

The X-ray source content of the XMM-Newton Galactic plane survey[★]

C. Motch^{1,★★}, R. Warwick², M. S. Cropper³, F. Carrera⁴, P. Guillout¹, F.-X. Pineau¹, M. W. Pakull¹, S. Rosen², A. Schwobe⁶, J. Tedds², N. Webb⁵, I. Negueruela⁷, and M. G. Watson²

¹ CNRS, Université de Strasbourg, Observatoire Astronomique, 11 rue de l'Université, 67000 Strasbourg, France
e-mail: christian.motch@astro.unistra.fr

² Department of Physics and Astronomy, University of Leicester, LE1 7RH, UK

³ Mullard Space Science Laboratory, University College London, Holmbury St. Mary, Dorking, RH5 6NT Surrey, UK

⁴ Instituto de Física de Cantabria (CSIC-UC), 39005 Santander, Spain

⁵ Centre d'Étude Spatiale des Rayonnements, 9 avenue du Colonel Roche, 31028 Toulouse Cedex 4, France

⁶ Astrophysikalisches Institut Potsdam, An der Sternwarte 16, 14482 Potsdam, Germany

⁷ Departamento de Física, Ingeniería de Sistemas y Teoría de la Señal, Universidad de Alicante, Apdo. 99, 03080 Alicante, Spain

Received 29 October 2009 / Accepted 2 July 2010

ABSTRACT

We report the results of an optical campaign carried out by the XMM-Newton Survey Science Centre with the specific goal of identifying the brightest X-ray sources in the XMM-Newton Galactic plane survey. In addition to photometric and spectroscopic observations obtained at the ESO-VLT and ESO-3.6 m, we used cross-correlations with the 2XMMi, USNO-B1.0, 2MASS, and GLIMPSE catalogues to advance the identification process. Active coronae account for 16 of the 30 positively or tentatively identified X-ray sources and exhibit the softest X-ray spectra. Many of the identified hard X-ray sources are associated with massive stars, possible members of binary systems and emitting at intermediate X-ray luminosities of 10^{32-34} erg s⁻¹. Among these are (i) a very absorbed, likely hyper-luminous star with X-ray/optical spectra and luminosities comparable to those of η Carina; (ii) a new X-ray-selected WN8 Wolf-Rayet star in which most of the X-ray emission probably arises from wind collision in a binary; (iii) a new Be/X-ray star belonging to the growing class of γ -Cas analogues; and (iv) a possible supergiant X-ray binary of the kind discovered recently by INTEGRAL. One of the sources, XGPS-25, has a counterpart of moderate optical luminosity that exhibits HeII λ 4686 and Bowen CIII-NIII emission lines, suggesting that this may be a quiescent or X-ray shielded low mass X-ray binary, although its X-ray properties might also be consistent with a rare kind of cataclysmic variable (CV). We also report the discovery of three new CVs, one of which is a likely magnetic system displaying strong X-ray variability. The soft (0.4–2.0 keV) band $\log N(>S)$ – $\log S$ curve is completely dominated by active stars in the flux range of 1×10^{-13} to 1×10^{-14} erg cm⁻² s⁻¹. Several active coronae are also detected above 2 keV suggesting that the population of RS CVn binaries contributes significantly to the hard X-ray source population. In total, we are able to identify a large fraction of the hard (2–10 keV) X-ray sources in the flux range of 1×10^{-12} to 1×10^{-13} erg cm⁻² s⁻¹ with Galactic objects at a rate consistent with what is expected for the Galactic contribution alone.

Key words. X-rays: binaries – X-rays: stars – surveys – binaries: close

1. Introduction

The brightest X-ray sources discovered by the early collimator-based experiments in operation in the 1970s were very luminous ($\sim 10^{38}$ erg s⁻¹), accretion-powered X-ray binaries located in our Galaxy (see e.g. the fourth Uhuru catalogue of X-ray sources; Forman et al. 1978). The dramatic improvement in sensitivity and spatial resolution afforded by the next generation of instruments exploiting X-ray imaging revealed a Galactic landscape with many more lower luminosity systems powered by a wide range of physical processes. For example, observations first with Einstein and later with ROSAT showed that low Galactic latitude regions are crowded with a large number of low-luminosity sources in the X-ray bands explored by these two missions (0.5–4.5 keV and 0.2–2.4 keV for Einstein and ROSAT respectively). These soft sources are predominantly identified with active

stellar coronae (e.g. Hertz & Grindlay 1984; Motch et al. 1997). The first imaging hard (2–10 keV) X-ray survey of the Galactic plane was performed a few years later with ASCA (Sugizaki et al. 2001). ASCA revealed the presence of a genuinely Galactic population of low-luminosity noncoronal X-ray sources that emit hard X-rays and are therefore detectable through large columns of interstellar absorption. However, the still relatively large positional errors affecting ASCA sources combined with the effects of the strong interstellar extinction in the Galactic plane prevented their optical identification in most cases.

The prospects for building a detailed census of the low to intermediate X-ray luminosity sources has now greatly improved with the launch of the Chandra and XMM-Newton observatories. Thanks to their unprecedented sensitivity and spatial resolution, these observatories are able to study the properties of the faint X-ray source populations throughout the Galaxy, most notably those present in large numbers in the central parts (Wang et al. 2002; Munro et al. 2003). The fields-of-view of the Chandra and XMM-Newton X-ray cameras are such that many serendipitous sources are seen in low-latitude fields in addition to the

* Tables 9–11 and Figs. 32, 33 are only available in electronic form at <http://www.aanda.org>

** Based on optical observations obtained at ESO under programmes 69.D-0143, 70.D-0227 and 71.D-0552.

primary targets, and the preliminary results of such surveys have already emerged in the context of the Champlane and XMM-Newton SSC surveys (Motch et al. 2003; Zhao et al. 2003; Hands et al. 2004; Grindlay et al. 2005; Motch 2006). Several dedicated Galactic surveys involving either single deep observations or a mosaic of shallower exposures have also been carried out or are in progress, (e.g. the Galactic centre region, Munro et al. 2003; Wijnands et al. 2006; Koenig et al. 2008; Munro et al. 2009; Revnivtsev et al. 2009).

The nature of the intermediate- to low-luminosity Galactic hard X-ray sources discovered in the Galactic plane surveys quoted above is only partially known. Cataclysmic variables (CVs) and quiescent X-ray binaries (both low- and high-mass types) account for a significant fraction, however, the exact nature of the majority of the sources detected in the central regions of the Galaxy remains doubtful in the absence of optical or infrared identifications, which in most cases are hindered by the large interstellar absorption.

The observation of intermediate- to low-luminosity Galactic X-ray sources can address many issues related to binary-star evolution and to accretion physics at low rates. In addition surveys which extend the search boundaries have the potential to improve our knowledge of source population statistics and to unveil rare types of compact X-ray-emitting systems which have a low space density in the local Galactic neighbourhood. For instance, the determination of the space density and scale height of CVs is relevant to estimates of the Galactic novae rate and connects to the origin of low-mass X-ray binaries and type Ia supernovae. Low X-ray luminosity but long lived evolutionary stages of classical low and high mass X-ray binaries could also be found in relatively large numbers if the predictions of some evolutionary scenarios are correct (see e.g. Pfahl et al. 2002; Willems & Kolb 2003). Massive X-ray binaries are good proxies of relatively recent star-bursts and if detected in sufficient numbers might give insight into the recent star-formation history of specific regions of our Galaxy.

Moreover, no X-ray telescope planned in the foreseeable future will have the necessary spatial resolution and sensitivity to study in detail the distribution of these low- and intermediate-luminosity sources in external galaxies. Consequently, X-ray surveys of our own Galaxy and its Magellanic satellites will remain for a long time the only means to study how the various X-ray emitting populations relate to the main Galactic structures such as the thin disc, the thick disc and the bulge.

However, such studies presuppose the knowledge of the nature of the bulk of the X-ray sources surveyed, a prerequisite which can only be fulfilled through multi-wavelength spectroscopic identifications. Nevertheless, the statistically controlled cross-correlation with large catalogues such as the 2MASS catalogue and/or with the recently made available source lists from the GLIMPSE surveys, provide useful information on the intensity and shape of the part of the spectral energy distribution in the observing windows least affected by line-of-sight absorption in the interstellar medium.

The work presented here was carried out in the framework of a Galactic plane survey programme instigated by the XMM-Newton Survey Science Centre (SSC). The long term objective of this project is to gather a representative sample of identified low-latitude X-ray sources, which eventually could be used as a template for identifying and classifying in a statistical manner the entire catalogue of serendipitous XMM-Newton sources detected in the Milky Way region. Companion programs are being carried out at high Galactic latitudes using three separate samples of sources selected at faint (Furusawa et al. 2008),

medium (Barcons et al. 2002) and bright (Della Ceca et al. 2004) fluxes.

In the first part of this paper, we recall the main properties of the XMM-Newton Galactic plane survey (XGPS) of Hands et al. (2004) and describe the way a sub-sample of X-ray sources were selected for optical follow-up at the telescope. The following section explains the method applied to cross-correlate the XGPS source list with the USNO-B1.0 and 2MASS catalogues and how identification probabilities were assigned to each optical or near infrared candidate. After a description of the observing procedures, the next section presents in detail the results of our optical spectroscopic identification campaign. The last sections discuss the $\log N(>S) - \log S$ curves and the statistics of the various kinds of X-ray emitters identified in the soft and hard bands as well as their contributions to the genuine Galactic population of low to medium X-ray luminosity sources¹.

2. The XGPS source sample

The XGPS was the first survey of an extended segment of the Galactic plane carried out by XMM-Newton (Hands et al. 2004). It covers a narrow strip of 1.2° in Galactic latitude, extending between 19° and 22° in Galactic longitude, centred on the Galactic plane and covering about 3 deg^2 . With an exposure time ranging between 6.6 and 13.7 ksec for the MOS cameras (but typically ~ 2 ksec less for the pn camera due to its longer set-up time), the limiting sensitivity is of the order of $4 \times 10^{-15} \text{ erg cm}^{-2} \text{ s}^{-1}$ in the 0.4–2 keV band and about $2 \times 10^{-14} \text{ erg cm}^{-2} \text{ s}^{-1}$ in the 2–10 keV band. The soft band sensitivity is about a factor 30 deeper than that of the ROSAT all-sky survey at low Galactic latitudes (e.g. Motch et al. 1997). In hard X-rays, the XGPS reaches limiting fluxes a factor 10 or more fainter than the ASCA Galactic plane survey (Sugizaki et al. 2001). Chandra is in principle able to reach significantly fainter flux limits. For instance, the deep observation at $l = 28.5^\circ$, $b = 0^\circ$ by Ebisawa et al. (2005) detects sources down to $\sim 3 \times 10^{-15} \text{ erg cm}^{-2} \text{ s}^{-1}$ in the hard band and $\sim 2 \times 10^{-16} \text{ erg cm}^{-2} \text{ s}^{-1}$ in the soft band. The Champlane project (Grindlay et al. 2005) based on archive observations with a broad spread of exposure times spans a range of sensitivity extending down to this deep survey limit. In summary, the XGPS can be described as a medium sensitivity survey offering unique coverage of several square degrees of the Galactic plane around $l = 20^\circ$. This is a direction in which the line-of-sight column density, N_{H} , integrated through the Galaxy, ranges from $\log(N_{\text{H}}) = 22.5$ to 23.5. It is also a region unhindered by the presence of one or more very bright Galactic sources (see Hands et al. 2004, for more details).

The catalogue of X-ray sources derived from the XGPS survey by Hands et al. (2004) was based on a customised background-fitting and source-detection software package, that pre-dated the full development of the XMM-Newton Science Analysis Software (SAS). The very robust XMM-Newton X-ray source catalogues that are now available (e.g. the 2XMM and 2XMMi catalogues, Watson et al. 2009), which utilise the latest software and calibration information, provide an opportunity for consistency checking of the original XGPS data. In this context we have cross-correlated the original XGPS list of sources with the 2XMMi catalogue in order to retrieve fully up-to-date X-ray source statistics and parameters. Among a total of 424 original XGPS sources, 269 have a match within $20''$ with a 2XMM/2XMMi entry. This rather large search radius

¹ All observational material including fits files is available at <http://xcatdb.u-strasbg.fr/xidresult>.

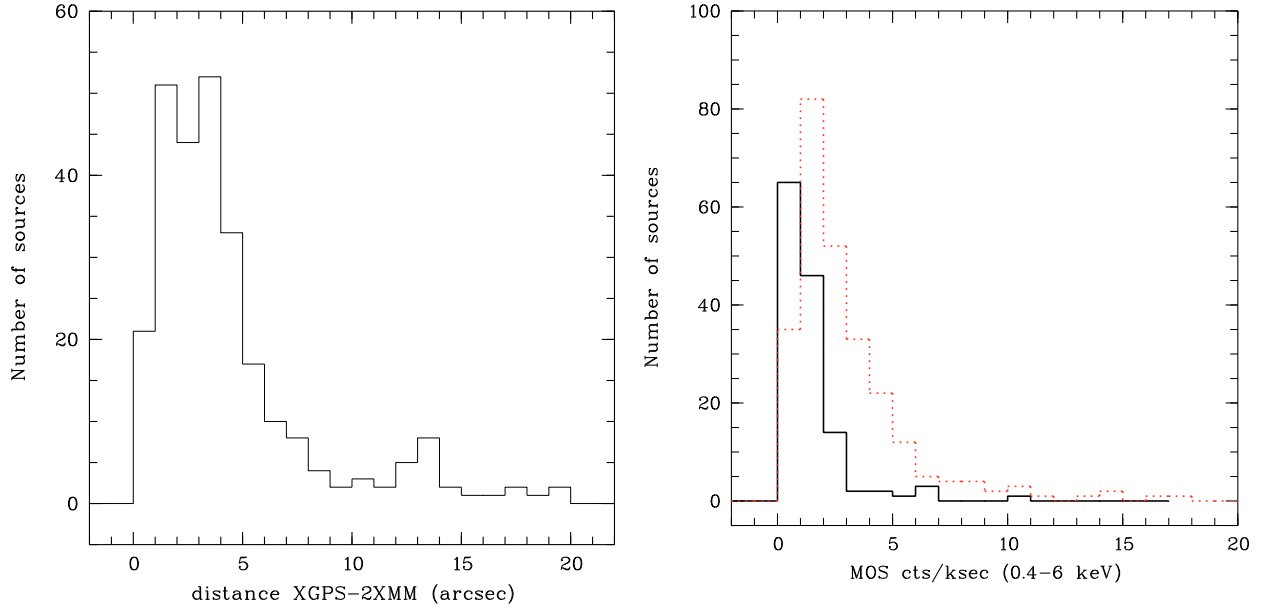


Fig. 1. *Left:* Histogram of distances between original XGPS positions and 2XMM positions. *Right:* Histogram of the XGPS MOS count rates for XGPS sources with a matching 2XMM entry (dashed red line) and without (plain black). The XGPS-2 field which is not part of the 2XMM catalogue has been excluded from the sample.

was chosen so as to cope with possibly large positional errors affecting some of the original XGPS source positions. Enlarging the search radius beyond $20''$ only brings a few extra matches. None of the new fields entered in the incremental version of the 2XMM catalogue (2XMMi) overlaps with the XGPS area and therefore, all matching sources also belong to the original 2XMM catalogue². Among the 155 XGPS sources not present in 2XMM, 21 are located in the XGPS-2 field (Obsid 0051940201) which due to an ODF format problem could not be processed by the 2XMMi production pipeline. The distribution of the positional offsets between XGPS and 2XMM sources plotted in the left panel of Fig. 1 shows that most matches occur at a distance less than $5''$ but that a small group of XGPS sources tend to be systematically offset by 12 to 14 arcsec. The positions of only 22 of the 269 2XMM sources could be corrected for residual attitude errors by *eposcorr*. This SAS task cross-correlates the observation source list with the USNO-B1.0 catalogue and searches for systematic offsets and rotation of the EPIC field with respect to the optical astrometric references. Typically, raw positions have 90% confidence error radii of the order of $4-5''$ while attitude corrected positions have 90% confidence error radii of the order of $3''$ (Watson et al. 2009). The relatively low EPIC exposure times and consequently few sources per observation combined with a high density of field stars at these low Galactic latitudes probably explain the failure of *eposcorr* to find significant correction patterns in most cases. This also implies that the XGPS-2XMM offsets are not due to the application/non-application of *eposcorr*, since no *eposcorr*-like task was used to correct the original XGPS-I coordinates, but rather result from the different algorithms used for source centering and attitude reconstruction. XGPS sources without corresponding 2XMM entries tend to be significantly fainter than those having a 2XMM match as shown in the right panel of Fig. 1. It seems a reasonable conjecture that the 134 XGPS sources not recovered in 2XMM

have, in effect, a lower maximum likelihood than the threshold applied in 2XMM ($ML = 6$). As a consequence the fraction of spurious sources in this fainter sample may well be considerably higher than is the case for the confirmed XGPS/2XMM matches.

As a second cross-check, in March 2008, we searched for Chandra observations covering the field of view of the XMM-Newton pointings involved in the XGPS. Unfortunately, the overlap is not large, with only 4 of the 22 XMM-Newton fields coincident with Chandra observations (obsids 5563, 6675 and 7479). We extracted from the Chandra X-ray Center archive the source lists produced by the standard data processing and created by *celldetect* version DS7.6 for the total energy range. The merged ACIS source lists were then cross-correlated with the XGPS catalogue using a search radius of $20''$. The process resulted in only 16 source matches. We list in Table 1 the distance to the matching Chandra source of the XGPS source, of its corresponding 2XMM entry and of the 2MASS entry matching the 2XMM source when available (see below Sect. 3.1). The quoted errors on the offsets between the 2XMM and Chandra source positions were derived by adding the individual positional errors in quadrature. Chandra positions have a typical one σ error in the range of $0.1''$ to $0.6''$. The 2XMM entries are in most cases closer to the Chandra position than the original XGPS positions, reflecting the improved precision of 2XMM positions compared to those of the XGPS. Moreover, the 2XMM coordinates are in all cases but one consistent at the 90% confidence with the Chandra values. The group of XGPS sources located far (10 to $17''$) from their 2XMM counterparts have Chandra positions consistent with those of the 2XMM source, clearly indicating that the large offset is not due to an attitude error in the 2XMM catalogue. Interestingly, the vast majority of the 2MASS candidate counterparts are located less than $1''$ from the Chandra position, the two discrepant cases being those for which the probability of identification, computed by the likelihood ratio algorithm, was less than 14% (see Sect. 3.1).

In planning the optical follow-up observations (which were carried out in 2002 and 2003, see Sect. 4) it was necessary, of course, to make use of the X-ray source flux and position

² The processing used to generate the incremental 2XMMi catalogue is the same as used for 2XMM. The 2XMMi catalogue has 626 more observations and about 17% more detections than the 2XMM catalogue.

Table 1. XGPS sources with matches in archival Chandra catalogues.

XGPS ID (1)	2XMM Name (2)	2MASS Name (3)	Ident Prob (4)	d XGPS (5)	d 2XMM (6)	error (7)	d 2MASS (8)	Chandra RA Dec (9) (10)	
12	2XMM J182830.8-114514	18283106-1145159	0.44	3.8	4.0	2.4	0.2	18 28 31.05	-11 45 15.7
23	2XMM J183017.0-095326	18301701-0953272	0.96	2.5	1.0	2.6	1.2	18 30 16.96	-09 53 26.8
29	2XMM J182740.3-113953	18274040-1139532	0.94	2.3	0.4	1.7	0.6	18 27 40.44	-11 39 53.1
73	2XMM J182732.2-113357	18273223-1133571	0.98	3.0	0.6	1.9	0.7	18 27 32.27	-11 33 57.4
74	2XMM J182750.5-113549	–	–	4.8	1.0	2.2	–	18 27 50.66	-11 35 48.6
110	2XMM J182728.5-113741	18272856-1137400	0.92	3.2	1.7	2.3	0.7	18 27 28.61	-11 37 40.1
124	2XMM J182811.1-114933	18281123-1149341	0.60	11.3	1.8	3.8	0.6	18 28 11.27	-11 49 34.3
142	2XMM J182744.6-113957	18274465-1139576	0.98	3.1	0.2	3.0	0.2	18 27 44.66	-11 39 57.7
161	2XMM J182812.3-114144	18281235-1141399	0.10	17.3	3.8	4.2	6.3	18 28 12.55	-11 41 45.5
168	2XMM J182749.5-113725	18274944-1137264	0.80	2.5	1.4	2.7	0.2	18 27 49.44	-11 37 26.2
190	2XMM J182821.1-114750	18282106-1147472	0.74	8.4	3.9	4.2	0.2	18 28 21.06	-11 47 47.0
208	2XMM J182831.5-115145	18283165-1151464	0.80	14.6	2.2	3.5	0.5	18 28 31.68	-11 51 46.3
237	2XMM J182804.6-113832	18280497-1138320	0.14	10.1	0.9	4.0	5.4	18 28 04.61	-11 38 33.1
263	2XMM J182824.2-114153	–	–	14.3	2.3	3.7	–	18 28 24.39	-11 41 55.0
287	2XMM J182806.1-113734	18280597-1137354	0.82	0.6	2.5	4.9	0.3	18 28 05.97	-11 37 35.7

Notes. The columns give the following information: (1) – XGPS identifier. (2) – Name of the corresponding 2XMM source. (3) – 2MASS entry correlating with the 2XMM source. (4) – Probability of identification of the 2XMM source with the 2MASS entry. (5) – d XGPS–Chandra. (6) – d 2XMM–Chandra. (7) – 90% confidence error on d 2XMM–Chandra. (8) d 2MASS–Chandra. (9) and (10) Chandra position. All position offsets are quoted in arcsec.

information available at the time. In effect this was a combination of preliminary XGPS catalogue data and information derived from early versions of SAS-pipeline processing. The error circles available at the time of the optical observations were systematically larger than those provided by the 2XMM catalogue. This mainly results from the improved astrometric accuracy provided by the latest SAS versions illustrated by the fact that the systematic positional error went down from 1.5'' to 1.0'' in the absence of *eposcorr* correction. In addition, the 2XMM catalogue now merges detections from distinct exposures to derive improved positions. Consequently, we observed on occasions optical candidates that were found out later to be well outside the revised error circle. However, in describing the multiwaveband follow-up we use in the main, when available, source parameters derived from the most recent 2XMM catalogues (Watson et al. 2009), including most importantly the positional information (e.g. see Sect. 3). That said, the X-ray bright, sub-sample of XGPS sources studied spectroscopically was selected on the basis of the original count-rate information from Hands et al. (2004) consisting of MOS camera count rates in a soft (0.4–2 keV), hard (2–6 keV) and broad (0.4–6 keV) band. More specifically the full preliminary XGPS catalogue was sorted into a list ordered on the basis of a decreasing MOS count rate in the broad band (0.4–6 keV). Objects were subsequently studied at the telescope in effect by working down this list. Fortunately, the post facto rationalisation in terms of a XGPS/2XMM selection does not have a high impact on this bright source sub-sample. In the event a total of 43 X-ray sources down to a MOS broadband count rate of 4.2 counts/ks were investigated in detail (see Sect. 5 for further details).

The XGPS id number used throughout this paper refers to the rank of the source in the preliminary XGPS catalogue used at the time of the optical observations and sorted by decreasing MOS countrates in the broad band. This list differs from that published in Hands et al. (2004) in the sense that it misses a few sources which were later appended to the final catalogue (see Sect. 5.5.8) and also contains a few duplicated or spurious entries. As a consequence, the id number does not exactly follow the true broad band flux order of the final XGPS catalogue. Note that the

naming of the XGPS XMM-Newton fields in Hands et al. (2004) is distinct from the source numbering system used in this paper.

All error circles plotted on finding charts correspond to a 90% combined X-ray/optical confidence circle. For several interesting sources we retrieved X-ray data from the XMM-Newton archive at ESAC and processed them with the latest version of the SAS package (version 8) and calibration files. Spectral analysis was performed using *XSPEC* version 12.1 and above. Unless specified otherwise, all fit parameters are given at the 90% confidence level for one parameter of interest. Fit results are summarized in Table 10.

3. Cross-correlation of the XGPS/2XMM list with optical/IR catalogues

Optical crowding makes the identification of XMM-Newton sources in the Galactic plane rather difficult. Originally (circa 2002) the SAS task *eposcorr* corrected EPIC source positions for residual attitude errors by matching the X-ray source positions with the USNO-A2.0. However in the 2XMM pipeline, the cross-matches are done with the deeper USNO-B1.0 catalogue. When applicable, i.e., if the field stellar density is not too high to confuse the statistical cross-identification process, *eposcorr* can significantly reduce the 90% confidence error circle by decreasing systematic errors and thus easing optical identification. However, as noted above, the positions of most of the XGPS/2XMM sources could not be refined by *eposcorr*. Even with this improvement, XMM-Newton error circles are sufficiently large that for Galactic studies it is often the case that several optical candidates have positions consistent with the X-ray source, with none of these candidates standing out as the main contender. In this respect, the excellent positions provided by Chandra with a sky uncertainty area an order of magnitude smaller than that of XMM-Newton constitute a major advantage for Galactic plane studies.

Nevertheless, it is possible to find probable counterparts to at least a fraction of the XMM-Newton sources found in low-latitude fields by cross-correlation with major optical and infrared catalogues. Thus for all the XGPS/2XMM sources we

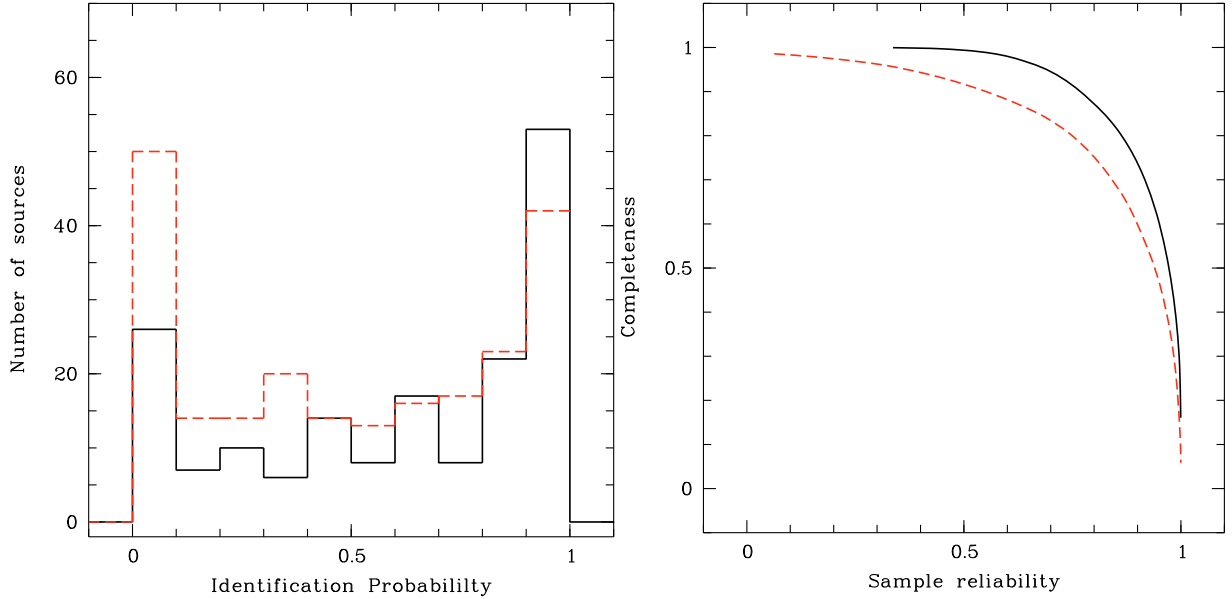


Fig. 2. *Left:* Histogram of the USNO-B1.0 (plain black) and 2MASS (dashed red) probabilities of identification in the XGPS region. *Right:* relation between the integrated sample reliability versus completeness for USNO-B1.0 (plain black) and 2MASS (dashed red).

looked for possible identifications in archival catalogues using the XCat-DB³ developed in Strasbourg (Motch et al. 2007b).

3.1. Cross-correlation with USNO-B1.0 and 2MASS

In a sizable number of cases, the XMM-Newton error circle contains a relatively bright optical object. This is consistent with the fact known from previous ROSAT surveys, namely that the majority of soft Galactic X-ray sources are active stars (e.g. Motch et al. 1997) which, apart from the faintest K and M types, appear as relatively bright optical objects even at the flux sensitivity of XMM-Newton. There is obviously a limiting magnitude at which the appearance of a relatively bright optical object in the EPIC error circle has a high probability of being a chance coincidence due to the increasing density of field objects with magnitude. In order to properly estimate the probability of identification of the X-ray source with a USNO-B1.0 (Monet et al. 2003) or 2MASS (Cutri et al. 2003) entry, we used the likelihood ratio scheme especially developed by Pineau et al. (2008, 2010) in the framework of the XMM-Newton SSC for the cross-identification of the 2XMMi sources with several large astronomical catalogues. In a few words, the process considers the widely used ratio between the likelihood that the optical and X-ray sources are associated and thus have the same position, to the likelihood to find by chance an optical object as bright as the candidate at that angular distance from the X-ray source. This likelihood ratio, however, does not provide a direct measure of the value of the association since it formally depends on the probability that a given X-ray source has to have a counterpart in the archival catalogue considered. Eventually, this probability depends on the properties and relative fractions of the various populations of X-ray sources entering the overall sample. Most authors build a histogram of the associations likelihood ratios (LR) and estimate the contributions of spurious matches to this histogram by randomising the X-ray positions. This Monte Carlo process might be time consuming when applied to very large samples and the scheme used in Pineau et al. (2008, 2010) uses

a geometrical approach instead. For a given bin of likelihood ratio the probability of identification is then derived from the ratio of total observed (true + spurious) to estimated spurious associations. In practice, it is necessary to merge the LR histograms of several XMM-Newton observations at similar Galactic latitudes to obtain enough statistics and fit in a reliable manner the relation between spurious match rate and likelihood ratio. The probabilities of identifications with 2MASS and USNO-B1.0 entries were retrieved from the XCat-DB for each XGPS source having a corresponding entry in the 2XMM catalogue.

The cross-correlation process searches for possible candidate counterparts within a radius corresponding to 3.44 times the combined 1σ positional error (obtained by adding the X-ray and catalogue 1σ errors in quadrature). This corresponds to the area in which 99.7% of the true matches (3 Gaussian σ) should be found. For the 2XMM catalogue, we use the combined intrinsic plus systematic⁴ positional error as listed in the column labelled *poserr* which has a mean value of $1.8''$ (1σ) for the sample of 269 2XMM/XGPS sources. Typical positional errors on USNO-B1.0 and 2MASS entries are much lower, of the order of a few tenth of an arcsecond (Monet et al. 2003; Cutri et al. 2003). Over the whole XGPS area, a total of 171 and 223 2XMM X-ray sources have a match with a USNO-B1.0 and 2MASS entry respectively. Although the number of matches appears significantly higher in the near infrared than at optical wavelengths, the relatively high density of 2MASS entries in the Galactic plane decreases the reliability of these cross-identifications. The left panel of Fig. 2 shows that the number of high probability (>90%) USNO-B1.0 identifications is 53 while only 42 2MASS entries have as high probabilities of identification. We define the sample reliability as the expected fraction of correct identifications among matches with an individual identification probability above a given threshold. Completeness is then the fraction of true identifications recovered above that threshold divided by the total number of true identifications expected in the given survey. Computed over the entire XGPS area, the completeness versus reliability curve shown in the right panel of Fig. 2 reveals

³ <http://xcatdb.u-strasbg.fr/>

⁴ $0.35''$ or $1.0''$ depending on the outcome of *eposcorr* task (Watson et al. 2009).

Table 2. Fraction of spurious identifications and completeness for the 2XMM/USNO-B1.0 and 2XMM/2MASS cross-correlation in the XGPS area as a function of the individual probability threshold.

	2MASS ident. prob.				
	50%	60%	70%	80%	90%
Spurious Fr.	21.4	13.6	08.8	04.3	01.3
Completeness	76.7	66.6	57.2	44.1	27.4
	USNO-B1.0 ident. prob.				
	50%	60%	70%	80%	90%
Spurious Fr.	18.9	12.8	08.8	04.3	01.2
Completeness	86.2	79.1	71.1	57.5	39.4

Notes. The spurious fraction and completeness values are given as a percentage.

that the USNO-B1.0 catalogue provides more reliable and more complete identifications than the 2MASS catalogue. On average, matches with identification probabilities of less than 10% are with USNO-B1.0 and 2MASS objects only one or two magnitudes brighter than the limiting magnitudes (~ 20 in R and ~ 12.5 in K). In contrast, candidate counterparts with identification probability $\geq 90\%$ are typically either USNO-B1.0 entries brighter than $R \sim 15$ or 2MASS entries with K ranging from 12 to 8 with a mean value of ~ 10 .

Therefore, thanks to a careful statistical handling of the cross-correlation process, we are able, in many cases, to recover with high efficiency the actual counterpart of the X-ray source and quite significantly extend the identification rate. This can be achieved in spite of the poorer XMM-Newton positional accuracy as compared to that of Chandra for X-ray sources having bright enough optical counterparts.

We list in Table 2 values of the fraction of spurious identifications and completeness as function of the threshold set on the individual source identification probability. At the 90% threshold generally used in this work, the number of wrong identifications should be of the order of 1%, and only 30% to 40% of the true matches are identified.

3.2. Cross-correlation with Spitzer source lists

We also explored the content of the recently released Spitzer source catalogue from the Galactic Legacy Infrared Mid-Plane Survey Extraordinaire (GLIMPSE) project (Benjamin et al. 2003). The survey provides images and source lists with magnitudes and fluxes in the four bands of the IRAC instrument, centred at approximately 3.6, 4.5, 5.8 and 8.0μ . GLIMPSE I covers the Galactic longitudes from 10° to 65° with a width of $\pm 1^\circ$ in latitude and thus perfectly overlaps with the area covered by the XGPS survey. We extracted the individual source lists from the GLIMPSE I archive⁵ merging the catalogues covering the range of Galactic longitude $l = 19.0^\circ$ to 22.15° . We did not compute the probabilities of identifications of EPIC sources with GLIMPSE entries using the LR based method described above but instead simply considered all GLIMPSE candidate counterparts in a radius of $7''$ (≥ 3 average σ) around the 2XMM X-ray position. GLIMPSE positions are only subject to small errors since 95% of the Spitzer sources are within $0.2''$ from their 2MASS counterparts⁶. The Spitzer IRAC flux measurements

⁵ http://data.spitzer.caltech.edu/popular/glimpse/20070416_enhanced_v2/source_lists/north/

⁶ GLIMPSE Quality Assurance v1.0.

were used to constrain the spectral energy distributions of some of the candidate counterparts and provide additional identification diagnostics. However, the GLIMPSE source lists provide 2MASS identifications which can be used as proxies to compute likelihoods of associations using the 2XMM/2MASS cross-correlation. We list in Table 3 the 55 XGPS/2XMM sources having an identification probability above 80% with a 2MASS + GLIMPSE entry, together with their identification class (see Sect. 5). We checked that beyond a radius of $7''$, no more 2MASS + GLIMPSE identifications of 2XMM sources are found with probabilities larger than 80%.

4. Optical observations

The optical observations presented here were obtained in 2002 and 2003 with the ESO 3.6 m telescope and the ESO-VLT. At the ESO-3.6 m equipped with EFOSC2, observations took place from July 9 to 12 in 2002 and from February 28 till March 3 and from June 27 till July 2 in 2003. An additional run was performed in 2003 with the VLT-Yepun and FORS2 on July 1st and 2nd. Bright optical stars were observed with grism #14 on EFOSC2, while spectra of fainter candidates were obtained using grisms #6 and #1. At the VLT, we used grisms GRIS_1400V for the brightest objects and GRIS_300I or GRIS_300V for the faintest ones. Absolute flux calibration was derived from the observation of standard stars done every night. Weather conditions were photometric in most cases. Table 4 shows the details of the instrumental setups relevant to this work.

All CCD frames were corrected for bias and flat-fielded using standard MIDAS procedures. Arc-lamp exposures of various atomic species were used to derive a wavelength calibration generally accurate to better than 5% of the spectral resolution. One dimensional spectra were extracted with a procedure optimising the accumulation region in order to reach the best signal to noise ratio and using sky background cleaned from cosmic-ray impacts. The requirement to put two optical candidates in the slit, in order to minimise observing time, prevented it from being aligned along or close to the parallactic angle. Consequently, the accuracy of the flux calibration, whilst sufficient to derive relative fluxes, may still suffer from moderate spectral distortion in some instances.

Stellar spectral classification can be difficult when using only low to moderate spectral resolution, particularly in the case of faint stellar counterparts with spectra of commensurately low signal to noise ratio. In order to perform a classification with a minimum of bias, we designed a MIDAS procedure in which flux calibrated reference spectra degraded to the spectral resolution of the observations are fitted to the observed spectrum by adjusting the mean flux and interstellar absorption. We used standard spectra from various references depending on the resolution and wavelength range of the observation. The most useful atlases were those of Jacoby et al. (1984), Pickles (1998), STELIB (Le Borgne et al. 2003) and a collection of spectra extracted from the NASA/JPL NStars project⁷. The spectral fitting process was visually controlled and checked by monitoring the behaviour of several important diagnostic lines (Turnshek 1985; Jaschek & Jaschek 1987). We estimate that our spectral classification is on average accurate to one subclass.

In addition, we obtained photometrically uncalibrated broad band imaging at the ESO 3.6 m and ESO-VLT telescopes in the B , R and I filters for XGPS positions lacking relatively bright optical candidates. Standard MIDAS procedures allowed us to

⁷ <http://stellar.phys.appstate.edu/>

Table 3. XGPS/2XMM - 2MASS - GLIMPSE I cross correlation.

XGPS id	Class	2MASS name	2MASS Prob id	<i>J</i>	<i>err</i>	<i>H</i>	<i>err</i>	<i>K</i>	<i>err</i>	3.6 μ	<i>err</i>	4.5 μ	<i>err</i>	5.8 μ	<i>err</i>	8.0 μ	<i>err</i>
2	AC	18284546-1117112	0.97	9.80	0.02	9.14	0.02	8.96	0.02	8.91	0.04	8.92	0.05	8.74	0.04	8.77	0.03
6	AC	18284771-1013354	0.98	7.48	0.02	7.22	0.05	7.13	0.03	7.23	0.03	7.25	0.05	7.18	0.04	7.14	0.02
11	AC	18250691-1204304	0.89	10.39	0.02	9.38	0.02	9.03	0.02	8.80	0.05	8.80	0.05	8.68	0.04	8.64	0.04
14	WR	18311653-1009250	0.98	9.09	0.03	8.29	0.04	7.63	0.02	7.17	0.04	6.83	0.06	6.66	0.03	6.32	0.03
16	AC	18303575-1021039	0.96	11.06	0.06	10.32	0.07	10.04	0.05	9.77	0.05	9.75	0.07	9.55	0.05	9.49	0.07
20	AC	18263956-1142150	0.88	11.36	0.02	10.81	0.04	10.57	0.03	10.31	0.11	10.43	0.10	10.31	0.11	10.19	0.07
21	AC	18310376-0958153	0.86	12.39	0.03	11.73	0.05	11.38	0.05	11.08	0.07	11.07	0.09	10.97	0.10	10.81	0.13
23	AC	18301701-0953272	0.96	11.40	0.03	10.60	0.03	10.32	0.02	10.09	0.04	10.09	0.06	9.94	0.05	9.94	0.04
30	AC	18274009-1028124	0.84	11.56	0.04	10.83	0.04	10.49	0.04	10.28	0.06	10.34	0.06	10.25	0.06	10.31	0.08
36	HMXB?	18301593-1045384	0.93	10.54	0.02	10.10	0.02	9.67	0.02	9.01	0.05	8.77	0.05	8.55	0.04	8.26	0.04
42	UNID	18283337-1026505	0.95	11.41	0.03	10.21	0.02	9.72	0.02	9.37	0.04	9.43	0.05	9.24	0.05	9.19	0.05
46	AC	18312487-1047478	0.98	8.32	0.03	8.19	0.05	8.11	0.03	8.02	0.06	8.02	0.04	8.06	0.03	8.05	0.04
51		18253369-1214505	0.95	11.27	0.02	10.76	0.02	10.59	0.02	10.47	0.07	10.42	0.06	10.40	0.09		
59		18281589-1154333	0.92	10.54	0.02	9.24	0.03	8.78	0.03	8.46	0.04	8.52	0.04	8.39	0.04	8.41	0.03
60	AC	18251158-1157257	0.96	10.58	0.02	10.24	0.03	10.15	0.03	9.98	0.06	10.00	0.05	9.94	0.05	10.03	0.05
61		18282189-1011279	0.98	8.98	0.02	8.63	0.03	8.51	0.03	8.45	0.06	8.42	0.06	8.47	0.04	8.43	0.03
66		18284762-1155529	0.91	11.92	0.03	10.90	0.03	10.51	0.02	10.39	0.06	10.28	0.11	10.13	0.06	10.15	0.06
71		18292438-1029568	0.92	12.19	0.02	11.37	0.02	11.15	0.02	10.99	0.05	10.95	0.07	11.02	0.09	11.14	0.10
72		18321298-1006343	0.94	11.81	0.02	11.14	0.03	10.89	0.03	10.72	0.04	10.59	0.06	10.60	0.06	10.70	0.08
73		18273223-1133571	0.98	12.03	0.03	10.50	0.03	9.88	0.03	9.49	0.05	9.47	0.05	9.27	0.05	9.22	0.04
75		18263832-1043417	0.90	11.40	0.02	10.90	0.03	10.76	0.02	10.43	0.04	10.50	0.06	10.52	0.07	10.42	0.05
82		18264265-1121246	0.98	6.11	0.05	5.81	0.04	5.65	0.03	5.48	0.05	6.05	0.12	5.39	0.03	5.31	0.03
95		18263599-1146469	0.97	10.32	0.02	9.56	0.03	9.27	0.02	9.06	0.04	9.17	0.05	9.06	0.04	9.01	0.04
110		18272856-1137400	0.92	11.86	0.03	11.23	0.04	11.02	0.05	10.99	0.06	10.94	0.09	10.88	0.09	11.27	0.11
112		18254529-1131541	0.95	10.57	0.02	10.23	0.04	10.00	0.03	9.95	0.05	9.94	0.06	9.94	0.06	9.89	0.05
113		18291343-0957303	0.95	10.82	0.02	10.27	0.03	10.08	0.03	9.98	0.04	10.04	0.07	9.81	0.06	9.85	0.04
117		18293962-1058346	0.89	11.80	0.02	11.14	0.02	10.86	0.02	10.49	0.05	10.49	0.13	10.29	0.07	10.35	0.08
119		18301584-1024593	0.88	12.33	0.04	11.40	0.05	11.11	0.04	10.82	0.05	10.84	0.08	10.72	0.06	10.65	0.06
122		18303260-0947301	0.89	11.20	0.03	10.60	0.04	10.37	0.03	10.25	0.04	10.15	0.04	10.11	0.06	10.10	0.04
125		18260807-1215145	0.97	11.39	0.02	10.68	0.02	10.54	0.02	10.40	0.03	10.53	0.06	10.38	0.06	10.60	0.16
130		18281914-1002074	0.98	7.12	0.02	5.97	0.03	5.49	0.03	5.31	0.07	6.03	0.11	5.27	0.03	5.23	0.03
132		18301787-1027277	0.92	10.39	0.03	10.01	0.03	9.88	0.02	9.90	0.07			9.89	0.10	10.52	0.22
135		18272674-1120398	0.93	12.34	0.03	11.73	0.05	11.52	0.05	11.35	0.07	11.28	0.08	11.37	0.12	11.33	0.12
142		18274465-1139576	0.98	9.59	0.02	8.95	0.03	8.78	0.02	8.67	0.05	8.70	0.05	8.70	0.04	8.67	0.03
156		18270828-1134567	0.90					9.19	0.03	8.51	0.03	8.63	0.05	8.26	0.03	8.37	0.03
174		18283639-1036553	0.85	12.18	0.02	11.12	0.02	10.70	0.02	10.40	0.04	10.51	0.06	10.35	0.08	10.39	0.06
182		18274957-1025358	0.92	10.32	0.03	9.89	0.03	9.58	0.03	9.57	0.21	9.23	0.13	9.40	0.05	9.25	0.04
203		18262946-1100587	0.95	10.60	0.02	9.70	0.03	9.43	0.03	9.20	0.04	9.23	0.05	9.16	0.05	9.08	0.03
208		18283165-1151464	0.80					11.11	0.03	10.78	0.07	10.86	0.06	10.83	0.10	11.06	0.10
214		18303226-1051502	0.98	6.89	0.02	6.68	0.03	6.57	0.02	6.81	0.04	6.57	0.05	6.60	0.04	6.58	0.02
224		18285835-1039133	0.86	10.01	0.02	8.44	0.06	7.73	0.03	7.34	0.03	7.54	0.05	7.28	0.04	7.18	0.03
249		18284536-1156528	0.86	11.59	0.02	11.24	0.02	11.10	0.02	11.08	0.05	10.98	0.06	10.91	0.07	11.07	0.09
254		18271801-1128218	0.82	12.95	0.05	12.07	0.07	11.62	0.03	11.05	0.10	11.02	0.10	10.97	0.09	10.78	0.09
276		18271464-1130273	0.96	12.08	0.03	11.21	0.04	10.84	0.03	10.49	0.07	10.41	0.09	10.45	0.09	10.40	0.07
283		18274118-1127156	0.94					11.54	0.05	11.26	0.06	11.27	0.10	11.18	0.07		
287		18280597-1137354	0.82	11.97	0.03	11.60	0.04	11.35	0.03	11.11	0.13	10.99	0.12	10.98	0.09		
305		18281180-1025424	0.98	8.36	0.03	6.93	0.04	5.63	0.03	4.50	0.09			3.54	0.06		
319		18294250-1100494	0.84	11.33	0.03	9.91	0.03	9.34	0.03	8.91	0.06	8.86	0.05	8.77	0.04	8.75	0.04
322		18291086-1042454	0.93	10.93	0.02	9.74	0.03	9.31	0.03	8.99	0.05	9.00	0.05	8.96	0.04	8.82	0.04
326		18273027-1135116	0.83	10.91	0.02	10.65	0.03	10.56	0.03	10.42	0.06	10.41	0.06	10.45	0.06	10.40	0.07
350		18260167-1220208	0.88	9.97	0.02	7.02	0.03	5.52	0.02	4.40	0.07			3.69	0.03	3.41	0.05
383		18302135-1050371	0.93	11.06	0.02	10.56	0.02	10.37	0.02	10.27	0.05	10.24	0.06	10.17	0.06	10.31	0.06
405		18244642-1204260	0.98	7.82	0.03	7.43	0.02	7.22	0.02	7.05	0.05	7.01	0.04	6.89	0.03	6.88	0.02

Notes. We only list here 2MASS sources with an individual probability of identification with the corresponding 2XMM source above 80% and identified with a GLIMPSE I source. The entries under the column labelled “Class” refer to the nature of the source as derived from our optical follow-up programme: AC (active corona); WR (Wolf-Rayet star); HMXB (high-mass x-ray binary); UNID (un-identified source). The measurements in the different wavebands are given in magnitudes.

correct these frames for bias and flat-field. These exposures were used to prioritise targets for subsequent spectroscopic observations. Some of the finding charts presented in this work are also based on these data. Short raw white light acquisition images are also used on occasion. Finally, many of the charts are based on MAMA scans of the *R* band plate SRC734S extracted from

the second epoch survey of the ESO/SERC Southern Sky Atlas. All images were astrometrically corrected using reference stars in the GSC 2.2 catalogue. We estimate that the resulting positions are good to $\sim 0.3''$. This error is quadratically added to XMM-Newton astrometric errors when plotting the 90% confidence error circle.

Table 4. Optical spectroscopic settings.

Telescope	Instrument	Spectral range (Å)	<i>FWHM</i> spectral resolution (Å)	Slit width (")	Grisms
ESO-3.6 m	EFOSC2	3185–10940	59	1.5	Grism #1
ESO 3.6 m	EFOSC2	3860–8070	17.3	1.5	Grism #6
ESO 3.6 m	EFOSC2	3095–5085	7.1	1.5	Grism #14
ESO-UT4	FORS2	3850–7500	12	1.0	GRIS_300V
ESO-UT4	FORS2	5900–10240	11	1.0	GRIS_300I
ESO-UT4	FORS2	4560–5860	2	1.0	GRIS_1400V

5. Optical identification of a bright source sub-sample

As mentioned earlier, the basic strategy of the optical spectroscopic campaign was to start with the brightest XGPS sources in the broad band and then to work down the XGPS list to fainter count rates. However, even at the low Galactic latitude ($b \sim 0^\circ$) covered by the XGPS, the integrated Galactic interstellar absorption along the line of sight is not large enough ($N_{\text{H}} \sim 10^{23} \text{ cm}^{-2}$) to efficiently screen hard X-rays above $\sim 2 \text{ keV}$. We thus expected that many of the XGPS sources might actually be background AGN.

In order not to waste valuable telescope time, we did not investigate the content of the error circles of sources void of optical candidates bright enough to obtain optical spectra in a reasonable amount of time and exhibiting a MOS hardness ratio⁸ consistent with that expected for an extragalactic source undergoing the total Galactic absorption in the source direction. The expected MOS hardness ratios of extragalactic sources were computed assuming a power-law spectrum of photon index equal to 1.7. As it was, we used the finding charts provided by the XMM-Newton pipeline⁹ which in the region of the Galactic plane covered by the XGPS are based on the same R band second epoch survey of the ESO/SERC Southern Sky Atlas as used for some of the finding charts shown in Fig. 33. We did not consider for optical follow-up X-ray sources having no detectable objects in their error circles implying a limiting magnitude of $R \sim 21.5$ ¹⁰. This corresponds to the faintest targets reachable with the instrument used at the 3.6 m telescope. Evidently, optically faint Galactic X-ray sources undergoing large foreground or internal absorption would also be discarded by this selection criterion.

We used the cross-correlations of EPIC source positions with over 170 astronomical catalogues available in the pipeline data produced by the Survey Science Centre to investigate the content of the EPIC error circles¹¹.

We have computed the expected total Galactic absorption in the direction of each XGPS source from the IR maps provided by COBE/DIRBE and IRAS/ISSA (Schlegel et al. 1998). We compared these values to those obtained by summing the HI (Dickey & Lockman 1990) and CO (Dame et al. 2001) column densities

⁸ $\text{HR} = (\text{H}-\text{S})/(\text{H}+\text{S})$ with H and S the count rates in the 2.0–6.0 keV and 0.4–2.0 keV bands respectively (Hands et al. 2004).

⁹ SSC provided finding charts are based on images extracted from the Aladin image server at CDS (Bonnarel et al. 2000).

¹⁰ <http://www.roe.ac.uk/ifa/wfau/ukstu/platelib.html>

¹¹ The SSC pipeline lists all archival catalogue entries with positions consistent within 3σ with the EPIC source. However, at this stage, no probability of identification is computed. These cross-correlations are available from the XCat-DB. See Watson et al. (2009) for a complete description.

in each direction. Values were interpolated over the 4 nearest pixels (of size $2'.37^2$) for the COBE/DIRBE maps, whereas the HI and CO maps were not interpolated and had pixel sizes of $0'.5^2$ and $0'.121^2$ respectively. We assumed $N_{\text{H}} = N_{\text{HI}} + 2 \times N_{\text{H}_2}$ with $N_{\text{H}_2} = 2.7 \cdot 10^{20} \times W_{\text{CO}}$ where W_{CO} is the intensity of the CO 1-0 rotational transition. The two determinations of the total column density agree well. However, the radio determined N_{H} value clearly saturates at $\text{Log}(N_{\text{H}}) \geq 23.1$. We thus retained the N_{H} values derived from the IR maps as providing a more realistic estimate of the total Galactic absorption.

In the event our programme of optical spectroscopic follow-up extended down to the 63rd source in the count-rate ordered preliminary XGPS list (XGPS-69) to a limiting MOS broadband count rate of 4.2 ct/ks. However, of these 63 sources, 12 were discarded due to the optical candidate/MOS hardness-ratio criterion outlined above and 8 due to lack of observing time at the ESO 3.6 m telescope or due to very offset XGPS positions.

This leaves us with a total of 43 XGPS sources which were investigated at the telescope. Of these, we failed to identify a likely counterpart in 13 cases due to the lack of spectral signatures of known classes of X-ray emitters in the observed candidates or because the optical candidates turned out to be too faint for the instrumental setting used at the given telescope. Further details of these 43 sources are given later – in Table 8. Possible identifications are discussed in Sects. 5.1 to 5.4, while some of the unidentified sources for which we have the most constraining information are presented in Sect. 5.5. Optical spectra for all identified sources are available as online material (Fig. 32). Finding charts for all of the 43 investigated sources are either shown in Sect. 5 or in the online material section (Fig. 33).

As a check for unforeseen biases we have investigated some of the characteristics of our “telescope” sample in relation to the whole XGPS catalogue. For example, Fig. 3 shows the histogram of the broad-band (0.4–6.0 keV) MOS count rate for sources scheduled for optical follow-up compared to that of the entire final XGPS sample of 424 sources. The difference between the two histograms is explained by the fact we ignored 20 sources. In addition, as mentioned in Sect. 2 (see also Sect. 5.5.8), the preliminary version of the XGPS catalogue used at the telescope was missing a few bright sources.

We plot in Fig. 4 the histogram of the integrated Galactic N_{H} for the entire XGPS set of 424 sources and for the sub-sample of 43 bright sources investigated optically. The distribution shows that the broad band bright sample of XGPS sources selected for optical follow-up does not exhibit any bias towards obscured or clear Galactic directions.

Table 5 provides a break-down by identification type for the 43 sources studied at the telescope. In practice, the faintest identified XGPS source is XGPS-65 with a broad band MOS count rate of 4.5 ct/ks.

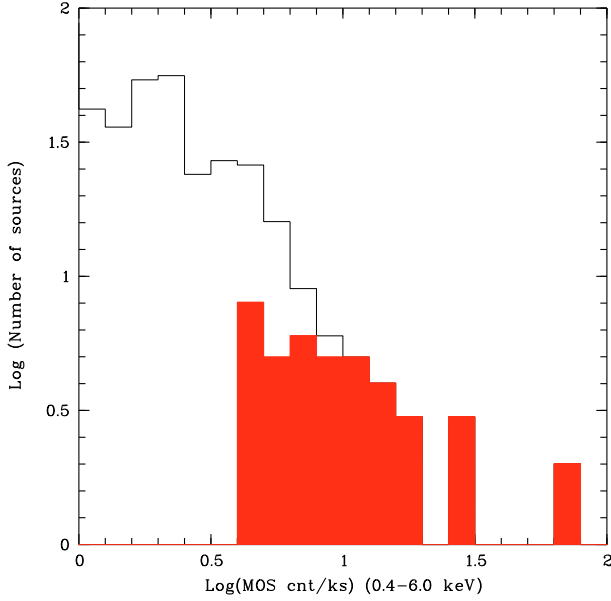


Fig. 3. Histogram of the MOS broad-band flux for the entire XGPS sample and for the sub-sample scheduled for identification at the telescope (red histogram).

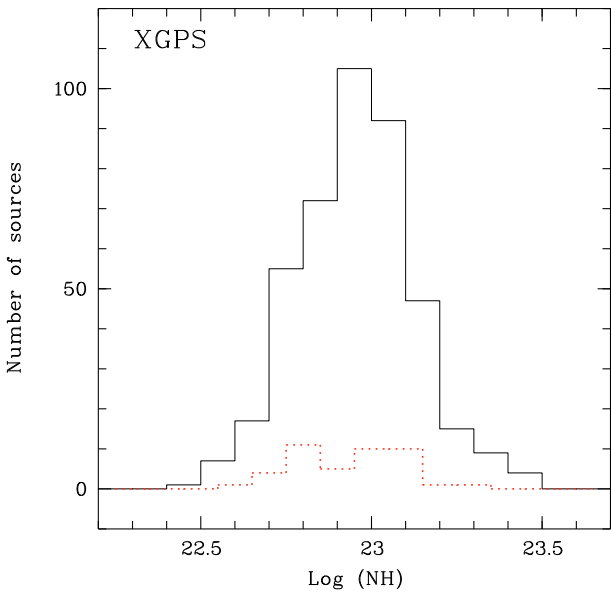


Fig. 4. Distribution of integrated N_H for the entire set of XGPS sources (black solid line) and for the sources investigated optically (red dashed line).

5.1. Stellar identifications

5.1.1. Normal stars

Our identification of an X-ray source with an active corona (AC), in the main, rests on the detection of spectroscopic evidence such as Balmer emission or Ca H&K re-emission. However, when the optical spectrum of the candidate star was lacking such features, the identification was then based on a probability of association with the USNO-B1.0 or 2MASS object above 90%. Note that in this statistical identification process, we did not apply any constraint on X-ray hardness ratio.

Most coordinates of active coronae are derived from their GSC2 entry and thus reflect their position near epoch 1988.

Table 5. Identification statistics for the sub-sample of XGPS sources selected for follow-up optical observations.

Class	Number
AC	16
Possible AC	2
B stars	2
WR	1
CV	3
LMXB candidates	2
HMXB candidates	4
Unidentified	13
Total	43

Notes. AC: Active Coronae, WR: Wolf-Rayet star.

However, whenever a TYCHO entry was available we used the TYCHO coordinates corrected for proper motion at epoch J2000, i.e. at a time very close to X-ray observations. A close inspection of finding charts in Fig. 33 reveals the relatively high proper motion of XGPS-6 whose 2001 X-ray position is overplotted on a plate acquired in 1982 and of that of the counterpart of XGPS-21 whose 2003 position is well inside the error circle.

A total of 16 (or 18 including the two dubious cases) of the 30 sources having a confirmed or a tentative identification fall into the AC category. Stars located across all regions of the HR diagram have been detected in X-rays (see e.g. Vaiana et al. 1981; Guillout et al. 1999) barring A-type stars and cool M-type giants (although even in these cases exceptions do exist).

For the hottest O, B stars, shocks forming in unstable winds heat the ambient plasma to million degree temperatures, while for late-type stars, X-ray emission results from magnetic activity in the outer stellar atmospheres due to an interplay between rotation and subsurface convection. In the latter case whether the coronae are energised by flares, waves or currents is still debated. If the counterpart is a late B-type or an A-type star then very often the X-ray emission is ascribed to an unresolved, active, binary companion (see for instance Neff & Simon 2008).

In our spectroscopically identified sample we find 2 K stars, 3 G stars and one late B and one late A star (in these two later cases, we assumed that X-ray emission arises from a late-type stellar companion). We also have 9 counterparts which are Me stars in the range of M1e to M6e. Source XGPS-16 is identified with a likely physical pair of a M4 and a M5 emission line stars, based on their comparable photometric distances. The X-ray brightest coronal source, XGPS-2, was also detected in the ASCA Galactic plane survey (AX J182846-1116, Sugizaki et al. 2001). We also identify two sources XGPS-19 and XGPS-56 with early B type stars.

Unfortunately, the absence of reliable optical spectrophotometric flux calibration resulting from the observing procedure prevents us from deriving accurate enough reddening corrected X-ray to optical flux ratios. As a consequence, we cannot sensitively search our stellar sample for possible anomalous X-ray emission which could be the signature of neutron star or black hole accreting binaries in quiescence for instance. However, neglecting all reddening effects, the $\log(f_x/f_r)$ distribution of our active coronae appears fully consistent with that of ChaMPPlane stellar identifications in the direction of the Galactic bulge (Koenig et al. 2008).

Despite their fully convective interior structure, the X-ray activity of very low mass M dwarfs shows similar trends to more massive stars, for example an ultra-cool M9 star has been detected in X-rays at a quasi-quiescent level (Robrade & Schmitt 2009). Although F, G and K-type stars display higher X-ray

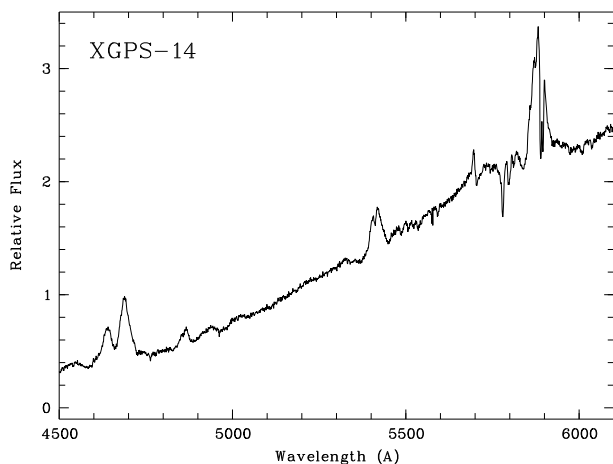


Fig. 5. The WHT optical spectrum of the WN8 counterpart of XGPS-14.

luminosity than M dwarfs, only the “tip of the iceberg” of the stellar coronal population has been sampled here. In terms of the likely composition of X-ray source catalogues, it is probable that M dwarfs will overwhelmingly outnumber other stellar categories at faint X-ray fluxes.

The high fraction (~50%) of M stars found among active coronae in the XGPS is at variance with the results of the ROSAT Galactic plane survey (Motch et al. 1997), which recorded only 19% of M-type identifications. It is, however, known from X-ray stellar population models (Guilout et al. 1996) that the contribution of M stars rises with increasing sensitivity. However, considering the small number of stars in each class, it is difficult to make a detailed comparison with the stellar-content inferred for published X-ray surveys covering other segments of the Galaxy and with different flux sensitivities.

5.1.2. XGPS-14: an X-ray selected Wolf-Rayet star

This X-ray source has previously been detected in the ASCA Galactic plane survey (Sugizaki et al. 2001) as entry AX J183116-1008, but has not been identified at other wavelengths. Our improved position shows it to be coincident with the southern component of a highly reddened visual binary at a separation of 15'' which consists of USNO-A2.0 0750-13397443 and USNO-A2.0 0750-13397376, the former being the actual optical counterpart of the X-ray source. According to the 2MASS (Cutri et al. 2003) and DENIS database¹², the observed optical/IR magnitudes of the counterpart are as follows: $B = 17.2$; $R = 13.4$ $I = 11.63 \pm 0.03$; $J = 9.09 \pm 0.03$; $H = 8.29 \pm 0.04$; $K = 7.63 \pm 0.02$, where the B and R magnitudes are deduced from photographic plates (USNO-A2.0 Catalogue, Monet & et al. 1998) and should accordingly be treated with caution. XGPS-14 is also identified with the GLIMPSE source SSTGLMA G021.6064-00.1970 (see Table 3).

A first optical spectrum shown in Fig. 32 was obtained at the ESO-3.6 m in 2003 with EFOSC2 and Grism#6 (see Table 4). Figure 5 shows the second, higher resolution spectrum ($FWHM$ resolution of ~ 2 Å). It was acquired on May 18, 2005 with the ISIS spectrograph attached on the William Herschel Telescope. On this occasion, the R300B grating was used in the blue arm with the EEV12 CCD. Our optical spectra confirm the highly reddened nature of the star and, furthermore, reveal strong broad emission lines typical of a Wolf-Rayet star. The presence of HeI,

HeII, and nitrogen emission lines and the lack of strong carbon lines defines a nitrogen-sequence WN star. Drawing on the spectral classification criteria described by Smith et al. (1996), the emission line ratio $\text{HeI}\lambda 5876/\text{HeII}\lambda 5411 > 1$ (where the $\lambda 5876$ component is furthermore diminished by interstellar Na I absorption) suggests a spectral type later than WN7, whereas the presence of NIV ions and the ratio $\text{NIV}\lambda 4057/\text{NIII}\lambda 4640$ (~ 0.3) constrains the spectral type to WN8. This classification is confirmed by comparison with the Vreux et al. (1983) near-IR-spectral-atlas of WR stars. The higher resolution WHT spectrum shows that the HeII emission lines do have a two-component structure or a central absorption component which might indicate (but do not necessarily imply) the presence of an early O type close binary companion. Given the intrinsic colours of an early-type star, which in the IR displays the Rayleigh-Jeans tail of a black body spectrum (here we use an O9 type star), we estimate the reddening $E(B - V) = 3.05 \pm 0.15$ towards XGPS-14 by fitting the B to K band photometry. A similar reddening is derived from the slope of the optical spectrum only. We note that the same colour excess is found for the northern component of the visual binary, which appears intrinsically redder and which on the basis of its IR colours (Koornneef 1983) is consistent with a late F-type supergiant.

The analysis of the EPIC pn and MOS observations of XGPS-14 is unfortunately limited by the short usable exposure time of the source, typically just a few thousand seconds at a large off-axis angle. Nevertheless the results are sufficiently interesting to be reported here. The source is in the field of view of the EPIC cameras in six observations, 0135741401, 0135744301, 0135744501, 0135746601, 0135741601 and 0135746301. However, apart for observations 0135741601 and 0135746301, the high flaring background or a position at the extreme edge of the field of view prevent the extraction of an X-ray spectrum. Owing to the position of XGPS-14 close to the edge of the field of view, we measured the background contribution in a circular area located on the same CCD and at slightly smaller off-axis angle. The small number of photons collected led us to use the Cash statistics. Fitting together or separately the EPIC pn and MOS data of the two observations yield consistent results. Models based on an absorbed thin thermal *mekal* spectrum or an absorbed power-law continuum are acceptable, although the former gives a slightly better fit. Using observation 0135746301 only, which displays the best signal-to-noise ratio, we find $kT = 2.14^{+1.09}_{-0.52}$ keV and $\Gamma = 2.91^{+0.96}_{-0.86}$ for the thin thermal temperature and the photon spectral index respectively. In both cases, the X-ray column densities $N_{\text{X}} = 5.21^{+1.38}_{-1.25}$ and $5.34^{+1.99}_{-1.68} \times 10^{22}$ H atoms cm^{-2} , respectively, are three times larger than the optical/IR derived value of $N_{\text{H}} = 1.7 \times 10^{22}$ atoms cm^{-2} , (assuming the canonical relation $N_{\text{X}} = 5.5 \times 10^{21} E(B - V)$ atoms cm^{-2} of Predehl & Schmitt (1995) corrected for $A_{\text{V}}/E(B - V) = 3.1$).

Using these spectral models we derive observed/unabsorbed 0.2–10 keV fluxes of $\sim 8.2 \times 10^{-13}/4.4 \times 10^{-12}$ erg cm^{-2} s^{-1} for the thin thermal *mekal* model. The temperature is significantly higher than the more typical values of < 1 keV observed from stellar-wind shocks in early (O and WR) type stars, but agrees with the values expected in colliding winds binaries (Skinner et al. 2007), which also tend to be more X-ray luminous than single O and WR stars.

A reliable estimate of the distance to XGPS-14 may be derived in at least two ways. Either the distance modulus can be established by comparing the unabsorbed magnitude to the absolute magnitude of the stellar type, or the distance can be

¹² <http://cdsweb.u-strasbg.fr/denis.html>

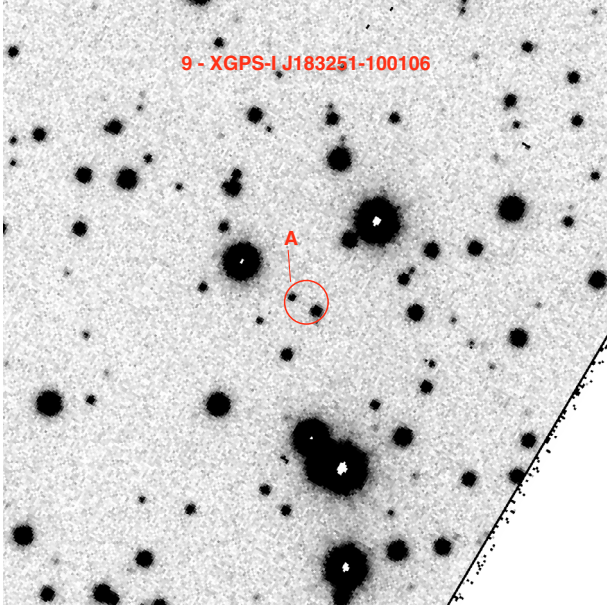


Fig. 6. A 2 min long ESO-VLT V band exposure showing the field of XGPS-9. The cataclysmic variable (object A) is the fainter of the two objects located in the 2XMM error circle. North is at the top and East to the left. The field of view shown is approximately $1' \times 1'$.

estimated by comparing the observed reddening to a previously determined relation between reddening/absorption and distance in the line-of-sight of the object in question. The latter may be derived from the absorption maps of Marshall et al. (2006). The distance determinations from the two methods are in agreement if we assume that the absolute magnitude M_V of a Galactic WN8 star lies in the range -6 to -7.2 , as suggested by Abbott & Conti (1987) and Hamann et al. (2006). The distance so-inferred using the optical/IR reddening/absorption is ~ 5 kpc. At this distance, the unabsorbed X-ray luminosity is $\sim 1.3 \times 10^{34}$ erg s $^{-1}$. This is more than 3 orders of magnitude brighter than observed from single WN8 stars (Oskinova 2005), but only slightly higher than the luminosities of several WR + O star colliding wind binaries (Skinner et al. 2007). The high X-ray output also leaves open the possibility of a WR + compact object binary that can reach up to several 10^{38} erg s $^{-1}$. Such systems are in vogue again since the discovery of the WR counterparts of IC 10 X-1 and NGC 300 X-1 (Carpano et al. 2007; Prestwich et al. 2007). In fact, we believe that XGPS-14 is among the very rare cases of an X-ray selected WR star. These are rare objects since only ~ 300 WR stars are known in the Galaxy. In a recent paper Shara et al. (2009) discuss the use of different near-infrared photometric techniques that allow them to discover 41 new WR stars. They fail, however, to detect any late WN (7-9) stars.

5.2. Cataclysmic variables

Three cataclysmic variables were positively identified in the XGPS survey; their properties are described in the following paragraphs.

5.2.1. XGPS-9

The optical finding chart for XGPS-9 is shown in Fig. 6. The optical spectrum of object A, the fainter of the two objects present in the X-ray error circle was acquired at the ESO-VLT

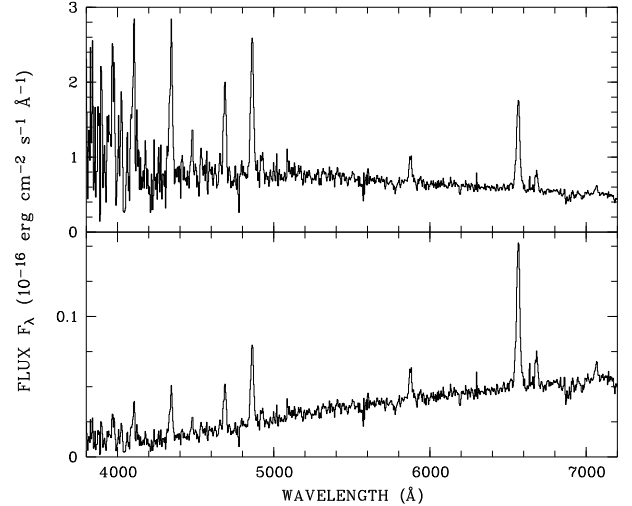


Fig. 7. Original (lower panel) and de-reddened (upper panel) identification spectra of XGPS-9. The upper spectrum was corrected for a reddening corresponding to the best X-ray N_H (8×10^{21} cm $^{-2}$).

using FORS2 and grism GRIS_300V. The observed and the de-reddened (see below) optical spectra are shown in Fig. 7. These spectra show the typical features of a magnetic cataclysmic variable, namely strong H, HeI and HeII emission, superposed on a blue continuum. We note that the spectrum does not show signs of the secondary star nor does it display evidence of cyclotron lines, which are sometimes seen in polar systems. If the orbital period were known, the size and mass of the secondary star could be determined and based on the non-detection of the secondary, a lower distance limit could be estimated.

The emission lines have an observed width of 21 \AA ($FWHM$), somewhat larger than the formal $FWHM$ spectral resolution of 12 \AA provided by grism GRIS_300V (see Table 4).

Due to its large off-axis angle, the source was not in the field of view of the optical monitor (OM) on XMM-Newton, an independent brightness determination of the counterpart is thus not possible. ESO-VLT imaging observations unfortunately lack proper photometric calibration. However, the counterpart is certainly very faint since the flux calibrated spectrum indicates $V \sim 23.3$.

To create an X-ray spectrum, photon events were extracted using a circular aperture of radius \sim one arcmin. The resulting count rate spectrum was binned with a minimum of 20 photons per bin to allow the application of the χ^2 statistic in the model fitting.

A one-component thermal plasma spectrum absorbed by cold interstellar matter provided a satisfactory fit to the data. The temperature was not well constrained and was thus fixed at 20 keV^{13} . The column density of the best fit is $N_H \sim 8 \times 10^{21}$ cm $^{-2}$ and the $0.2\text{--}12 \text{ keV}$ unabsorbed flux of the source was determined to be $F_X = 1.4 \times 10^{-12}$ ergs cm $^{-2}$ s $^{-1}$. Taking the fitted value of the column density at face value, the optical spectrum was de-reddened (see above) using the calibrations in Predehl & Schmitt (1995) (for A_V) and Cardelli et al. (1989) (for A_λ/A_V) and assuming $R = 3.1$ for Galactic dust.

The X-ray light curve shown in Fig. 8 was created with task *epiclccorr* (with dead-time and vignetting corrections applied) and has time bins of 600 s. There is evidence of variability of up

¹³ Unconstrained thermal plasma model fits of magnetic CVs tend to reveal unphysical high plasma temperatures due to reflection and/or warm absorption, see e.g. Schwarz et al. (2009); Staude et al. (2008)

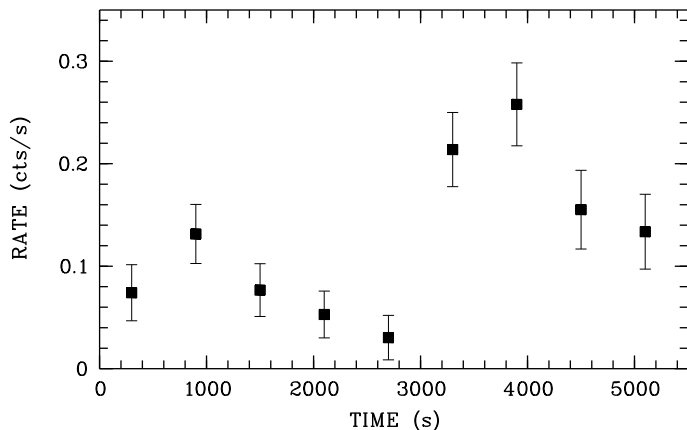


Fig. 8. EPIC pn X-ray light curve of XGPS-9 with bin size 600 s.

to 100% on a timescale as short as a few 100 s. Unfortunately, an estimate of any periodic behaviour (orbital period or spin period of the white dwarf) is not possible given the rather short X-ray observation and the low count rate.

Taking all facets together, the source XGPS-9 is almost certainly a magnetic cataclysmic variable. A final classification, AM Her type or DQ Her type (polar or intermediate polar), i.e. with synchronously or asynchronously rotating white dwarf, would need measurements of both the orbital period and the spin period of the white dwarf. The absence of a soft X-ray spectral component, a prominent defining feature for polars in the ROSAT era does not rule out the classification of XGPS-9 as a polar. Follow-up observations of definite polars with XMM-Newton revealed a $\sim 30\%$ fraction without a soft component (Ramsay & Cropper 2004). To the best of our knowledge XGPS-9 is the first magnetic CV to have been uncovered in the 2XMM/2XMMi catalogue as a result of a dedicated optical identification programme. However, previously two rather bright eclipsing polars were discovered amongst the 2XMM sources due to their prominent X-ray variability (Vogel et al. 2008; Ramsay et al. 2009).

5.2.2. XGPS-24 and XGPS-65

We show in Fig. 9 and Fig. 10 the finding charts for sources XGPS-24 and XGPS-65, respectively. The VLT spectra obtained with FORS2 and grism GRIS_300V for the respective counterparts are reproduced in Figs. 11 and 12. The optical spectra of the counterparts of sources #24 (object B) and #65 USNO-B1.0 0789-0404378 are very similar. Both show hydrogen Balmer (α, β, γ) and He I ($\lambda\lambda 5875, 6678$) emission lines on a reddened smooth continuum. The absence of He II emission suggests a classification as non-magnetic cataclysmic variables, i.e. disc CVs whose X-ray emission likely originates from the boundary layer between the disc and the accreting white dwarf. A further division according to CV subclass is not possible/reliable given the sparse observational data base.

However, following Patterson (1984) we estimate the absolute brightness M_V of the accretion disc from the observed equivalent width of the H β line, $EW(H\beta) = 0.3M_V^2 + \exp(0.55(M_V - 4))$. Using the same observable the X-ray to optical flux ratio may be inferred with the empirical relation of Patterson & Raymond (1985): $\log(F_X/F_V) = -2.21 + 1.45 \log(EW)$. Measurements and results are compiled in Table 6.

Many caveats have to be made when interpreting the numbers in Table 6. Patterson's $EW-M_V$ relation displays a high

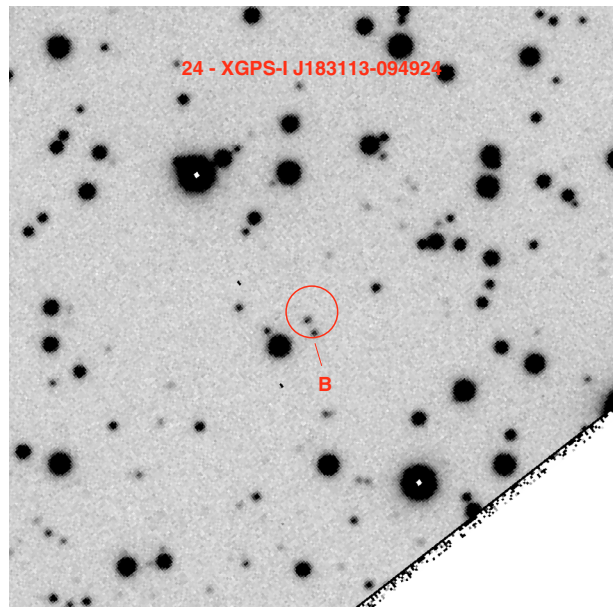


Fig. 9. A 2 min long ESO-VLT V band exposure showing the field of XGPS-24. The CV counterpart of the X-ray source (object B) is the object located at the South-West. North is at the top and East to the left. The field of view shown is approximately $1' \times 1'$.

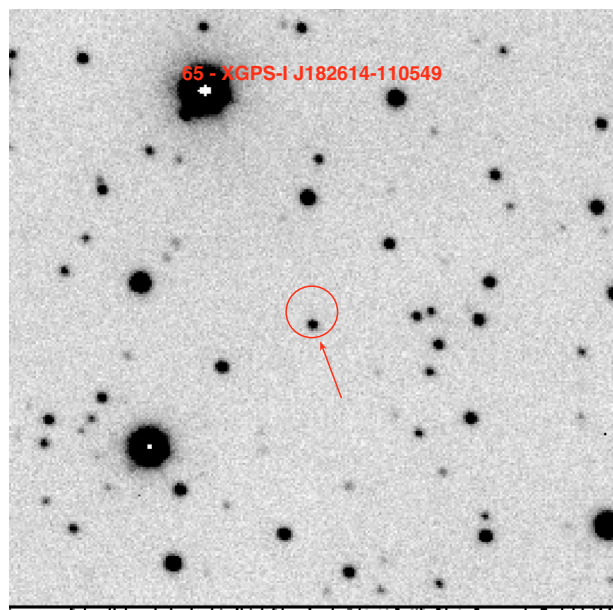


Fig. 10. A 2 min long ESO-VLT V band exposure showing the field of XGPS-65. The CV counterpart of the X-ray source, USNO-B1.0 0789-0404378, is marked. North is at the top and East to the left. The field of view shown is approximately $1' \times 1'$.

scatter by 1.5 mag above $EW \sim 15 \text{ \AA}$, and it is even less certain at lower widths. The apparent B and V magnitudes were derived from the observed spectra by folding those through model filter curves and are probably accurate to about 30%. The biggest uncertainty is the rather unconstrained A_V . Some constraints on the absorbing column density can be derived from the X-ray spectra. They are compatible with a one-component thermal spectrum with $kT \geq 5 \text{ keV}$. Fixing the temperature at 5 keV, $N_H \sim (0.2-2.4) \times 10^{22} \text{ cm}^{-2}$ for XGPS-24 and $\sim (0.8-2.4) \times 10^{22} \text{ cm}^{-2}$

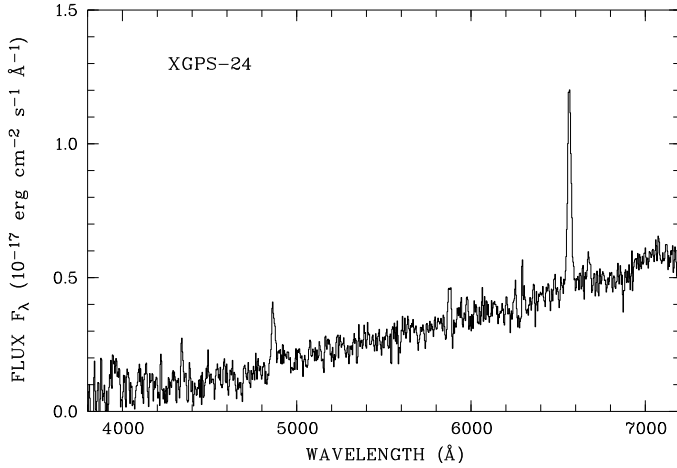


Fig. 11. Identification spectrum of XGPS-24 (i.e., of object B).

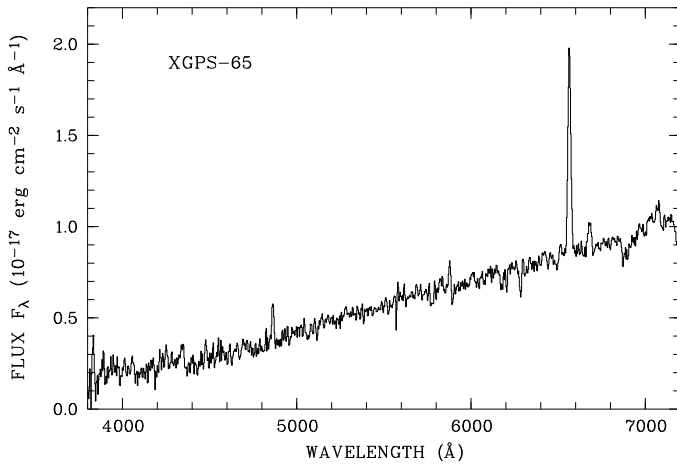


Fig. 12. Identification spectrum of XGPS-65 (i.e., of USNO-B1.0 0789-0404378).

Table 6. $H\beta$ equivalent widths (in \AA) and derived quantities for the non-magnetic CVs XGPS-24 and -65.

XGPS	B	V	$EW(H\beta)$	M_V	$\log(F_X/F_V)$	A_V	D/kpc
24	24.3	22.8	-25 ± 5	7.6 ± 0.6	-0.18	1–5	7–1.1
65	23.4	22.0	-9 ± 1	5 ± 0.3	-0.82	1–5	16–2.5

for XGPS-65, implying $A_V = 1\text{--}13$ using the calibration of Predehl & Schmitt (1995).

Alternatively, $E(B - V)$ and A_V can be estimated using the observed $B - V$ colour of the systems as derived from the spectrophotometry and an assumed intrinsic colour. Assuming $(B - V)_0 \simeq 0.3$ (Tylenda 1981) and $R_V = 3.1$ for Galactic dust, $A_V \simeq 4$ for the two systems. In Table 6 distance limits are derived for the range $A_V = 1\text{--}5$ using M_V derived from Patterson’s $EW\text{--}M_V$ relation.

The X-ray spectral parameters yield an unabsorbed 0.2–12 keV spectral flux of a few times 10^{-13} $\text{erg cm}^{-2} \text{s}^{-1}$, which at the lower limit distance estimates of 1.1 and 2.5 kpc listed in Table 6 give luminosities of $(1\text{--}5) \times 10^{31}$ erg s^{-1} . Values in that range are expected for nova-like CVs or dwarf novae in quiescence and we propose such an identification for the two systems.

5.3. Candidate high-mass X-ray binaries

Einstein and ROSAT all-sky survey observations of OB stars (Pallavicini et al. 1981; Berghoefer et al. 1997) have established a rather well defined relation between X-ray and stellar bolometric luminosities, $L_X \sim 10^{-7} \times L_{\text{bol}}$, with maximum X-ray (0.1–2.4 keV) luminosities of the order of a few 10^{32} erg s^{-1} for the hottest O-type stars. X-ray spectra are adequately described by multi-temperature thin thermal emissions. When fitted with a single temperature component, the mean kT is $\sim 0.2\text{--}0.6$ keV for O stars and $kT \sim 1$ keV for B stars (see e.g. Nazé 2009, for a recent survey of XMM-Newton observations). The XGPS sources listed in this section display properties departing from those of normal early type stars, either based on their high X-ray luminosities in excess of several 10^{33} erg s^{-1} or on the basis of an unusually hard X-ray spectrum. Extreme wind collisions such as proposed for the X-ray selected WR star XGPS-14, may explain the observed properties to some extent. However, the high L_X and/or the X-ray hardness combined with the absence of WR signatures and evidence of Balmer emission suggest the presence of a compact object accreting from a circumstellar disc as in “classical” Be/X-ray systems (see Neuguera 2007, for a recent review) or from the massive stellar wind of a supergiant star (Corbet 1986). Our sample includes four tentative identifications of X-ray binaries with high mass primaries. We outline below the supporting evidence for each of these sources.

5.3.1. XGPS-3

The XMM-Newton source position coincides with a radio source detected in the 1.4 GHz survey of Zoonematkermani et al. (1990) and the 5GHz VLA survey of the Galactic plane (Becker et al. 1994). It also matches with the ASCA Galactic plane survey detection AX J1832.1-0938 (Sugizaki et al. 2001). The X-ray source is identified with GSC2 S300302241761/2MASS 18320893-0939058 with a probability greater than 98% (see optical finding chart in Fig. 33). Our optical spectrum (Fig. 13) shows that this relatively bright star ($R = 16.80 \pm 0.45$) exhibits a very strong $H\alpha$ emission line (EW of -104\AA) superposed on a highly reddened continuum and is indeed the likely optical counterpart of the X-ray source. Stephenson (1992) also reports a strong near infrared excess and identify this star with IRAS 18293-0941. The source is also present in the DENIS survey ($I = 12.325 \pm 0.020$). Its 2MASS magnitudes are very bright with $J = 7.05 \pm 0.007$, $H = 5.49 \pm 0.015$ and $K = 4.34 \pm 0.027$. We show in Fig. 14 the 5.8μ image acquired by the IRAC instrument on board Spitzer, which illustrates the high infrared brightness of the counterpart. Amazingly, this bright source is not found in both the “reliable” and “less reliable” versions of the final 2007 GLIMPSE I catalogue available at IPAC. This absence might be due to the fact that saturation did not allow clean extraction of the infrared parameters.

In addition to the prominent $H\alpha$ line, our spectrum exhibits HeI emission lines at $\lambda 6678$ and $\lambda 7065 \text{\AA}$ (Fig. 14). The absence of any visible photospheric absorption features makes spectral classification extremely difficult. Furthermore, since our discovery spectrum was acquired with EFOSC2 and grism #6, the wavelength range does not cover the Paschen line region. Model spectra of B to K giant stars can reasonably well account for the slope of our optical spectrum assuming a large $E(B - V)$ in the range of 5 to 7. Later spectral types would display TiO bands which are not detected in the red part of our spectrum. We plot in Fig. 15 the overall optical to infrared energy distribution of the star, using our own flux calibrated spectrum, and

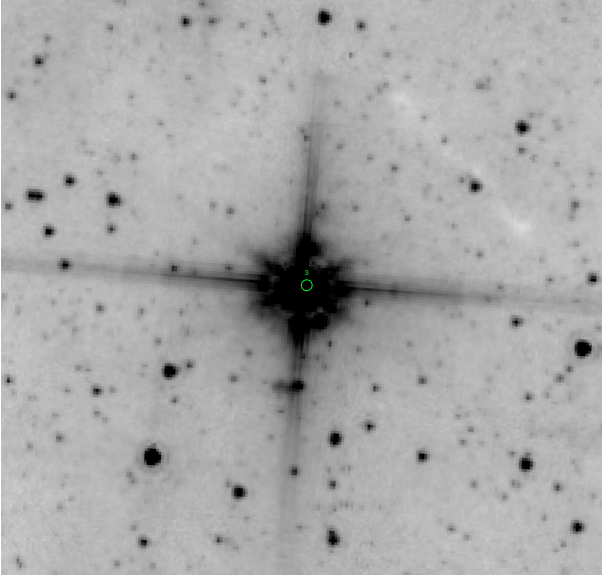


Fig. 13. The 5.8μ image of the field of XGPS-3 as seen by Spitzer. North is at the top and East to the left. The field approximately covers 4×4 arcmin.

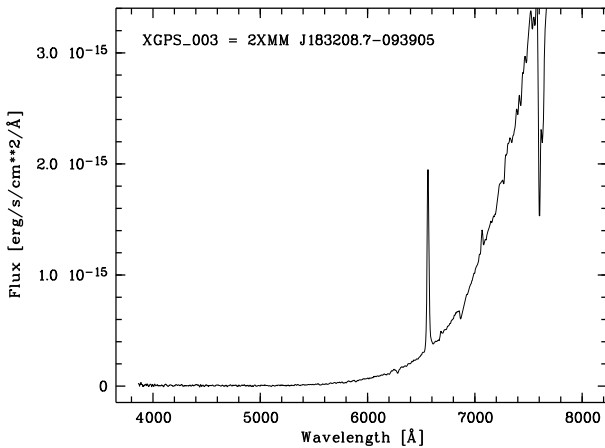


Fig. 14. The observed optical spectrum of XGPS-3.

GSC 2.2, DENIS, 2MASS and IRAS photometry, together with a theoretical model for a O6I star (Castelli & Kurucz 2004). In fact good fits are obtained with model energy distributions corresponding to super-giant O6 to K0 stars. However, in all cases, the 12 and 25μ IRAS fluxes seem an order of magnitude above model expectations and might be indicative of a cool dusty circumstellar envelope. Assuming that the underlying spectrum is that of an early type OB star implies $E(B - V) \sim 7.0$ while a G0I star would still require $E(B - V) \sim 6.0$. Such a high reddening, if not intrinsic to the source indicates astonishingly large distances and accordingly a very high luminosity. To find the distance corresponding to this reddening we used both the 3D extinction model of Drimmel et al. (2003)¹⁴ based on FIR COBE/DIRBE data and that of Marshall et al. (2006) relying on a modelling of the giant stellar population detected at large distances by 2MASS. Both models predict that $E(B - V) \sim 7$ is reached between 8 and 9 kpc. At this distance the absolute K magnitude of the star reaches an exceptional value of

¹⁴ In general, we prefer to use Marshall's determinations which are not sensitive to variations of dust temperature along the line of sight.

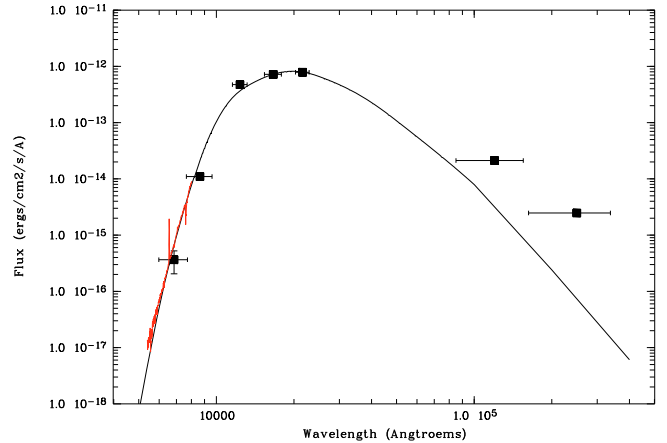


Fig. 15. The spectral energy distribution of the optical counterpart of XGPS-3. Data points show the 2MASS and IRAS photometry, while the optical spectrum is plotted. The continuous line represents the theoretical energy distribution of a O6I star with $E(B - V) = 6.9$.

$K_0 = -12.4$. Interestingly, Lockman et al. (1996) note the presence of a nearby HII region [LPH96] 022.162-0.157, only 33 arcsec away from XGPS-3. The HII region has two velocity components which, using the velocity distance relation of Anderson & Bania (2009), imply a distance of either 4.8 kpc or 9 kpc, the latter being close to that estimated from the reddening.

We reprocessed the XMM-Newton data of observation 0135741701. Only the MOS detectors were on at the time of this observation with both medium filters deployed. XGPS-3 is detected with a count rate of 0.13 ct/s. However, the modest exposure time of 6.9 ks and a strong vignetting due to the large off-axis angle of the source yields only about 300 photons in each MOS camera. We thus grouped the X-ray spectra with a minimum of 15 counts per channel and used the XSPEC C statistics for fitting. A power-law model (see Fig. 16) provides a good fit to the MOS spectra with a photon index of $1.45^{+0.42}_{-0.40}$ and a strong photoelectric absorption of $N_H = 2.69^{+0.76}_{-0.67} \times 10^{22} \text{ cm}^{-2}$ (90% confidence level). A thin thermal (*mekal*) energy distribution also provides a good fit to the observed spectra with $kT = 4.2 \pm 0.6 \text{ keV}$, when N_H is fixed at the value inferred from the optical/infrared reddening ($E(B - V) = 7$ or $N_H \sim 3.8 \times 10^{22}$). Assuming a power-law model, the observed 0.2–10 keV flux is $3.2 \times 10^{-12} \text{ erg cm}^{-2} \text{ s}^{-1}$ equivalent to an unabsorbed 0.2–10 keV flux of $5.6 \times 10^{-12} \text{ erg cm}^{-2} \text{ s}^{-1}$. The corresponding X-ray luminosity is $L_X = 6.7 \times 10^{34} (\text{d}/10 \text{ kpc})^2 \text{ erg s}^{-1}$, corrected for interstellar absorption. It may be noted that the flux ($1.97 \times 10^{-12} \text{ erg cm}^{-2} \text{ s}^{-1}$; 0.7–10 keV) and spectral shape (photon index = $3.67^{+0.76}_{-0.69}$ and $N_H = 5.48^{+1.87}_{-1.47} \times 10^{22} \text{ atoms cm}^{-2}$) observed by ASCA are not consistent with the XMM-Newton values and provide evidence of long-term flux and spectral variability. No significant flux variability is detected during the ~ 2 h XMM-Newton observation.

Taken at face value, the large reddening and inferred distance imply that the optical counterpart is a rare super-giant star with an extreme luminosity. The overall observational picture presented by XGPS-3 is clearly reminiscent of that of η Carina, which displays similar optical and X-ray luminosity and X-ray spectral shape (Davidson & Humphreys 1997; Chlebowski et al. 1984). By analogy with the model favoured to explain the absorbed high-energy emission from η Carina, we may speculate that wind collision in a binary system may be at the origin of the copious X-ray emission. For XGPS-3, however, we would expect a different viewing condition to the X-ray source, since

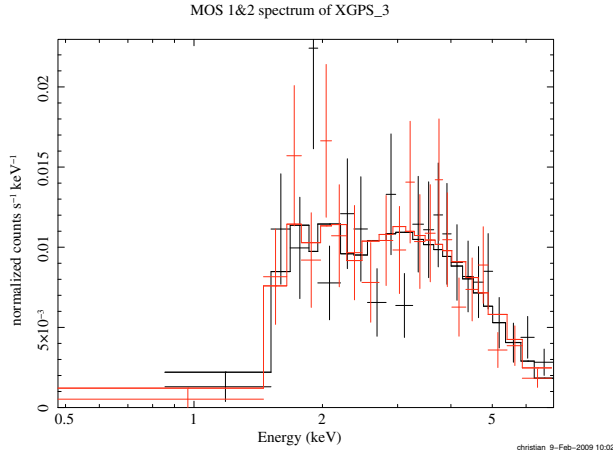


Fig. 16. The MOS 1 (black) and MOS 2 (red) spectra of XGPS-3 fitted with a power law of photon index 1.45 and $N_{\text{H}} = 2.7 \times 10^{22} \text{ cm}^{-2}$.

the photoelectric X-ray absorption, is consistent (at least for the thermal model) with that seen in the optical/infrared range. The detection of radio emission also fits well in this picture since η Carina itself is a strong variable radio emitter (Duncan & White 2003, and references therein). Alternatively, assuming that the star is a more common dwarf or giant hot star, then the strong intrinsic X-ray absorption and optical reddening would suggest that a cocoon of absorbing matter surrounds the source.

However, the high inferred X-ray luminosity is also consistent with a scenario in which a compact object, a neutron star or a black hole, accretes matter from the dense wind of an early type companion star.

5.3.2. XGPS-10

This source is located in the field designated XGPS-2 (nb recall that the XGPS field names are not related to the source numbering system employed here). Although the source position and finding charts produced by an early (2001) version of the standard analysis are available, the observation data unfortunately suffer from an ODF description problem which prevents it from being processed by the current pipeline. XGPS-10 is thus not in the 2XMM or 2XMMi catalogues. However, at the telescope we used the position and associated errors computed by the 2001 pipeline (RA = 18 27 45.49, Dec = -12 06 06.7 and a 90% error radius of 2.3") which is fully consistent with that listed in the XGPS-I catalogue while providing a smaller error radius. The XGPS MOS-based hardness ratio of this source is 0.56, indicative of a hard spectrum but not the degree of absorption expected for a background extragalactic object (assuming a $\Gamma = 1.7$ power law energy distribution). The two faint candidates A and B, are shown in Fig. 17. The third faintest object to the North [of candidate A] was not spectroscopically observed. Candidate B shows $H\alpha$ in absorption and no evidence for Paschen lines, suggesting a rather late type star. Because of the relatively large reddening, the G band could not be measured. The absence of strong Mg “b” feature suggests a possible F-G spectral type. However, candidate A might exhibit a double-peaked $H\alpha$ line in emission and shows high-order Paschen absorption lines (see Fig. 18) consistent with an early B spectral type or with a \sim mid F type star (Fremat et al. 1996). XGPS-10 has no match with 2MASS stars within 5 arcsec. There is however a GLIMPSE source at RA = 182745.44 and Dec = -12 06 06.3 detected only in the 3.6 μ and 4.5 μ bands. Its position is consistent with either candidate A or the fainter object to the north. Assuming

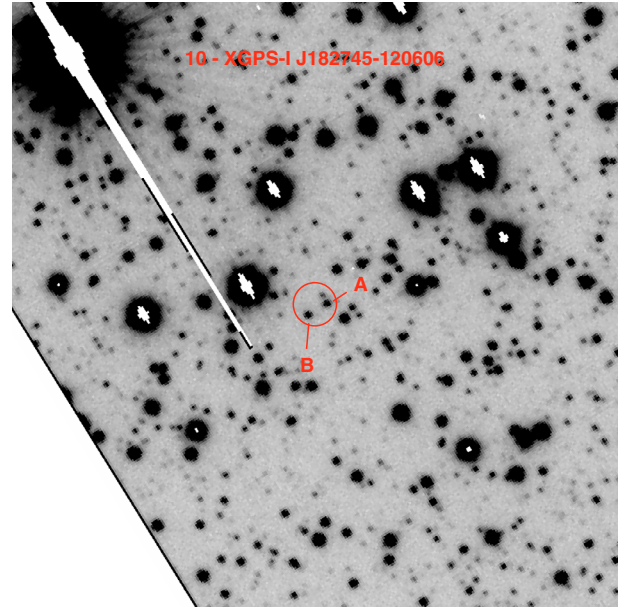


Fig. 17. A 20 s long ESO-VLT white light exposure showing the field of XGPS-10 and the position of candidates A and B. North is at the top and East to the left. The field approximately covers 1×1 arcmin. The position and 90% confidence radius shown here are those produced by the 2001 version of the XMM-Newton pipeline.

that the GLIMPSE source is indeed candidate A yields an optical to infrared energy distribution suggesting $E(B-V) \sim 3.9$ and $E(B-V) \sim 3.2$ for a B0V and a F2V star respectively. Fitting the spectral distribution to the flux calibrated optical spectrum alone yields a slightly smaller value of the reddening of $E(B-V) \sim 3$ and $E(B-V) \sim 2.2$ for a B0V and a F2V star respectively. The estimated V band magnitude of candidate A ($V \sim 23.7$) would imply distances of the order of 10 kpc assuming an early type star. Such a large distance is in fact consistent with a total A_V of 12.1 derived by Marshall et al. (2006), since in this direction the line of sight appears much clearer than towards source XGPS-3. The unabsorbed 0.2–10 keV X-ray luminosity is of the order $L_X \sim 3.7 \times 10^{34} (\text{d}/10 \text{ kpc})^2 \text{ erg s}^{-1}$, assuming a spectral shape similar to that of XGPS-3. Overall, the observational picture could be consistent with a Be/X-ray system in quiescence. However, considering the need to confirm the Balmer emission of candidate A we regard the identification of XGPS-10 with a high-mass X-ray binary as uncertain.

5.3.3. XGPS-15

Two relatively bright stars occupy the error circle (see Fig. 19). We tentatively identify the X-ray source with the object located on the Eastern side, which is also 2MASS 18281430-1037288 and identical to the GLIMPSE source SSTGLMA G020.8457+00.2476. The formal probability of identification of XGPS-15 with the 2MASS entry is 55% and therefore the association cannot be proven solely on the basis of positional coincidence. Our optical spectrum reveals a heavily reddened flux distribution. It shows rather clear evidence for $H\alpha$ emission (see Fig. 20) with an equivalent width of $\sim -1.9 \text{ \AA}$ and, again, high order Paschen lines in absorption with depths consistent with those expected from an early B0V type star. In contrast, the optical spectrum of the western star, which is the brightest in the optical, exhibits a much less reddened continuum and $H\alpha$ in absorption. The slope of the optical spectrum of the candidate 2MASS identification indicates $E(B-V) \sim 5.0$,

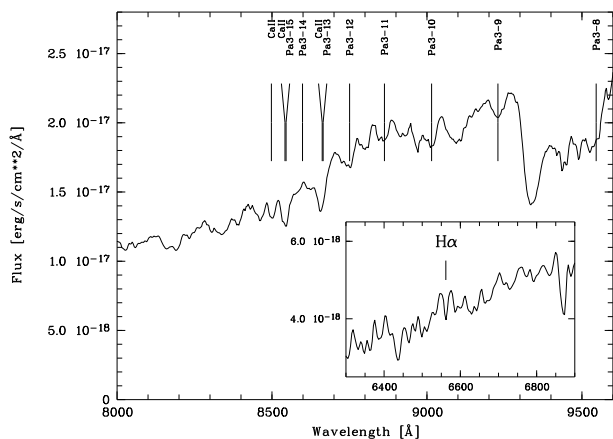


Fig. 18. Red part of the ESO-VLT FORS2 spectrum of candidate A for XGPS-10 displaying evidence of Paschen absorption lines. The CaII triplet is mostly of interstellar origin (spectrum filtered with a 10 \AA window). Inset: the $H\alpha$ region (spectrum filtered with a 3.3 \AA Gaussian).

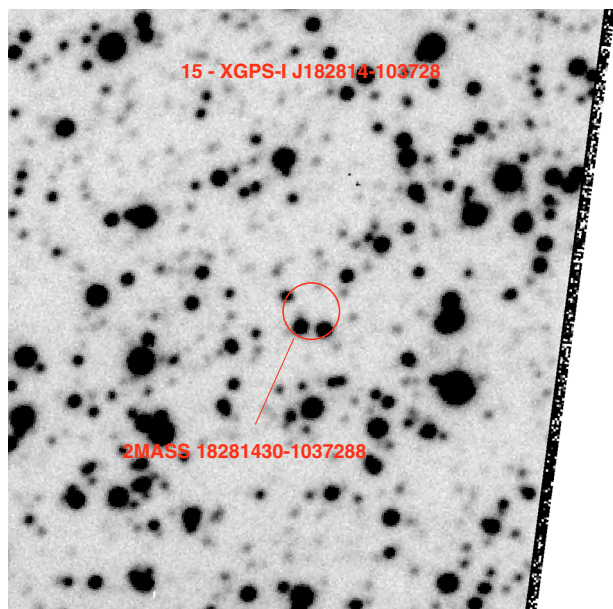


Fig. 19. A 30 s long ESO-VLT I band exposure showing the field of XGPS-15. The proposed optical counterpart is the 2MASS source. North is at the top and East to the left. The field approximately covers 1×1 arcmin.

assuming an early B-type stellar continuum. The optical and GLIMPSE energy distribution are indeed well represented by a $T_{\text{eff}} = 30\,000 \text{ K}$ stellar atmosphere model (Castelli & Kurucz 2004) subject to $E(B - V) \sim 5.0$ (see Fig. 21).

The fact that the 2MASS photometry does not fit the model suggests the presence of an interloper within the 2MASS photometric radius or the existence of variability. With an estimated $R \sim 22.2$ derived from the optical spectrum, a B0V star would be located at $\sim 5 \text{ kpc}$ for a total absorption of $A_V = 15.8$. However, this reddening is reached at a distance of $\sim 10 \text{ kpc}$ in that direction (Marshall et al. 2006) for which the absolute K magnitude of ~ -5.3 would then indicate a giant or super-giant star.

The large off-axis position and relative faintness of the source limits the constraints that can be derived from the shape of the X-ray energy distribution. A power law adequately fits the combined data from the three EPIC cameras ($\chi_r^2 = 1.27$) and gives $N_H = 7.8^{+5.9}_{-3.4} \times 10^{22} \text{ cm}^{-2}$ with a photon index of $2.4^{+1.5}_{-1.0}$.

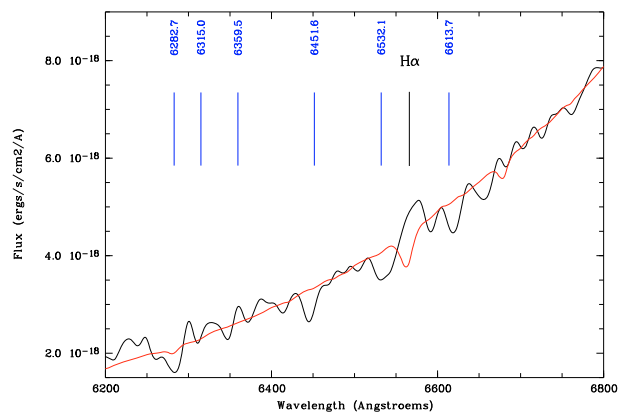


Fig. 20. Black line; combined GRIS_300I and GRIS_300V optical spectrum of 2MASS 18281430-1037288, the possible counterpart of XGPS-15, obtained at ESO-UT4 and smoothed with a $\sigma = 5 \text{ \AA}$ Gaussian filter. Red line; the best fit spectrum of a reddened B0V star. Blue labels show the positions of the strongest interstellar absorption bands.

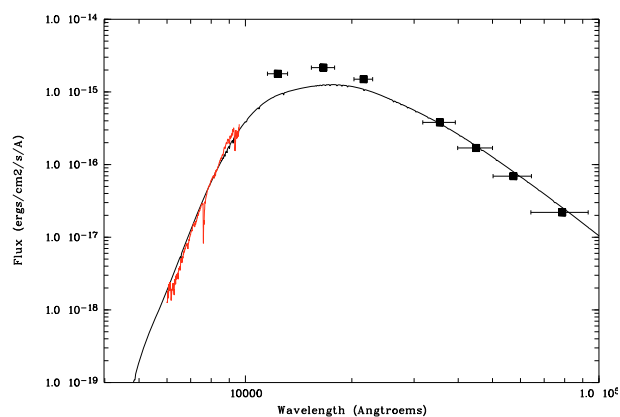


Fig. 21. The spectral energy distribution of the possible optical counterpart of XGPS-15. Data points show the 2MASS and GLIMPSE photometry, while the optical spectrum is plotted in red. The continuous line represents a theoretical energy distribution of a B0V star with $E(B - V) = 5.0$.

The corresponding unabsorbed X-ray luminosity is $L_X \sim 5.4 \times 10^{34} (\text{d}/10 \text{ kpc})^2 \text{ erg s}^{-1}$ ($0.2\text{--}12 \text{ keV}$). In the direction of XGPS-15, the total Galactic absorption is $\sim 6.4 \times 10^{22} \text{ cm}^{-2}$ and therefore the X-ray spectrum could be consistent with an extragalactic origin if the early type star is simply a chance interloper.

If the identification of XGPS-15 with 2MASS 18281430-1037288 were confirmed, the reddening of the optical candidate ($E(B - V) \sim 5.0$) implies $N_H \sim 2.8 \times 10^{22} \text{ cm}^{-2}$ (Predehl & Schmitt 1995) and would suggest the presence of an additional local absorption in the X-ray domain, as is sometimes seen in the super-giant high-mass X-ray binaries discovered by INTEGRAL (see e.g. Walter et al. 2006). An identification with a giant star could be consistent with the absence of strong infrared excess in the Spitzer bands. An accreting Be/X-ray system would probably exhibit a noticeable excess of infrared emission from the circumstellar disc.

5.3.4. XGPS-36

A bright optical object, GSC2 S300302371, occupies the error circle (see finding chart in Fig. 33). Its optical spectrum (see Fig. 32) was unfortunately not acquired under the best

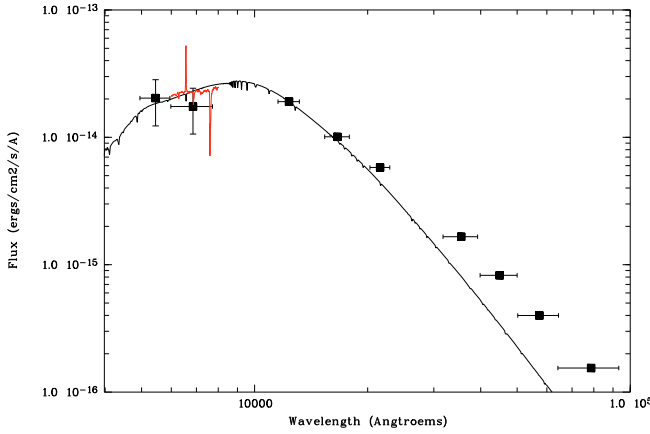


Fig. 22. The spectral energy distribution of the optical counterpart of the Be/X-ray source XGPS-36. Data points show the GSC2.2, 2MASS and GLIMPSE photometry, while the optical spectrum is plotted in red. The continuous line represents a theoretical energy distribution of a B1V star with $E(B - V) = 1.5$.

conditions. The continuum shape of the flux-calibrated spectrum is distorted as the slit was not aligned to the parallactic angle, and the observation was carried out under non-photometric conditions. Many diffuse interstellar bands are visible. The equivalent width of the $\lambda 5780$ and $\lambda 6613$ Å lines are consistent with $E(B - V) \sim 1.5$ (Herbig 1975). Balmer absorption lines are also clearly visible blue-ward of $H\beta$. Several HeI absorption lines are seen with equivalent widths suggesting an early B type star. The $H\alpha$ line is strongly in emission with an equivalent width of 27 Å. The overall spectral energy distribution (SED) based on the optical, 2MASS and GLIMPSE data (see Table 3) is shown in Fig. 22. Assuming $E(B - V) = 1.5$, the B to H band flux distribution fits well that of a $T_{\text{eff}} 25\,000$ K model (Castelli & Kurucz 2004) corresponding to a B1V star. However, the SED shows evidence for an infrared excess starting red-wards of 2μ which may indicate the presence of a large circumstellar envelope. A B1V star would need to be at ~ 2.6 kpc to account for the [K -band] 2MASS observed magnitude of 9.67. Interestingly, the 3D absorption map of Marshall et al. (2006) indicates that the reddening of $E(B - V) = 1.5$ is reached at about 2.5 kpc, fully consistent with the photometric distance.

The 2XMM EPIC pn hardness ratios (see Sect. 6) reveal a rather hard X-ray spectrum with, for EPIC pn, $HR2 = 0.882 \pm 0.430$; $HR3 = 0.613 \pm 0.211$ and $HR4 = -0.039 \pm 0.196$. Assuming a power-law energy distribution with a photon index of 1.9 and a column density fixed at the optically derived $E(B - V)$, the observed flux of $2.57 \pm 0.34 \times 10^{-13}$ erg cm $^{-2}$ s $^{-1}$ yields an unabsorbed X-ray luminosity of 3.4×10^{32} (d/3 kpc) 2 erg s $^{-1}$ (0.2–12 keV). The overall observational picture, spectral type, equivalent width of the $H\alpha$ line, X-ray hardness ratios and luminosity, clearly suggest that XGPS-36 is another member of the growing class of γ -Cas analogues, a group of early Be stars exhibiting very hard thermal X-ray emission ($kT \sim 10$ keV) and X-ray luminosities of a few 10^{32} erg s $^{-1}$ (Lopes de Oliveira et al. 2006; Motch et al. 2007a).

5.4. Candidate low-mass X-ray binaries

5.4.1. XGPS-1

This source is coincident in position with SAX J1828.5-1037 (Cornelisse et al. 2002) which is known to exhibit X-ray

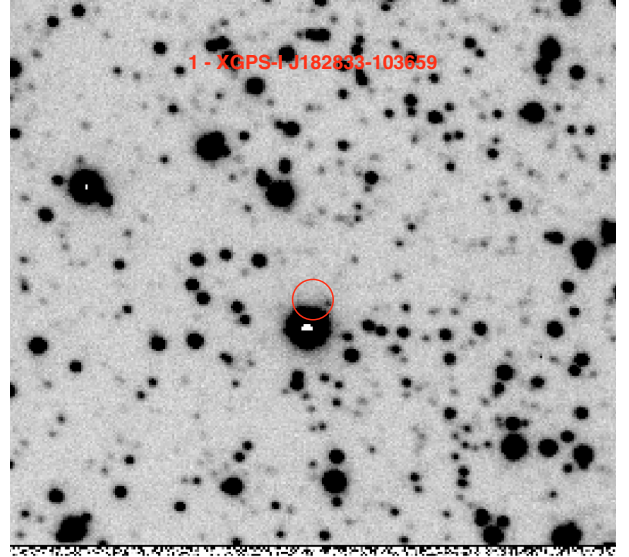


Fig. 23. A 30 s ESO-VLT I band exposure showing the 2XMM position of the bright X-ray transient [here designated XGPS-1]. North is at the top and East to the left. The field approximately covers 1×1 arcmin.

bursts. It belongs to the growing class of very faint X-ray transients (Sakano et al. 2005; King & Wijnands 2006) whose exact nature remains uncertain. An optical spectrum of GSC2 S300302034199, the bright star located slightly outside the 2XMM 90% confidence error circle (see Fig. 23) shows that the object is a normal G-type star and thus unrelated to the X-ray source. The faint object in the error circle located to the north-west of GSC2 S300302034199 has $I \sim 21.6$. The absence of a bright optical counterpart is consistent with a low-mass X-ray binary type and a large interstellar absorption.

5.4.2. XGPS-25

XGPS-25, alias 2XMM J182854.6-112656, is identified with a relatively bright object ($R \sim 17.05$) detected in the USNO and GSC2 R band and 2MASS and DENIS infrared surveys but with no GLIMPSE counterpart (see optical finding chart in Fig. 33). A radio source detected in the Parkes-MIT-NRAO (PMN) catalogue (Griffith et al. 1994, source catalogue for the tropical survey ($-29^\circ < \Delta < -9.5^\circ$) at 4850 MHz) is found 20.2'' away from the X-ray source and owing to the error on the radio position, could still be associated with the 2XMM source. The optical spectrum exhibits a wealth of interstellar bands suggesting a rather strong reddening. In addition to the $H\alpha$, $H\beta$ and $\lambda 6678$ HeI emission lines, there is clear evidence for the $\lambda 4686$ HeII and $\lambda 4630$ -4660 CIII-NIII Bowen complex high excitation lines. The equivalent widths remain modest ranging from -4.3 Å for $H\alpha$ to ~ -1.1 Å and -0.9 Å for $H\beta$ and HeII respectively. The optical candidate is only detected in the DENIS I and J bands, with only non-constraining upper limits available in the 2MASS H and K bands. Although the flux derived from the GSC2.2 R band appears fully consistent with that of our calibrated spectrum, the I and J band seem about ~ 0.4 mag brighter than the extrapolation toward longer wavelengths of the optical spectrum, suggesting some long term variability. The optical spectrum and the I and J flux can be independently fitted by a B0V star energy distribution undergoing $E(B - V) \sim 1.5$.

XGPS-25 was only detected in observation 0051940601 which, unfortunately, suffers from a large background flare. The combined EPIC spectrum gathers 1.7 ks and 3.8 ks of usable pn and MOS exposure time. Owing to the few counts we used the C statistics in *XSPEC*. The energy distribution of XGPS-25 is extremely hard with a power-law photon index of $1.07^{+0.32}_{-0.32}$ or a thin thermal temperature in excess of 10 keV with N_{H} ranging from 1 to $8 \times 10^{21} \text{ cm}^{-2}$. The upper range of N_{H} is compatible with the $E(B-V)$ estimated from the slope of the optical flux calibrated spectrum. In the direction of the source, $E(B-V) = 1.5$ is reached in the distance range of ~ 2 to 4 kpc (Marshall et al. 2006), yielding $M_{\text{R}} \sim 0.6-2.1$, while the unabsorbed X-ray luminosity would be $\sim 4.3 \times 10^{32} \text{ erg s}^{-1}$ at 3 kpc.

XGPS-25 is clearly not a high-mass system and the determination of its true nature requires further observations. The X-ray luminosity and spectral shape are consistent with those expected from a cataclysmic variable of the intermediate polar type (see e.g. Patterson 1994). However, the likely high optical brightness of the counterpart seems at first glance inconsistent with a CV nature (Warner 1987). Although some old novae and novae-like systems do exhibit the NIII-CIII complex in emission (Williams & Ferguson 1983) as well as some AM Her systems (Schachter et al. 1991), the high relative strength of the Bowen complex compared to HeII 4686 is at odds with what is observed in CVs. In addition, the X-ray emission of novae-like systems arising from shocks in the boundary layer between the accretion disc and the white dwarf usually have soft thermal energy distributions at variance with that observed in XGPS-25. Although some symbiotic binaries emit hard X-ray spectra (see e.g. Muerstet et al. 1997; Kennea et al. 2009), the absence of M giant signature in the optical spectrum and the low equivalent width of the emission lines seem to exclude this hypothesis. A possibility would be that of a transient low-mass X-ray binary in the quiescent state. Alternatively, XGPS-25 could be an X-ray bright LMXRB whose X-ray emission is mostly shielded by an accretion disc seen at high inclination, such as for the accretion disc coronae (ADC) sources 4U 1822-37 and 4U 2129+47 (White & Holt 1982). ADC sources exhibit a wide range of optical and X-ray properties. In the case of 4U 2129+47 for instance, a type I X-ray burst suggests that only 0.2% of the central X-ray luminosity is observed (Garcia & Grindlay 1987). The amount of visible scattered X-ray emission will depend both on the optical depth and extent of the ADC and on the inclination of the accretion disc which determines the fraction of the ADC shielded by its edge (White & Holt 1982). In this framework, the modest L_{X} emitted by XGPS-25 may indicate a low central X-ray luminosity and/or a small visible scattered fraction. The LMXRB scenario is also supported by the relatively small EW of the optical lines which appear comparable to those exhibited by many LMXBs (see e.g. Motch & Pakull 1989).

5.5. Notes on other unidentified XGPS sources

In this section, we report on the 7 unidentified sources for which we could obtain significant spectroscopic information, useful for further optical identification work, and from which constraints on the possible nature of the X-ray emitter can be derived. The remaining six unidentified sources either have too faint optical candidates, offset XGPS positions with respect to 2XMM coordinates or very large error circles leading to an impracticable number of possible candidates.

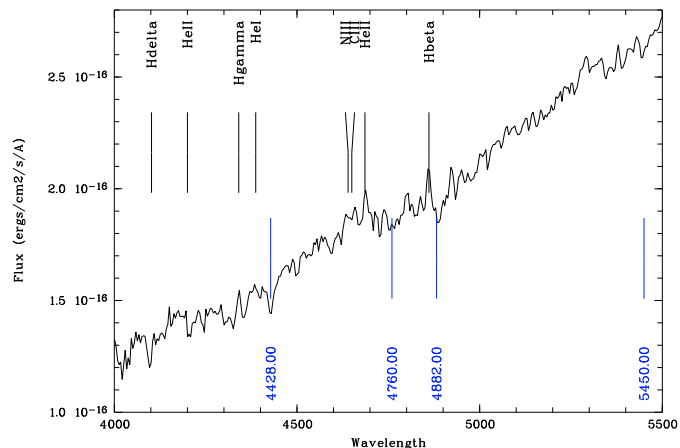


Fig. 24. Blue part of the optical spectrum of the counterpart of XGPS-25 showing the pronounced interstellar absorption lines (marked at the bottom) and the HeII and CIII-NIII Bowen emission lines.

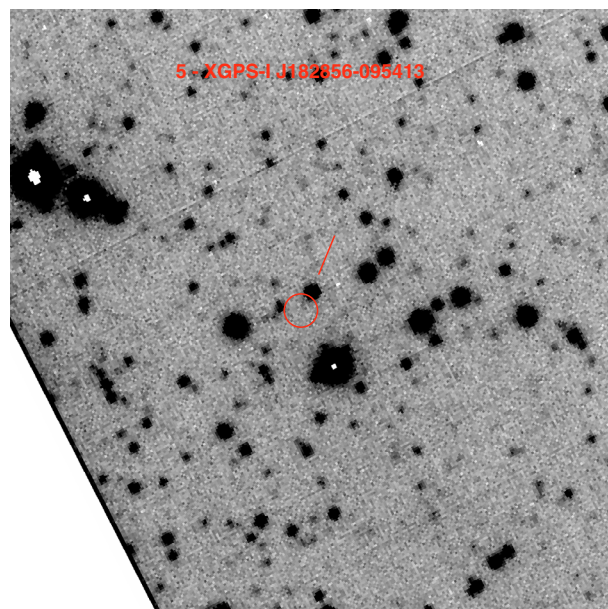


Fig. 25. A 20 s ESO-VLT white band exposure showing the 2XMM position of source XGPS-5. North is at the top and East to the left. The field of view shown is approximately $1' \times 1'$.

5.5.1. XGPS-5

This source has MOS and EPIC pn hardness ratios consistent with an extragalactic origin. The only bright star visible close to the 2XMM error circle (marked on Fig. 25) displays the Mgb band, $H\alpha$ absorption and weak high order Paschen lines. The overall spectrum is consistent with a late G star undergoing a mild reddening of $E(B-V) \sim 1.5$ and therefore is unlikely to be the optical counterpart of the hard X-ray source.

5.5.2. XGPS-7

The $R \sim 18.8$ star USNO-B1.0 0782-0453438 lies slightly outside of the $2.3''$ 90% confidence error circle (see optical finding chart in Fig. 33). The identification probability is less than 2%, based on positional coincidence. USNO-B1.0 0782-0453438 displays $H\alpha$ in absorption and evidence for high-order Paschen lines in absorption. There is a GLIMPSE source

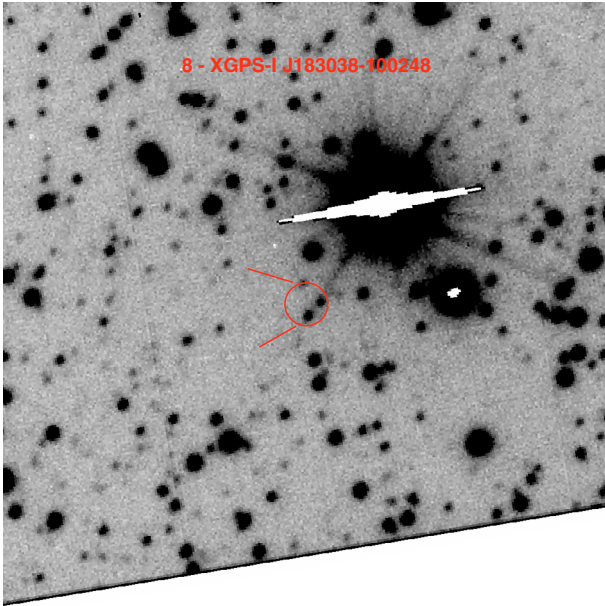


Fig. 26. A 20 s ESO-VLT white band exposure showing the 2XMM position of source XGPS-8. North is at the top and East to the left. The field of view shown is approximately $1' \times 1'$.

G019.5207+00.3343 only $1.2''$ away from the X-ray position and probably coincident with a faint optical object exhibiting a reddened featureless spectrum. The overall SED can be fitted equally well by an O9V or a F6V star undergoing a high reddening of $E(B - V) \sim 5$ and ~ 4 respectively.

5.5.3. XGPS-8

This source remains unidentified down to very faint optical limits. XGPS-8 is probably identical to the ASCA source AX J1830.6-1002 (Sugizaki et al. 2001) located only $18.6''$ away from the XMM position. XGPS-8 is also probably detected by the SPI instrument on board INTEGRAL (Bouchet et al. 2008) up to 100 keV and by IBIS/ISGRI up to 40 keV (Bird et al. 2007), although the identification of the SPI detection with the ASCA source is quoted as tentative since more than one possible identification could exist. Interestingly XGPS-8 also coincides with a radio source, GPSR5 21.631-0.007, detected in the 5 GHz VLA survey of the Galactic plane conducted by Becker et al. (1994). This source is also present in the NVSS catalogue. The XMM EPIC spectrum is not consistent with that of an extragalactic object since it displays a significant flux down to 0.5 keV and seems to consist of two distinct components peaking at ~ 1 keV and 5 keV. Three faint stars are visible in the 90% confidence XMM error circle (see Fig. 26). We have collected spectra of the brightest object located at the south of the error circle and of the faint one to the north both marked on Fig. 26. The two spectra are rather noisy and none of these two candidates displays any convincing evidence for Balmer or Paschen emission or absorption lines. The third object located at the west of the error circle is probably coincident with 2MASS 18303813-1002463, DENIS J183038.2-100246 and the GLIMPSE source G021.6316-00.0061. The probability of identification of XGPS-8 with the 2MASS source is $\sim 40\%$. The 1.2μ to 4.5μ SED does not allow us to meaningfully constrain the spectral type, but suggests a reddening of the order of $E(B - V) \sim 4$, which might not be consistent with the presence of a soft component in the X-ray spectrum.

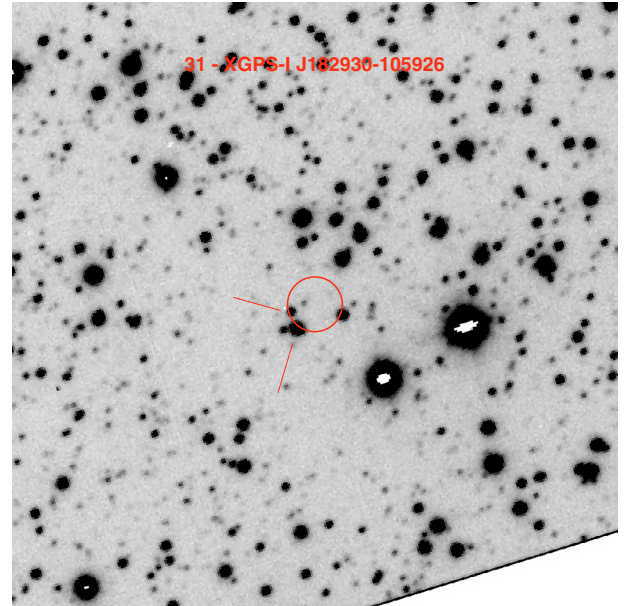


Fig. 27. A 20 s ESO-VLT white band exposure showing the 2XMM position of source XGPS-31. North is at the top and East to the left. The field of view shown is approximately $1' \times 1'$.

5.5.4. XGPS-28

This source was detected three times by XMM-Newton (in observations 0051940601, 0104460401 and 0135747001) and could be slightly variable. Its MOS hardness ratio suggests a likely Galactic nature. We observed the relatively faint star at the East edge of the error circle which is probably identified with 2MASS 18282782-1117500 (see optical finding chart in Fig. 33). The spectrum is highly reddened and displays $H\alpha$ and high order Paschen lines in absorption. The error circle contains a relatively bright GLIMPSE source G020.2759-00.1138 with a 3.6μ mag of 11.66 ± 0.07 . The Spitzer source has no obvious 2MASS or optical counterpart.

5.5.5. XGPS-31

XGPS-31 has EPIC pn and MOS hardness ratios suggesting a Galactic origin. Its rather large error circle of $3.0''$ (90% confidence level) overlaps with three relatively bright objects. We obtained optical spectra of the two bright stars located on the Eastern edge of the error circle (marked in Fig. 27) but failed to acquire spectral information on the object located at the Western edge. Neither of these two objects exhibit spectral signatures of X-ray activity such as Balmer emission lines.

5.5.6. XGPS-42

The position of 2XMM J182833.3-102650 coincides with GLIMPSE G021.0390+00.2608, USNO-B1.0 0795-0405657 and 2MASS 18283337-1026505. In spite of the rather large 90% confidence radius of $2.7''$, the individual probabilities of identification of the X-ray source with the USNO-B1.0 and 2MASS entries are 94% and 95% respectively and thus qualify this relatively bright object ($R \sim 16.2$) as a likely candidate (see Fig. 28). The optical spectrum reveals a reddened continuum with $H\alpha$ in absorption and no evidence for Paschen lines. In the pipeline processing used for the 2XMM catalogue production, the *eposcorr* task had failed to correct X-ray

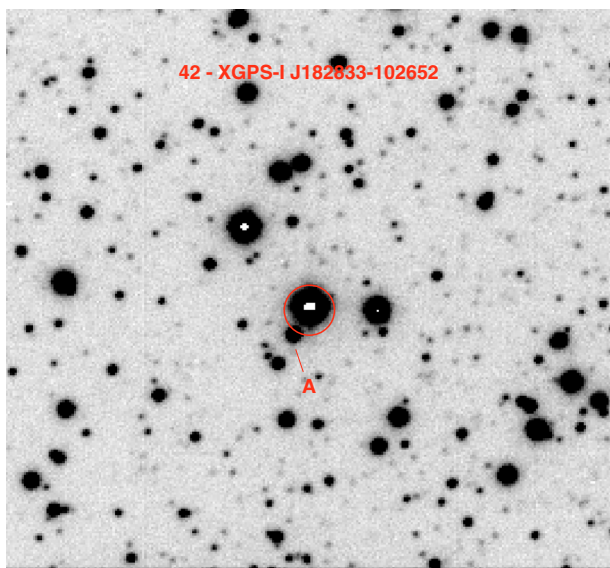


Fig. 28. A 20 s ESO-VLT white band exposure showing the 2XMM position of source XGPS-42. North is at the top and East to the left. The field of view shown is approximately $1' \times 1'$.

positions in observation 0135740901 for remaining boresight errors. However, in the 2002 pipeline processing we actually used at the telescope, the *eposcorr* task had been able to find a likely shift and translation improving the attitude and moved the position of the source towards candidate “A”, the fainter object South-East of USNO-B1.0 0795-0405657 but still located close to the 2XMM 90% confidence circle. Candidate A might be associated with the GLIMPSE source G021.0385+00.2599. Our ESO-VLT optical spectrum of object A reveals again a reddened continuum with $H\alpha$ absorption. However, deep Paschen lines are clearly detected in absorption and hint at an early type star. On this basis, we consider candidate A is a more likely counterpart of XGPS-42 than the brighter USNO-B1.0 star which fails to show spectroscopic evidence of strong coronal activity.

5.5.7. XGPS-69

The relatively bright star ($R \sim 17$), located somewhat outside of the south-west edge of the 90% confidence error circle is USNO-B1.0 0785-0414570 (highlighted in Fig. 33). Its probability to be associated with the X-ray source is of only 22%. Our optical spectrum shows Balmer, Paschen absorption lines and a continuum consistent with a F star reddened by $E(B - V) \sim 1.1$.

5.5.8. Tentative identification of several bright XGPS sources missing in the preliminary catalogue

A small number of relatively bright X-ray sources present in the final catalogue were actually missing in the preliminary XGPS list we used at the time of the observations. These sources would have been bright enough in the broad X-ray band to enter our sample of sources scheduled for optical follow-up. We thus discuss below their possible identifications:

XGPS-I J183216-102303: Ranks as the fourth brightest in the broad (0.4–6.0 keV) band. It is also known as 2XMM J183216.1-102301 and has a bright USNO-B1.0 ($R = 11.80$) and 2MASS ($K = 9.2$) match with a probability of identification of 99% and 91% respectively. XGPS-I J183216-102303 was

also detected by ROSAT as 2RXP J183216.1-102255. The overall picture suggests an identification with a bright active corona. The MOS hardness ratio of 0.51 given in Hands et al. (2004) suggests a hard spectrum possibly indicative of an RS CVn system.

XGPS-I J182830-114516: Ranks at the twelfth position in the broad band. As for the previous case the source has a bright ($R = 12.8$) optical counterpart with a high probability of association (86%). The soft MOS hardness ratio of -0.82 and the EPIC pn hardness ratios of $HR2 = -0.319 \pm 0.067$ and $HR3 = -0.625 \pm 0.096$ clearly indicate an active corona.

XGPS-I J183053-101936: Stands among the faintest of our sample at the 66th position. It is clearly identified with an active corona on the basis of a highly significant match with 2MASS 18305320-1019370 ($K = 9.4$; 95%) and USNO-B1.0 0750-13374636 ($R = 14.4$; 92%) and of a soft MOS hardness ratio of -0.08 .

XGPS-I J183057-103452 (35th), XGPS-I J183156-102447 (60th) have no match with USNO-B1.0 nor 2MASS and no tentative identification in Simbad.

Accordingly, we assigned a stellar nature to the first three sources and include these alongside the 43 objects studied at the telescope when discussing the nature of the XGPS source content.

6. Properties and characteristics of the XGPS source sample

We show in Fig. 29 the distribution of the full sample of XGPS/2XMM sources in an X-ray two-colour diagram based on the hardness ratios deriving from the EPIC pn camera. The XMM-Newton EPIC hardness ratios are based on five energy bands which expressed in keV units are 0.2–0.5, 0.5–1, 1–2, 2–4.5 and 4.5–12.0. Hardness ratio i is then defined as;

$$HR_i = \frac{C_{i+1} - C_i}{C_{i+1} + C_i} \quad (1)$$

with C_i the count rate in band i corrected for vignetting. Soft sources exhibit negative hardness ratios.

The diagram overplots the source nature (active corona, X-ray binary, cataclysmic variable or unidentified) as derived from our optical spectroscopic campaign for a subset of bright sources. Because of the limit of 0.3 set on the hardness ratio errors, only a fraction of the 269 XGPS/2XMM sources appear in the diagrams. In addition, those sources with likely infrared or optical counterparts based on the probability of identification with 2MASS or USNO-B1.0 are highlighted.

As expected, the sources with spectroscopically confirmed stellar identifications occupy the region with $pn_HR3 < 0.0$ indicative of an underlying soft X-ray spectrum, although in some cases with non-negligible soft X-ray absorption (as measured by pn_HR2). It is also remarkable that most of the XGPS entries having a likely identification with a bright USNO-B1.0 or 2MASS candidate (here with a probability of association higher than 90%) are also found in the soft region implying that these are also very likely active coronae. The handful of spectroscopically identified active coronae without high probability USNO-B1.0 or 2MASS associations are faint Me stars. In these cases, the low identification probabilities reflect the high surface density of objects as faint as the M star counterparts.

Interestingly, a few hard X-ray sources also have high probability matches with relatively bright optical or infrared counterparts. At the probability threshold of 90% chosen here, the sample “purity” or integrated probability of identification is about

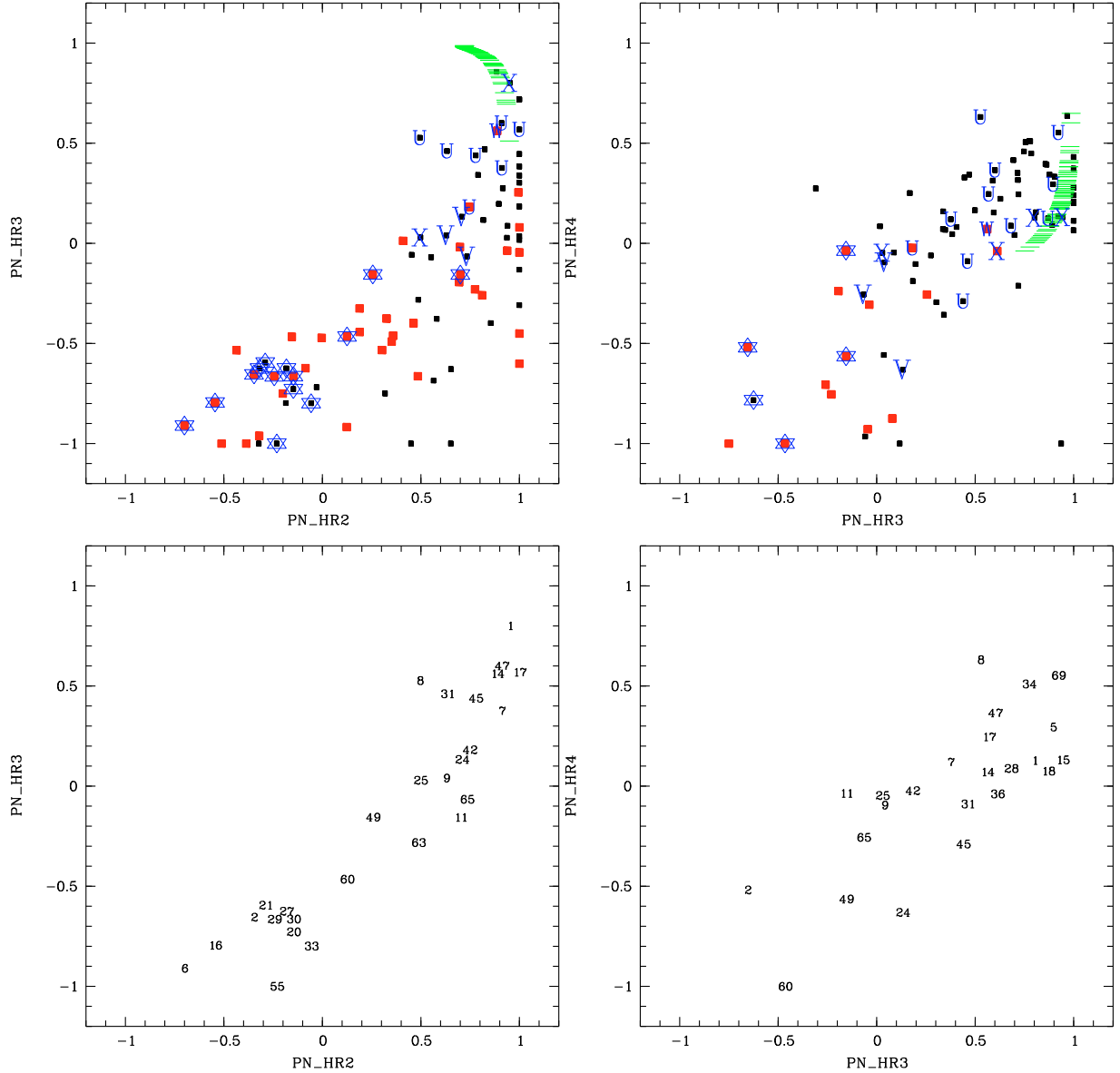


Fig. 29. The distribution of the XGPS/2XMM sources in the EPIC pn hardness ratio diagrams. For clarity, we show only those sources with hardness ratio errors less than 0.3. *Upper panel:* Larger red squares; sources having an optical or infrared counterpart with matching probability above 90%. Small black squares; the remaining XGPS sources. The overplotted characters (in blue) show the sources observed at the telescope. Stars - identified active coronae; V – cataclysmic variables; X – high-mass and low-mass X-ray binary candidates; W – Wolf-Rayet; U – sources unidentified at the telescope. The green strips illustrate the locus occupied by extragalactic sources, computed assuming a power-law spectrum of photon index 1.7 and the total Galactic absorption on the line of sight. *Lower panel:* corresponding id numbers of the XGPS sources observed at the telescope.

99%, leaving only 1% of spurious matches (see Table 2). We note that this probability threshold also implies that we miss about two thirds of all true associations. The total number of XGPS/2XMM sources shown in Fig. 29 matching a USNO-B1.0 or a 2MASS entry and having errors on pn_HR2 and pn_HR3 hardness ratios smaller than 0.3, is of 38. Therefore, at most one of these high likelihood associations could be spurious. Since the probability of a spurious match does not depend on source hardness, the frequency of wrong identifications will be higher for hard X-ray sources which on the average have fainter optical counterparts and are less likely to have a bright stellar counterpart than soft X-ray sources. This is possibly the case of source XGPS-42 (see Sect. 5.5.6) for which the bright USNO-B1.0 counterpart has no spectroscopic evidence suggesting

it is the true counterpart of the X-ray source, whereas the much fainter candidate A exhibits the spectral signatures of an early type star and on this basis can be considered as a serious contender. XGPS-42 (pn_HR2 = 0.74 ± 0.14 ; pn_HR3 = 0.18 ± 0.14 ; pn_HR4 = -0.02 ± 0.14) appears as the hardest unidentified source having a high probability of association with a bright optical object. However, the majority of the associations between a hard X-ray source and a relatively bright optical or infrared object, are still expected to be true identifications in agreement with the fact that the γ -Cas like object XGPS-36 and the Wolf-Rayet associated with XGPS-14 are found amongst them.

The identified or candidate low-mass and high-mass X-ray binaries and cataclysmic variables preferentially exhibit harder X-ray spectra, some approaching that expected for extragalactic

sources. However, CVs in general display spectra significantly softer than those of background AGN. Only one of the two XGPS sources identified with an early type B star (XGPS-56, not plotted on Fig. 29 for clarity) has an EPIC pn measurement. Due to the low count rates in the soft band HR2 is not defined. Its HR3 and HR4 ratios of 0.92 ± 0.11 and 0.14 ± 0.16 respectively clearly indicate a hard source. Although early-type stars have thin thermal spectra of temperature comparable to that of active coronae, their somewhat higher average X-ray luminosity ($L_X \sim 10^{31-32} \text{ erg s}^{-1}$) allow their detection at large distances in spite of the strong hardening due to significant photoelectric interstellar absorption. Source XGPS-14, identified with a likely wind colliding Wolf-Rayet star also appears as a hard X-ray source.

It can also be seen that several of the sources we failed to identify have hardness ratios significantly softer than those expected from a typical AGN absorbed by the full Galactic line-of-sight column density. The nature of these Galactic sources is hard to guess. In the absence of a 2MASS or GLIMPSE infrared source an identification with a massive X-ray binary or a γ -Cas like analogue seems unlikely. Cataclysmic variables would make viable candidates since we know from our identification of the relatively X-ray bright source, XGPS-9 with a $V \sim 23$ object, that CVs may turn out to be hard to identify in the large XMM-Newton error boxes and even beyond the spectroscopic reach of the VLT, at least in the optical band. However, some of these unidentified sources may belong to a new group of moderate- to low-luminosity X-ray sources such as wind-accreting neutron stars (Pfahl et al. 2002) or pre low-mass X-ray binaries (Willems & Kolb 2003). If this putative population has a space density which rises sharply with declining galacto-centric radius, then the X-ray surveys of the Galactic plane carried out prior to XMM-Newton and Chandra may contain very few relatively nearby archetypes of this population.

With an assumed luminosity of the CVs of $L_X \sim 10^{31} \text{ erg s}^{-1}$ and a limiting flux of $F_{\text{lim}} \sim 2 \times 10^{-14} \text{ erg cm}^{-2} \text{ s}^{-1}$, the maximum distance for a CV to be included in our sample, ignoring absorption, is about 2 kpc (absorption with a column density of $N_H = 10^{22} \text{ cm}^{-2}$ only gives a 10% flux reduction in the 2–10 keV band). The volume probed per XMM-pointing is $\sim 1.1 \times 10^5 \text{ pc}^3$. The CV space density is not well known, with recent observational constraints derived from the ROSAT Bright Survey (Schwope et al. 2002) and the ROSAT NEP Survey (Pretorius et al. 2007) for non-magnetic CVs giving $\rho \sim 1.5 \times 10^{-6} \dots 1.1 \times 10^{-5} \text{ pc}^{-3}$. Both values are nevertheless compatible with each other, because the RBS only probes the intrinsically bright part of the parent population, while the NEP also probes the faint end of the luminosity function at $\log(L_X) < 30.5 \text{ erg s}^{-1}$, which currently is very poorly understood¹⁵. In 17 XGPS pointings we might thus expect approximately 3 (RBS-type) $L_X \sim 10^{31} \text{ erg s}^{-1}$ non-magnetic CVs. Our survey area is too small to uncover the likely more abundant low-luminosity CVs at $L_X = 10^{30} \text{ erg s}^{-1}$. In 17 XGPS pointings we are surveying a volume of $6 \times 10^4 \text{ pc}^3$ and we expect to have one at maximum in our sample.

6.1. Log N – Log S curves

We constructed $\log N(>S)$ – $\log S$ curves using the final XGPS source list limited to count rates higher than 0.5 cts/ks and 1.5 cts/ks in the soft and hard bands respectively. This relatively

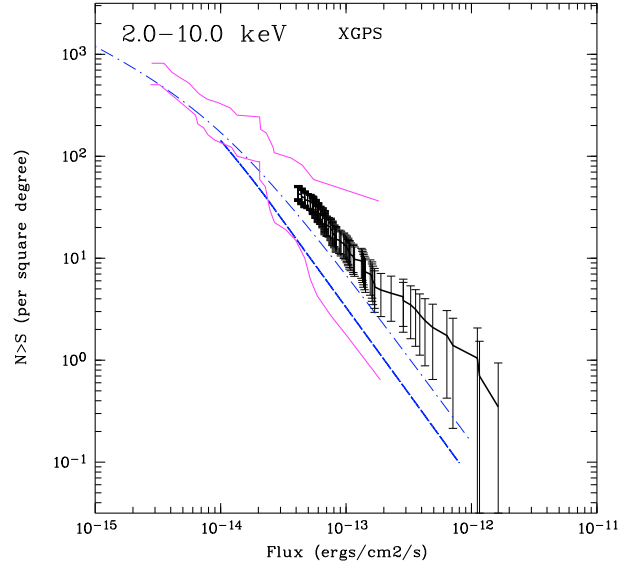


Fig. 30. The $\log N(>S)$ – $\log S$ curve of XGPS sources in the hard band. Error bars represent the one sigma counting statistics. At faint fluxes, the 90% confidence region of the $\log N(>S)$ – $\log S$ curve of Ebisawa et al. (2001) is shown in magenta. The dash-dotted blue curve represents the expected extragalactic contribution assuming a mean N_H of $9.0 \times 10^{22} \text{ cm}^{-2}$. Thin line: after Campana et al. (2001). Thick line: after Mateos et al. (2008).

high threshold minimises the effects of possible uncertainties in the area correction (see Fig. 8 in Hands et al. 2004) while keeping the flux range adapted to our optically identified sample of bright sources. The total number of sources entering the $\log N(>S)$ – $\log S$ curves is of 212 for the soft band and of 129 for the hard band. We apply the count to flux conversion factor of $2.6 \times 10^{-14} \text{ erg cm}^{-2} \text{ s}^{-1} / \text{MOS count ks}^{-1}$ for the hard band spectra given in Hands et al. (2004). This factor roughly corresponds to an “average” spectrum in the context of both Galactic and extragalactic sources ($N_H = 1 \times 10^{22} \text{ cm}^{-2}$ with a power law of photon index 1.7).

Since the stellar component is likely to dominate source counts in the soft band, we assumed a thin thermal spectrum with $kT \sim 0.5 \text{ keV}$ absorbed by $N_H \sim 10^{21} \text{ cm}^{-2}$. These spectral parameters are typical of active stars (Guedel & Naze 2009) observed at distances of a few hundred parsecs. The resulting flux conversion factor is $5.2 \times 10^{-15} \text{ erg cm}^{-2} \text{ s}^{-1} / \text{MOS count ks}^{-1}$ in the 0.4–2 keV band.

As shown in Fig. 15 of Hands et al. (2004), the 2–10 keV $\log N(>S)$ – $\log S$ XGPS curve nicely merges at high fluxes with the ASCA $\log N(>S)$ – $\log S$ (Sugizaki et al. 2001) and at faint fluxes with the results of a deep Chandra observation of a specific field at $l = 28.5^\circ$ (Ebisawa et al. 2001, 2005) (see Fig. 30). We expect a non-negligible contribution from extragalactic sources in this hard band despite the large Galactic foreground absorption. In order to estimate this fraction, we considered both the $\log N(>S)$ – $\log S$ relation of Campana et al. (2001) and that recently obtained by Mateos et al. (2008) (using the three-powerlaw description).

In the region covered by the XGPS, the mean total Galactic column density of $\sim 9 \times 10^{22} \text{ cm}^{-2}$ is high enough to reduce the normalisation of the $\log N(>S)$ – $\log S$ curve for extragalactic sources by a factor of about two. Consequently, in the flux range covered by the XGPS (between 5×10^{-14} and $1 \times 10^{-12} \text{ erg cm}^{-2} \text{ s}^{-1}$; 2–10 keV), the mean number of extragalactic sources per square degree is only 43% of what would be observed at high galactic latitude.

¹⁵ see the discussion by Pretorius in the conference *Wild Stars in the Old West* published on-line only <http://www.noao.edu/meetings/wildstars2/talks/tuesday/pretorius.pdf>

The X-ray bright part of the $\log N(>S)$ – $\log S$ curve of [Campana et al. \(2001\)](#), most relevant for our study, is based on the results of the ASCA GIS medium sensitivity survey of [Della Ceca et al. \(2001\)](#) and [Ueda et al. \(2005\)](#). At low flux, [Campana et al. \(2001\)](#) use data from several deep Chandra surveys. On the other hand, the $\log N(>S)$ – $\log S$ curve of [Mateos et al. \(2008\)](#) is only based on XMM-Newton measurements and being free of relative calibration uncertainties may be more directly comparable to our work.

It can be seen in Fig. 30 that the curve based on ASCA is systematically higher by a factor of 1.2 to 2.0 than that derived from XMM-Newton. This large discrepancy is also exemplified in Fig. 6 of [Mateos et al. \(2008\)](#). According to these authors, the reasons explaining the higher normalisation of the ASCA $\log N(>S)$ – $\log S$ remain unknown, since cross calibration uncertainties are unlikely to account for more than a 10% difference. We may argue, however, that since the curves are based on serendipitous detections in the field of view of observations devoted to bright targets, they are necessarily difficult to correct for in the flux range covered by the targets. Such a bias could explain the difference between the two $\log N(>S)$ – $\log S$ curves and would then argue in favour of using the ASCA relation, since the targets of the ASCA pointings were in general much brighter than those selected for the XMM-Newton observations. Depending on the assumed $\log N(>S)$ – $\log S$ curve, up to 50% (ASCA) or 30% ([Mateos et al. 2008](#)) of the low-latitude source population at $F_X \gtrsim 5 \cdot 10^{-14} \text{ erg cm}^{-2} \text{ s}^{-1}$ could be of extragalactic origin. At this threshold, the fraction of XGPS/2XMM sources with EPIC pn_HR3 and pn_HR4 consistent within 2σ with that expected from an extragalactic source is $\sim 50 \pm 8\%$. Given that this must represent an upper limit on the fraction of extragalactic sources contaminating the sample (since distant galactic sources will have hardness ratios largely indistinguishable from extragalactic objects) it strongly suggests that at least half of the hard sources are indeed of Galactic origin.

At a higher flux of $F_X \sim 10^{-12} \text{ erg cm}^{-2} \text{ s}^{-1}$, the relative contribution of AGNs decreases to $\sim 10\%$ in agreement with results from the ASCA Galactic plane survey ([Sugizaki et al. 2001](#)), albeit with a close to 100% upper limit owing to the high uncertainty caused by small number statistics. The exact contribution of extragalactic and Galactic sources is also made somewhat uncertain by the intrinsic scatter of the count to flux conversion resulting from the variety of photo-electric absorptions and intrinsic spectral shapes.

We investigated how the likely distribution of the intrinsic spectra and photoelectric absorptions of Galactic X-ray sources would affect the hard X-ray $\log N(>S)$ – $\log S$ curves. For that purpose, we computed the distribution of the 2–6 keV count to 2–10 keV flux conversion factors assuming powerlaw indices evenly distributed between 1.3 and 2.1 and $\log(N_H)$ in the range of 21.5 to 22.5. Assuming a constant ISM density and a Galactic radius of 14 kpc, a $\log(N_H)$ of 22.5 is reached at ~ 6.5 kpc. We assumed that this value was representative of the limiting distance of our survey. Our most absorbed source XGPS-3 (and probably most luminous apart from XGPS-1) also exhibits $\log(N_H) \sim 22.5$. This “flat” distribution of spectral parameters yields a rms scatter of 15% on the conversion factor. With the $\log N(>S)$ – $\log S$ slopes found here, the corresponding errors on the integrated surface densities of Galactic sources remain of the same order and become comparable to counting errors for the total Galactic + extragalactic curve near our faint flux limit. The effect should thus be relatively small and in the absence of good knowledge of the true N_H and spectral shapes exhibited by hard Galactic sources one cannot estimate more precisely how

the expected scatter of spectral parameters impacts the Galactic $\log N(>S)$ – $\log S$ curves.

We also tried to estimate the consequences of assuming a common mean count to flux conversion factor for both Galactic and extragalactic sources. For instance, removing the ASCA $\log N(>S)$ – $\log S$ seen through the mean survey N_H of $9 \times 10^{22} \text{ cm}^{-2}$ from the hard MOS count distribution rises the expected number of hard Galactic sources brighter than $1 \times 10^{-13} \text{ erg cm}^{-2} \text{ s}^{-1}$ and $5 \times 10^{-14} \text{ erg cm}^{-2} \text{ s}^{-1}$ to values comparable to those obtained assuming the [Mateos](#) extragalactic $\log N(>S)$ – $\log S$ and the count to flux conversion factor of [Hands et al. \(2004\)](#). However, the size of the effect will also depend on ISM clumpiness and on the intrinsic scatter of the AGN spectral parameters.

In the soft 0.4–2.0 keV band, we have available the ROSAT X-ray extragalactic $\log N(>S)$ – $\log S$ curve reported by [Hasinger et al. \(1998\)](#) and at faint flux levels that in [Campana et al. \(2001\)](#). However, the effect of the integrated Galactic photoelectric absorption is so large in this case that the expected number of AGN detectable at the XGPS flux level is several orders of magnitude below the observed soft $\log N(>S)$ – $\log S$ curve. We thus expect virtually no extragalactic “contamination” in the 0.4–2.0 keV band.

In order to illustrate the relative contributions of the various classes of identified source to the total Galactic population, we plot in Fig. 31 the soft and hard band $\log N(>S)$ – $\log S$ curves corrected for the contribution of AGNs using for the hard band the $\log N(>S)$ – $\log S$ curve of ASCA. We define here as stars all sources with a positive or tentative stellar spectroscopic identification i.e. with classes AC or AC?? in Table 8. We also consider those XGPS sources having an individual probability of identification with a USNO-B1.0 or a 2MASS entry greater than 90% (corresponding to a $\sim 1\%$ level of spurious associations) and 50%. At this later threshold, we expect the sample to be $\sim 80\%$ complete but with 20% of spurious matches in the sample. In other words, although we do not know which sources are actually identified with a USNO-B1.0 or a 2MASS entry, the total number of matches over the whole sample will be approximately correct. We also note that at the flux limit used here, only 85% of the XGPS sources entered in the $\log N(>S)$ – $\log S$ curve have a corresponding entry in the 2XMM catalogue and were thus searched for a possible candidate USNO-B1.0 or 2MASS identification. The true fraction of statistically plus spectroscopically identified sources should thus be slightly higher than shown on Fig. 31 by the dashed lines. The fact that the source density of bright 2.0–10 keV X-ray sources identified by spectroscopic or statistical means appears comparable to that expected for the Galactic population only, suggests that many of the hard XGPS sources discarded from the optical follow-up campaign on the basis of their too faint optical counterparts are indeed of extragalactic nature.

We used the maximum likelihood methods of [Crawford et al. \(1970\)](#) and [Murdoch et al. \(1973\)](#) to constrain the slopes of the “Galactic only” $\log N(>S)$ – $\log S$ curves. The hard X-ray slope appears consistent with Euclidean ($\alpha = -1.46 \pm 0.14$) and is clearly at variance with that obtained from the ASCA Galactic plane survey ($\alpha = -0.79 \pm 0.07$; [Sugizaki et al. 2001](#)) in the flux range of 10^{-10} to $10^{-12} \text{ erg cm}^{-2} \text{ s}^{-1}$. This steepening was also noted in [Hands et al. \(2004\)](#). Such a quasi-Euclidean distribution suggests that the hard sources detected in the XGPS flux regime are relatively homogeneously distributed and do not suffer too much from absorption effects. On the other hand, the soft X-ray $\log N(>S)$ – $\log S$ is found to be less steep with $\alpha = -1.26 \pm 0.10$. This value is consistent with those reported for other shallow

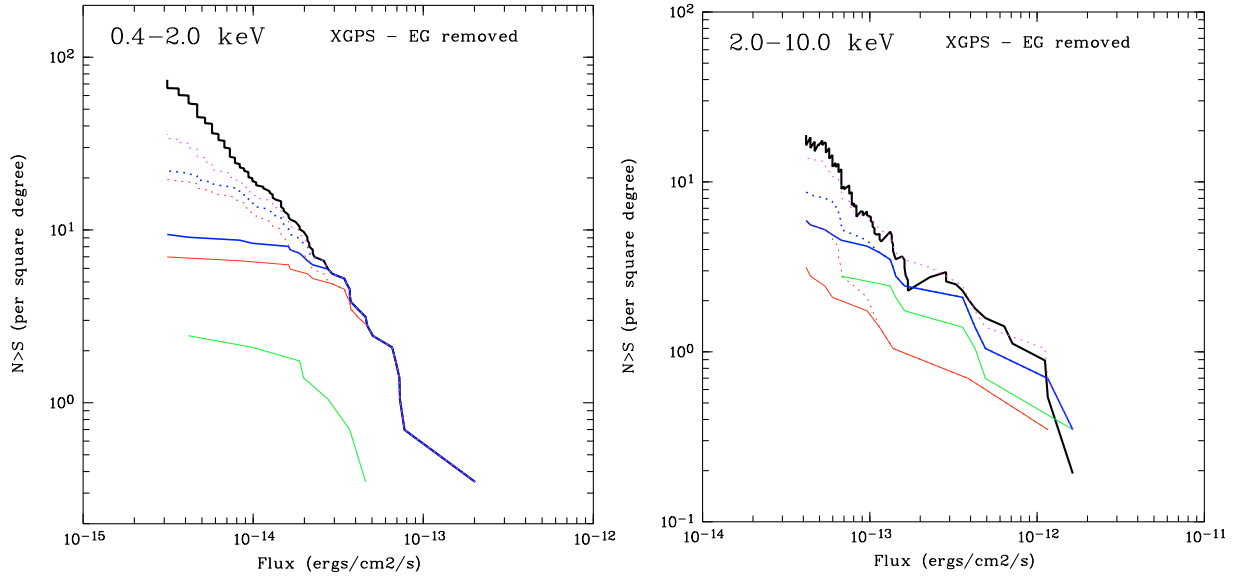


Fig. 31. Soft and hard XGPS $\log N(>S)$ - $\log S$ curves after subtracting the ASCA extragalactic contribution (EG) (thick black lines). The contribution of different categories of source are also shown as follows: identified stars (red, see text); accreting candidates (green); and all identified (blue). The dashed lines show the result of also including matches with USNO-B1.0 and 2MASS which have probabilities higher than 90% to the assumed stellar (red) and total (blue) identifications. The upper magenta dashed line shows the sum of all spectroscopically identified sources added to sources with an individual probability $>50\%$ to be positively associated with a USNO-B1.0 or 2MASS entry.

Table 7. Source identification statistics as a function of flux threshold.

Sample/Flux limit (cgs)	0.4–2.0 keV			
	10^{-13}	3×10^{-14}	10^{-14}	5×10^{-15}
All sources	1	15	52	122
All – extragalactic	1	15	52	122
Active coronae ^a	1	12	17	18
Accreting Candidates	0	2	5	6
All ids	1	15	23	25
All ids + stat ids (90%)	1	15	39	55
All ids + stat ids (50%)	1	15	44	72
Sample/Flux limit (cgs)	2.0–10.0 keV			
	10^{-12}	3×10^{-13}	10^{-13}	5×10^{-14}
All sources	3	10	36	102
All – extragalactic ^b	3	7	17	48
All – extragalactic ^c	3	9	27	73
Active coronae	1	1	2	5
Accreting Candidates	1	4	7	8
All ids	2	6	11	15
All ids + stat ids (90%)	2	6	12	23
All ids + stat ids (50%)	3	7	17	37

Notes. ^(a) The three bright XGPS sources discussed in Sect. 5.5.8 were added to the spectroscopic sample; ^(b) ASCA $\log N(>S)$ - $\log S$; ^(c) $\log N(>S)$ - $\log S$ from Mateos et al. (2008).

or medium deep soft X-ray Galactic surveys ($\alpha = -1.10 \pm 0.26$; Hertz & Grindlay 1984) and ($\alpha = -1.05 \pm 0.13$; Motch et al. 1997).

We list in Table 7 the identification statistics based on spectroscopic work for various classes of source and also positional coincidence with bright USNO-B1.0 and 2MASS entries. The table also gives estimates of the true number of Galactic sources by removing the expected extragalactic contribution using the extragalactic $\log N(>S)$ - $\log S$ curves. In this table, the two

tentative stellar identifications (XGPS-34 and XGPS-63) are included in the group of active coronae.

In the soft band, we spectroscopically identify all sources down to a flux of $2.7 \times 10^{-14} \text{ erg cm}^{-2} \text{ s}^{-1}$ with $\sim 17\%$ representing XRBs candidates and CVs. Adding USNO-B1.0 and 2MASS 90% probability matches allows us to build a completely identified sample down to $2.3 \times 10^{-14} \text{ erg cm}^{-2} \text{ s}^{-1}$. At $F_X = 1 \times 10^{-14} \text{ erg cm}^{-2} \text{ s}^{-1}$, the fraction of sources identified by spectroscopic or statistical means is still high, of the order of $\sim 75\%$. At this flux, XRB candidates and CVs contribute only $\sim 10\%$ of the total number of sources.

The census of optical identifications in the hard X-ray band remains good down to a flux level of $\sim 1 \times 10^{-13} \text{ erg cm}^{-2} \text{ s}^{-1}$ at which we identify one third of the total number of sources and $\sim 70\%$ of the expected number of Galactic sources (assuming the extragalactic ASCA $\log N(>S)$ - $\log S$). Above $F_X = 2 \times 10^{-13} \text{ erg cm}^{-2} \text{ s}^{-1}$, we identify about half of the total number of sources. The relative fraction of solar-type stars and XRB candidates plus CVs are reversed compared to what is observed in the soft band, with typically 10% of the expected number of non-extragalactic sources being identified with a stellar corona and $\sim 40\%$ with a XRB candidate or a CV at $F_X \geq 1 \times 10^{-13} \text{ erg cm}^{-2} \text{ s}^{-1}$.

7. Discussion and conclusions

We have successfully identified at the telescope many of the brightest X-ray sources detected in the XGPS. In addition, we were able to increase the number of identifications by cross-correlating X-ray positions with the USNO-B1.0 and 2MASS catalogues thanks to a carefully calibrated statistical method. The bulk of these statistical identifications with relatively bright optical or near infrared objects are likely stellar coronae based on their soft X-ray spectra. However, our optical campaign has demonstrated that some of them, in particular those exhibiting the hardest X-ray energy distributions, might

Table 8. Optical identifications of the brightest XGPS sources.

XGPS id	XGPS-I name	XGPS RA	XGPS Dec	2XMM name	2XMM RA	2XMM Dec	RA	Dec	r_{90} arcsec	d_{x-o} arcsec	MOS cnts cts/ksec	HR (MOS)	Class	R Type	Optical Id
1	XGPS-I J182833-103659	18 28 33.96	-10 36 59.5	2XMM J182833.7-103700	18 28 33.72	-10 37 00.5	18 28 45.48	-11 17 10.7	2.16	0.50	427.00	0.91	LMXB		
2	XGPS-I J182845-111711	18 28 45.94	-11 17 11.0	2XMM J182845.5-111710	18 28 45.51	-11 17 10.3	18 28 08.94	-09 39 06.0	1.32	2.45	78.50	-0.86	AC	11.71 M1e	GSC2 S3003020461
3	XGPS-I J183208-093906	18 32 08.93	-09 39 06.2	2XMM J183208.7-093905	18 32 08.78	-09 39 05.4	18 32 08.94	-09 39 06.0	2.33		68.80	0.79	HMXB?	16.80 Be?	GSC2 S30030224761
5	XGPS-I J182856-095413	18 28 56.04	-09 54 13.5	2XMM J182855.9-095414	18 28 55.96	-09 54 14.1			1.73		44.60	0.86	UNID		
6	XGPS-I J182847-101334	18 28 47.76	-10 13 34.6	2XMM J182847.6-101337	18 28 47.69	-10 13 37.8	18 28 47.71	-10 13 35.5	1.76	2.32	39.70	-0.97	AC	8.60 G0V	HD 170248
7	XGPS-I J182524-114525	18 25 24.48	-11 45 25.1	2XMM J182524.5-114525	18 25 24.58	-11 45 25.2			2.26		31.50	0.67	UNID		
8	XGPS-I J183038-100248	18 30 38.11	-10 02 48.6	2XMM J183038.2-100246	18 30 38.24	-10 02 46.5			2.29		26.70	0.68	UNID		
9	XGPS-I J183251-100106	18 32 51.65	-10 01 06.7	2XMM J183251.4-100106	18 32 51.48	-10 01 06.0	18 32 51.58	-10 01 05.4	2.34	1.55	25.20	0.27	CV	21.57 A	A
10	XGPS-I J182745-120606	18 27 45.55	-12 06 06.8				18 27 45.40	-12 06 06.6	4.00	2.20	24.10	0.56	HMXB?	21.60 Be	A
11	XGPS-I J182506-120433	18 25 06.85	-12 04 33.6	2XMM J182506.7-120430	18 25 06.73	-12 04 30.3	18 25 06.87	-12 04 29.6	2.63	2.14	17.60	0.15	AC	13.43 K0	GSC2 S300111014094
13	XGPS-I J182757-120941	18 27 57.24	-12 09 41.6				18 27 58.03	-12 09 40.6	4.00	11.60	16.10	-0.72	AC	9.40 G5	TYC 5698-611-1
14	XGPS-I J183116-100921	18 31 16.51	-10 09 21.2	2XMM J183116.5-100926	18 31 16.55	-10 09 26.3	18 31 16.51	-10 09 24.3	2.04	2.03	14.90	0.69	WR	13.34 W/N8	USNO-A2.0.0750-13397443
15	XGPS-I J182814-103728	18 28 14.23	-10 37 28.9	2XMM J182814.2-103726	18 28 14.22	-10 37 26.8	18 28 14.30	-10 37 28.8	3.07	2.31	14.40	0.86	HMXB?	20.30	2MASS J18281430-1037288
16	XGPS-I J183035-102105	18 30 35.91	-10 21 05.9	2XMM J183035.7-102102	18 30 35.71	-10 21 02.8	18 30 35.85	-10 21 04.4	2.22	2.67	14.20	-0.92	AC	13.31 M4e/M5	GSC2 S300302320885
17	XGPS-I J182625-112854	18 26 25.73	-11 28 54.0	2XMM J182626.7-112854	18 26 26.74	-11 28 54.3			2.31		13.80	0.81	UNID		
18	XGPS-I J182756-110450	18 27 56.84	-11 04 50.9	2XMM J182756.7-110448	18 27 56.80	-11 04 48.1			2.32		11.30	0.91	UNID		
19	XGPS-I J182951-100441	18 29 51.57	-10 04 41.0				18 29 51.77	-10 04 45.9	4.00	5.70	10.90	-1.00	B	15.40 ~B	USNO-A2.0.0750-13320307
20	XGPS-I J182639-114216	18 26 39.76	-11 42 16.4	2XMM J182639.6-114216	18 26 39.69	-11 42 16.1	18 26 39.56	-11 42 14.9	2.44	2.28	10.60	-0.78	AC	13.74 M2e	GSC2 S300111036891
21	XGPS-I J183103-095813	18 31 03.69	-09 58 13.5	2XMM J183103.7-095813	18 31 03.73	-09 58 13.6	18 31 03.73	-09 58 17.7	3.02	4.07	10.20	-0.47	AC	16.92 M6e	GSC2 S3003022700
22	XGPS-I J183031-094030	18 30 31.99	-09 40 30.5	2XMM J183031.9-094030	18 30 31.92	-09 40 30.8			1.79		10.00	1.00	UNID		
23	XGPS-I J183017-095326	18 30 17.12	-09 53 26.3	2XMM J183017.0-095326	18 30 17.03	-09 53 26.3	18 30 17.01	-09 53 27.0	1.64	0.77	9.40	-0.44	AC	14.84 M2e	GSC2 S30030226319
24	XGPS-I J183113-094924	18 31 13.12	-09 49 24.5	2XMM J183113.0-094922	18 31 13.03	-09 49 22.6	18 31 13.02	-09 49 25.4	2.80	2.80	9.20	0.20	CV	21.60 B	B
25	XGPS-I J182854-112656	18 28 54.86	-11 26 56.1	2XMM J182854.6-112656	18 28 54.68	-11 26 56.2	18 28 54.50	-11 26 56.2	2.75	2.69	8.80	0.18	LMXB?	15.87	USNO-B1.0.0785-0417035
27	XGPS-I J182911-105544	18 29 11.61	-10 55 44.9	2XMM J182911.6-105545	18 29 11.62	-10 55 45.4	18 29 11.46	-10 55 47.1	2.62	2.81	8.50	-0.76	AC	17.84 M5e	GSC2 S30030233935
28	XGPS-I J182827-111751	18 28 27.77	-11 17 51.8	2XMM J182827.5-111749	18 28 27.51	-11 17 50.0			1.81		8.40	0.67	UNID		
29	XGPS-I J182740-102812	18 27 40.40	-10 28 12.4	2XMM J182740.3-113953	18 27 40.37	-11 39 53.7	18 27 40.40	-11 39 52.6	1.47	1.21	7.60	-0.83	AC	17.05 M5e	GSC2 S300111038707
30	XGPS-I J182930-105926	18 29 30.87	-10 59 26.3	2XMM J182930.0-102811	18 29 30.87	-10 28 11.8	18 27 40.08	-10 28 11.8	2.73	1.27	7.40	-0.86	AC	13.65 M1e	GSC2 S300302037679
31	XGPS-I J182628-120922	18 26 28.66	-12 09 22.5	2XMM J182628.3-120926	18 26 28.32	-12 09 26.2	18 26 28.48	-12 09 25.5	3.07	2.47	6.90	-0.86	AC	13.70 K0	GSC2 S300111332915
34	XGPS-I J183236-101144	18 32 36.64	-10 11 44.8	2XMM J183236.3-101146	18 32 36.39	-10 11 46.9	18 32 36.16	-10 11 44.6	2.96	4.15	6.90	0.75	AC?	14.01 K1	GSC2 S300302326629
36	XGPS-I J183015-104538	18 30 15.94	-10 45 38.5	2XMM J183015.8-104538	18 30 15.81	-10 45 38.5	18 30 15.94	-10 45 38.4	2.67	1.94	6.60	0.89	HMXB?	12.74 Be	GSC2 S3003023371
42	XGPS-I J182833-102652	18 28 33.60	-10 26 52.0	2XMM J182833.3-102650	18 28 33.38	-10 26 50.9			2.72		5.90	0.47	UNID		
45	XGPS-I J182746-110255	18 27 46.33	-11 02 55.1	2XMM J182746.1-110250	18 27 46.20	-11 02 50.7			1.89		5.60	0.21	UNID		
46	XGPS-I J183124-104751	18 31 24.77	-10 47 51.5	2XMM J183124.7-104748	18 31 24.70	-10 47 48.2	18 31 24.70	-10 47 46.0	3.05	2.16	5.60	-1.00	AC	B9V	BD-104713B
47	XGPS-I J182553-112713	18 25 53.86	-11 27 13.0	2XMM J182554.7-112711	18 25 54.76	-11 27 11.6			2.52		5.50	0.92	UNID		
49	XGPS-I J182703-113714	18 27 03.66	-11 37 14.1	2XMM J182703.7-113713	18 27 03.75	-11 37 13.5	18 27 03.86	-11 37 13.9	1.98	1.65	5.36	-0.21	AC	15.49 G9	GSC2 S300111041110
55	XGPS-I J182813-103808	18 28 13.84	-10 38 08.7	2XMM J182813.8-103808	18 28 13.84	-10 38 08.1	18 28 13.82	-10 38 10.6	3.53	2.56	5.00	-0.83	AC	15.91 M4e	GSC2 S30030233754
56	XGPS-I J182828-102357	18 28 28.14	-10 23 57.3	2XMM J182827.9-102359	18 28 27.95	-10 23 59.1	18 28 28.13	-10 24 02.2	2.75	4.11	4.90	0.84	B	14.78 B3	GSC2 S300302038718
57	XGPS-I J182938-094900	18 29 38.87	-09 49 00.8	2XMM J182938.8-094857	18 29 38.85	-09 48 57.6			5.71		4.90	-0.15	UNID		
60	XGPS-I J182511-115726	18 25 11.68	-11 57 26.3	2XMM J182511.5-115726	18 25 11.56	-11 57 27.0	18 25 11.56	-11 57 26.2	3.49	0.78	4.80	-0.74	AC	A9	TYC 5698-4833-1
63	XGPS-I J182607-120627	18 26 07.17	-12 06 27.0	2XMM J182606.9-120626	18 26 06.95	-12 06 26.7	18 26 07.18	-12 06 25.2	3.08	3.66	4.70	-0.31	AC?	16.02 A8	GSC2 S300111013026
65	XGPS-I J182614-110549	18 26 14.69	-11 05 49.6	2XMM J182614.4-110548	18 26 14.46	-11 05 48.1	18 26 14.42	-11 05 50.2	2.78	2.14	4.50	0.11	CV	19.41	USNO-B1.0.0789-0404378
69	XGPS-I J182706-112437	18 27 06.40	-11 24 37.4	2XMM J182706.3-112436	18 27 06.30	-11 24 36.4			2.03		4.20	0.93	UNID		

Notes. All coordinates are given in J2000. For each XGPS-id source, we list the corresponding XGPS-I entry in Hands et al. (2004), the matching 2XMM entry and its combined multi-detection coordinates (when available) and the position of the optical identification. The 90% confidence error radius, r_{90} , is that of the 2XMM entry, while a constant value of $4''$ is assumed for XGPS-I only entries (Hands et al. 2004). d_{x-o} is the offset of the proposed optical counterpart from the 2XMM (or XGPS-I) position. MOS count rates refer to the broad (0.4–6.0 keV) band and the hardness ratios are those of the original XGPS processing. In the Class column, AC stands for active coronae. R magnitudes are extracted from the optical catalogue identifications, apart from sources 9, 10, 13, 15 and 24 for which R is estimated from the flux calibrated spectra.

be massive stars exhibiting particularly hard X-ray emission. Our optical spectroscopic follow-up observations have also confirmed the variety of the astrophysical objects contributing to the low to medium X-ray luminosity population of Galactic X-ray sources. We spectroscopically identify a total of 16 solar-type active stars, mostly among the softest X-ray sources with a high fraction of late Me stars. Furthermore, two early B type stars appear as the probable counterparts of some of our bright XGPS sources. We have discovered a total of three new cataclysmic variables with optical magnitudes in the range of ~ 23 – 22 and 0.5 – 10 keV fluxes from 0.7 to 4.7×10^{-13} erg cm $^{-2}$ s $^{-1}$. Four sources can qualify as massive X-ray binary candidates on the basis of hard X-ray emission and of the presence in the error circle of an early type star exhibiting H α emission. The optical counterpart of XGPS-3 is likely to be an hyper-luminous star possibly as bright as η Carinae. We also report the discovery of an X-ray selected Wolf-Rayet star. The brightest source of our sample, XGPS-1 is a known transient Low-Mass X-ray Binary exhibiting a bursting behaviour. The bright optical magnitude and unusual Bowen CIII-NIII emission of XGPS-25 might be the signature of a Low-Lass X-ray Binary in quiescence, although the observational picture could also be consistent with a rare type of CV. The main findings of our work can be summarised as follows:

1. In the 2–10 keV flux range from 10^{-12} to 10^{-13} erg cm $^{-2}$ s $^{-1}$, we positively identify a large fraction of the hard X-ray sources with Galactic objects at a rate consistent with that expected for the Galactic contribution alone. We note, however, that the diversity of the observed X-ray spectra makes the count to flux conversion somewhat uncertain. Moreover, different normalisations of the extragalactic $\log N(>S)$ – $\log S$ curves are proposed in the literature. Taken together, these two issues do not allow a precise estimate to be made of the fraction of Galactic sources. However, based on hardness ratio considerations, we find that about half of the hard XGPS sources are likely Galactic objects, in rough agreement with the number estimated by subtracting the extragalactic ASCA $\log N(>S)$ – $\log S$ curve from the relation obtained using the whole XGPS sample. At the faintest hard X-ray flux considered in our study of $F_X = 5 \times 10^{-14}$ erg cm $^{-2}$ s $^{-1}$, we still identify spectroscopically or statistically between 30% and 50% of the “Galactic fraction” of the hard X-ray sources. Since most of the identifications at the faint flux end rely on coincidence in position with a bright optical or infrared candidate, the nature of this optically bright population remains somewhat uncertain. However, drawing on the spectroscopic identifications of the optically bright X-ray brightest objects, we expect them for the most part to be made of particularly active late type stars and of early type stars.
2. The soft X-ray band is completely dominated by coronally emitting stars with CVs contributing only a small percentage of the identifications. We identify all sources down to $F_X \sim 3 \times 10^{-14}$ erg cm $^{-2}$ s $^{-1}$. With a mean integrated Galactic N_H of $\sim 9 \times 10^{22}$ cm $^{-2}$ the background of extragalactic sources is completely screened out by line-of-sight absorption. Although the small number statistics does not allow us to draw robust conclusions, it seems that a larger number of faint Me stars is present in the XGPS survey than was identified in the ROSAT Galactic plane survey. Such an evolution is in rough agreement with the prediction of X-ray stellar population models.
3. A few relatively bright active coronae do contribute significantly above 2 keV. This probably indicates unusually high temperatures for the hottest of the two thin thermal components generally needed to represent the X-ray spectra of active stars (see a recent review in [Guedel & Naze 2009](#)). The observation of open clusters and field stars of different ages has established clear relations between stellar age, X-ray luminosity and temperature. For instance, the young stars in Orion (age < 1 Myr) require on average $kT_1 \sim 0.8$ keV and $kT_2 \sim 2.9$ keV, while those of the ~ 160 Myr old stars in NGC 2516 have already dropped to $kT_1 \sim 0.5$ keV and $kT_2 \sim 1.7$ keV (see [Sung et al. 2008](#), and references therein). In contrast, the population of X-ray bright stars identified in the high galactic latitude XMM-Newton Bright Serendipitous Survey by [López-Santiago et al. \(2007\)](#) is well characterised by $kT_1 \sim 0.3$ keV and $kT_2 \sim 1.0$ keV, indicating a significantly older age on average. The hard X-ray coronae unveiled in the XGPS are thus likely to be very young stars in agreement with the predictions of X-ray stellar populations models. However, a fraction of these hard X-ray emitting stars may also be active binaries, mainly of the RS CVn type. Close binaries in which rotation and coronal activity is maintained by tidal synchronisation do amount to about one third of the ROSAT/Tycho-2 sample of stars ([Guillout et al. 2009](#)).
4. The hard X-ray source population has a strong component made of early-type stars exhibiting enhanced emission from a hard X-ray component. The physical mechanism responsible for the hard X-ray excess is unclear but could be related to wind collisions in the case of the Wolf-Rayet star counterpart of XGPS-14 and for the likely hyper-luminous star associated with XGPS-3, which shares several similarities with η Carinae. XGPS-36 is another example of an early Be star containing a well developed circumstellar disc and exhibiting thin thermal X-ray emission with typical temperatures of ~ 10 keV, much hotter than usually measured for normal OB stars in which shocks in the high-velocity radiation-pressure driven wind are responsible for the X-ray emission. The origin of the relatively modest X-ray emission ($L_X \sim 10^{32-33}$ erg s $^{-1}$) remains a matter of lively debate. Two distinct mechanisms have been proposed, mainly in the context of γ -Cas, namely accretion on a companion star, most probably a white dwarf, or magnetic interaction between the early-type star and its decretion disc. XGPS-36 is the eighth identified member of the growing class of γ -Cas analogues, and the fourth found so far in XMM-Newton observations of the Galactic plane.

Our optical spectroscopic campaign has successfully unveiled the nature of the Galactic sources in the hard X-ray flux interval between 10^{-12} and 10^{-13} erg cm $^{-2}$ s $^{-1}$. This F_X range corresponds to the faintest flux limit covered by the ASCA Galactic plane survey but still remains between one and two orders of magnitudes above the sensitivity reached by the deepest Chandra pointings. Our identified sample of hard X-ray sources mainly consists of massive stars, possible X-ray binary candidates and CVs with X-ray luminosities in the range of $L_X \sim 10^{32}$ to 10^{34} erg s $^{-1}$ and located within a few kpc from the Sun. At first glance, the nature of the “local” population of hard X-ray sources does not differ from that inferred from infrared follow-up imaging of deep Chandra pointings in the direction of the Galactic centre (see e.g. [Mauerhan et al. 2009](#), and references therein). However, the relative numbers of the various classes might well be quite different. Our work also illustrates the

difficulty of optically identifying sources in this F_X range, especially the cataclysmic variables as well as the importance of having arcsecond positions so as to alleviate the confusion issue.

Acknowledgements. We thank an anonymous referee for useful comments which helped to improve the quality of this paper. We are grateful to O. Herent for carrying out some of the observations presented in this work. This work has been supported in part by the DLR (Deutsches Zentrum für Luft- und Raumfahrt) under grants 50 OX 0201 and 50 OX 0801. I.N. is supported by the Spanish Ministerio de Ciencia e Innovación under grants AYA2008-06166-C03-03 and CSD2006-70. This publication makes use of data products from the Two Micron All Sky Survey, which is a joint project of the University of Massachusetts and the Infrared Processing and Analysis Center/California Institute of Technology, funded by the National Aeronautics and Space Administration and the National Science Foundation. The DENIS project has been partly funded by the SCIENCE and the HCM plans of the European Commission under grants CT920791 and CT940627. It is supported by INSU, MEN and CNRS in France, by the State of Baden-Württemberg in Germany, by DGICYT in Spain, by CNR in Italy, by FFwFBWF in Austria, by FAPESP in Brazil, by OTKA grants F-4239 and F-013990 in Hungary, and by the ESO C&EE grant A-04-046. Jean Claude Renault from IAP was the Project manager. Observations were carried out thanks to the contribution of numerous students and young scientists from all involved institutes, under the supervision of P. Fouqué, survey astronomer resident in Chile. The WHT is operated on the island of La Palma by the Isaac Newton Group in the Spanish Observatorio del Roque de los Muchachos of the Instituto de Astrofísica de Canarias. The observation presented here was taken as part of the ING service programme (proposal SW2005A06). This research has made use of Aladin, of the VizieR catalogue access tool and of Simbad at CDS, Strasbourg, France.

References

- Abbott, D. C., & Conti, P. S. 1987, *ARA&A*, 25, 113
- Anderson, L. D., & Bania, T. M. 2009, *ApJ*, 690, 706
- Barcons, X., Carrera, F. J., Watson, M. G., et al. 2002, *A&A*, 382, 522
- Becker, R. H., White, R. L., Helfand, D. J., & Zoonematkermani, S. 1994, *ApJS*, 91, 347
- Benjamin, R. A., Churchwell, E., Babler, B. L., et al. 2003, *PASP*, 115, 953
- Berghoef, T. W., Schmitt, J. H. M. M., Danner, R., & Cassinelli, J. P. 1997, *A&A*, 322, 167
- Bird, A. J., Malizia, A., Bazzano, A., et al. 2007, *ApJS*, 170, 175
- Bonnarel, F., Fernique, P., Bienaymé, O., et al. 2000, *A&AS*, 143, 33
- Bouchet, L., Jourdain, E., Roques, J.-P., et al. 2008, *ApJ*, 679, 1315
- Campana, S., Moretti, A., Lazzati, D., & Tagliaferri, G. 2001, *ApJ*, 560, L19
- Cardelli, J. A., Clayton, G. C., & Mathis, J. S. 1989, *ApJ*, 345, 245
- Carpano, S., Pollock, A. M. T., Wilms, J., Ehle, M., & Schirmer, M. 2007, *A&A*, 461, L9
- Castelli, F., & Kurucz, R. L. 2004, *ArXiv Astrophysics e-prints*
- Chlebowski, T., Seward, F. D., Swank, J., & Szymkowiak, A. 1984, *ApJ*, 281, 665
- Corbet, R. H. D. 1986, *MNRAS*, 220, 1047
- Cornelisse, R., Verbunt, F., in't Zand, J. J. M., et al. 2002, *A&A*, 392, 885
- Crawford, D. F., Jauncey, D. L., & Murdoch, H. S. 1970, *ApJ*, 162, 405
- Cutri, R. M., Skrutskie, M. F., van Dyk, S., et al. 2003, *2MASS All Sky Catalog of point sources*, ed. R. M. Cutri, M. F. Skrutskie, S. van Dyk, et al.
- Dame, T. M., Hartmann, D., & Thaddeus, P. 2001, *ApJ*, 547, 792
- Davidson, K., & Humphreys, R. M. 1997, *ARA&A*, 35, 1
- Della Ceca, R., Braitto, V., Cagnoni, I., & Maccacaro, T. 2001, *Mem. Soc. Astron. Ital.*, 72, 841
- Della Ceca, R., Maccacaro, T., Caccianiga, A., et al. 2004, *A&A*, 428, 383
- Dickey, J. M., & Lockman, F. J. 1990, *ARA&A*, 28, 215
- Drimmel, R., Cabrera-Lavers, A., & López-Corredoira, M. 2003, *A&A*, 409, 205
- Duncan, R. A., & White, S. M. 2003, *MNRAS*, 338, 425
- Ebisawa, K., Maeda, Y., Kaneda, H., & Yamauchi, S. 2001, *Science*, 293, 1633
- Ebisawa, K., Tsujimoto, M., Paizis, A., et al. 2005, *ApJ*, 635, 214
- Forman, W., Jones, C., Cominsky, L., et al. 1978, *ApJS*, 38, 357
- Fremat, Y., Houziaux, L., & Andriillat, Y. 1996, *MNRAS*, 279, 25
- Furusawa, H., Kosugi, G., Akiyama, M., et al. 2008, *ApJS*, 176, 1
- Garcia, M. R., & Grindlay, J. E. 1987, *ApJ*, 313, L59
- Griffith, M. R., Wright, A. E., Burke, B. F., & Ekers, R. D. 1994, *ApJS*, 90, 179
- Grindlay, J. E., Hong, J., Zhao, P., et al. 2005, *ApJ*, 635, 920
- Guedel, M., & Naze, Y. 2009, *A&ARv*, 17, 309
- Guillout, P., Hayward, M., Motch, C., & Robin, A. C. 1996, *A&A*, 316, 89
- Guillout, P., Schmitt, J. H. M. M., Egret, D., et al. 1999, *A&A*, 351, 1003
- Guillout, P., Klutsch, A., Frasca, A., et al. 2009, *A&A*, 504, 829
- Hamann, W.-R., Gräfener, G., & Liermann, A. 2006, *A&A*, 457, 1015
- Hands, A. D. P., Warwick, R. S., Watson, M. G., & Helfand, D. J. 2004, *MNRAS*, 351, 31
- Hasinger, G., Burg, R., Giacconi, R., et al. 1998, *A&A*, 329, 482
- Herbig, G. H. 1975, *ApJ*, 196, 129
- Hertz, P., & Grindlay, J. E. 1984, *ApJ*, 278, 137
- Jacoby, G. H., Hunter, D. A., & Christian, C. A. 1984, *ApJS*, 56, 257
- Jaschek, C., & Jaschek, M. 1987, *The classification of stars* (Cambridge: University Press)
- Kennea, J. A., Mukai, K., Sokolowski, J. L., et al. 2009, *ApJ*, 701, 1992
- King, A. R., & Wijnands, R. 2006, *MNRAS*, 366, L31
- Koenig, X., Grindlay, J. E., van den Berg, M., et al. 2008, *ApJ*, 685, 463
- Koornneef, J. 1983, *A&A*, 128, 84
- Le Borgne, J.-F., Bruzual, G., Pelló, R., et al. 2003, *A&A*, 402, 433
- Lockman, F. J., Pisano, D. J., & Howard, G. J. 1996, *ApJ*, 472, 173
- Lopes de Oliveira, R., Motch, C., Haberl, F., Negueruela, I., & Janot-Pacheco, E. 2006, *A&A*, 454, 265
- López-Santiago, J., Micela, G., Sciortino, S., et al. 2007, *A&A*, 463, 165
- Marshall, D. J., Robin, A. C., Reylé, C., Schultheis, M., & Picaud, S. 2006, *A&A*, 453, 635
- Mateos, S., Warwick, R. S., Carrera, F. J., et al. 2008, *A&A*, 492, 51
- Mauerhan, J. C., Munro, M. P., Morris, M. R., et al. 2009, *ApJ*, 703, 30
- Monet, D., & et al. 1998, *VizieR Online Data Catalog*, 1252, 0
- Monet, D. G., Levine, S. E., Canzian, B., et al. 2003, *AJ*, 125, 984
- Motch, C. 2006, in *The X-ray Universe 2005*, ed. A. Wilson, ESA SP, 604, 383
- Motch, C., & Pakull, M. W. 1989, *A&A*, 214, L1
- Motch, C., Guillout, P., Haberl, F., et al. 1997, *A&A*, 318, 111
- Motch, C., Herent, O., & Guillout, P. 2003, *Astron. Nachr.*, 324, 61
- Motch, C., Lopes de Oliveira, R., Negueruela, I., Haberl, F., & Janot-Pacheco, E. 2007a, in *Active OB-Stars: Laboratories for Stellar and Circumstellar Physics*, ed. A. T. Okazaki, S. P. Owocki, & S. Stefl, ASP Conf. Ser. 361, 117
- Motch, C., Michel, L., & Pineau, F. X. 2007b, in *Astronomical Data Analysis Software and Systems XVI*, ed. R. A. Shaw, F. Hill, & D. J. Bell, ASP Conf. Ser. 376, 699
- Muerst, U., Wolff, B., & Jordan, S. 1997, *A&A*, 319, 201
- Muno, M. P., Baganoff, F. K., Bautz, M. W., et al. 2003, *ApJ*, 589, 225
- Muno, M. P., Bauer, F. E., Baganoff, F. K., et al. 2009, *ApJS*, 181, 110
- Murdoch, H. S., Crawford, D. F., & Jauncey, D. L. 1973, *ApJ*, 183, 1
- Nazé, Y. 2009, *A&A*, 506, 1055
- Neff, J. E., & Simon, T. 2008, *ApJ*, 685, 478
- Negueruela, I. 2007, in *Massive Stars in Interactive Binaries*, ed. N. St.-Louis & A. F. J. Moffat, ASP Conf. Ser. 367, 477
- Oskinova, L. M. 2005, *MNRAS*, 361, 679
- Pallavicini, R., Golub, L., Rosner, R., et al. 1981, *ApJ*, 248, 279
- Patterson, J. 1984, *ApJS*, 54, 443
- Patterson, J. 1994, *PASP*, 106, 209
- Patterson, J., & Raymond, J. C. 1985, *ApJ*, 292, 550
- Pfahl, E., Rappaport, S., & Podsiadlowski, P. 2002, *ApJ*, 571, L37
- Pickles, A. J. 1998, *PASP*, 110, 863
- Pineau, F.-X., Derriere, S., Michel, L., & Motch, C. 2008, in *Astronomical Data Analysis Software and Systems XVII*, ed. R. W. Argyle, P. S. Bunclark, & J. R. Lewis, ASP Conf. Ser. 394, 369
- Pineau, F.-X., Motch, C., Carrera, F., et al. 2010, *A&A*, submitted
- Predehl, P., & Schmitt, J. H. M. M. 1995, *A&A*, 293, 889
- Prestwich, A. H., Kilgard, R., Crowther, P. A., et al. 2007, *ApJ*, 669, L21
- Pretorius, M. L., Knigge, C., O'Donoghue, D., et al. 2007, *MNRAS*, 382, 1279
- Ramsay, G., & Cropper, M. 2004, *MNRAS*, 347, 497
- Ramsay, G., Rosen, S., Hakala, P., & Barclay, T. 2009, *MNRAS*, 395, 416
- Revnivtsev, M., Sazonov, S., Churazov, E., et al. 2009, *Nature*, 458, 1142
- Robrade, J., & Schmitt, J. H. M. M. 2009, *A&A*, 496, 229
- Sakano, M., Warwick, R. S., Decourchelle, A., & Wang, Q. D. 2005, *MNRAS*, 357, 1211
- Schachter, J., Filippenko, A. V., Kahn, S. M., & Paerels, F. B. S. 1991, *ApJ*, 373, 633
- Schlegel, D. J., Finkbeiner, D. P., & Davis, M. 1998, *ApJ*, 500, 525
- Schwarz, R., Schwöpe, A. D., Vogel, J., et al. 2009, *A&A*, 496, 833
- Schwöpe, A. D., Brunner, H., Buckley, D., et al. 2002, *A&A*, 396, 895
- Shara, M. M., Moffat, A. F. J., Gerke, J., et al. 2009, *AJ*, 138, 402
- Skinner, S. L., Zhekov, S. A., Güdel, M., & Schmutz, W. 2007, *MNRAS*, 378, 1491
- Smith, L. F., Shara, M. M., & Moffat, A. F. J. 1996, *MNRAS*, 281, 163
- Staupe, A., Schwöpe, A. D., Schwarz, R., et al. 2008, *A&A*, 486, 899
- Stephenson, C. B. 1992, *AJ*, 103, 263
- Sugizaki, M., Mitsuda, K., Kaneda, H., et al. 2001, *ApJS*, 134, 77
- Sung, H., Bessell, M. S., & Sana, H. 2008, *J. Korean Astron. Soc.*, 41, 1
- Turnshek, D. E. 1985, *An Atlas of digital spectra of cool stars* (Tucson, Ariz. : Western Research Co.), 85

- Tylenda, R. 1981, *Acta Astron.*, 31, 127
Ueda, Y., Ishisaki, Y., Takahashi, T., Makishima, K., & Ohashi, T. 2005, *ApJS*, 161, 185
Vaiana, G. S., Cassinelli, J. P., Fabbiano, G., et al. 1981, *ApJ*, 245, 163
Vogel, J., Byckling, K., Schwobe, A., et al. 2008, *A&A*, 485, 787
Vreux, J. M., Dennefeld, M., & Andrillat, Y. 1983, *A&AS*, 54, 437
Walter, R., Zurita Heras, J., Bassani, L., et al. 2006, *A&A*, 453, 133
Wang, Q. D., Gotthelf, E. V., & Lang, C. C. 2002, *Nature*, 415, 148
Warner, B. 1987, *MNRAS*, 227, 23
Watson, M. G., Schröder, A. C., Fyfe, D., et al. 2009, *A&A*, 493, 339
White, N. E., & Holt, S. S. 1982, *ApJ*, 257, 318
Wijnands, R., in't Zand, J. J. M., Rupen, M., et al. 2006, *A&A*, 449, 1117
Willems, B., & Kolb, U. 2003, *MNRAS*, 343, 949
Williams, R. E., & Ferguson, D. H. 1983, in *Astrophysics and Space Science Library*, IAU Colloq. 72, *Cataclysmic Variables and Related Objects*, ed. M. Livio, & G. Shaviv, 97
Zhao, P., Grindlay, J., Edmonds, P., et al. 2003, *Astron. Nachr.*, 324, 176
Zoonematkermani, S., Helfand, D. J., Becker, R. H., White, R. L., & Perley, R. A. 1990, *ApJS*, 74, 181

Table 9. Additional cross-identifications of optically identified XGPS sources.

XGPS id	XGPS-I name	Identifications
1	XGPS-I J182833-103659	SAX J1828.5-1037
2	XGPS-I J182845-111711	AX J182846-1116
3	XGPS-I J183208-093906	AX J1832.1-0938, DENISJ183208.4-093905, 2MASS 18320893-0939058, IRAS 18293-094, NVSS 183209-093907, GPSR 22.154-0.154
14	XGPS-I J183116-100921	AX J183116-1008, DENIS J183116.5-100924, 2MASS 18311653-1009250, SSTGLMA G021.6064-00.1970
15	XGPS-I J182814-103728	SSTGLMA G020.8457+00.2476
25	XGPS-I J182854-112656	GSC2 S300111083138, DENIS J182854.6-112655, 2MASS 18285460-11265612
36	XGPS-I J183015-104538	USNO-A2.0 0750-13340834, 2MASS 18301593-1045384, SSTGLMA G020.9564-00.2565

Table 10. Summary of X-ray spectral fits. N_{H} are in units of 10^{22} cm^{-2} .

XGPS id	EPIC Cameras	Nbr of source photons	Model	Fit Quality	Fits results
3	MOS1&2	569	phabs*powerl	C=37.8/40 d.o.f.	$N_{\text{H}}=2.69^{+0.76}_{-0.67}$; $\Gamma=1.45^{+0.42}_{-0.40}$
3	MOS1&2	569	phabs*mekal	C=53.7/41 d.o.f.	$N_{\text{H}}=3.8$ (fixed); $kT = 4.2 \pm 0.6 \text{ keV}$
9	pn	177	tbabs*mekal ($kT = 20 \text{ keV}$ fixed)	$\chi^2=13.3/11$ d.o.f.	$N_{\text{H}} \sim 0.8$
14	pn + MOS1&2	362	phabs*mekal	C=67.8/57 d.o.f.	$N_{\text{H}}=5.21^{+1.38}_{-1.25}$; $kT = 2.14^{+1.09}_{-0.52} \text{ keV}$
14	pn + MOS1&2	362	phabs*powerl	C=86.5/57 d.o.f.	$N_{\text{H}}=5.34^{+1.99}_{-1.68}$; $\Gamma=2.91^{+0.96}_{-0.86}$
15	pn + MOS1&2	279	phabs*powerl	C=31.8/28 d.o.f.	$N_{\text{H}}=7.8^{+5.9}_{-3.4}$; $\Gamma=2.4^{+1.5}_{-1.0}$
24	pn	54	tbabs*mekal ($kT = 5 \text{ keV}$ fixed)	N/A	$N_{\text{H}} = 0.2-2.4$
25	pn + MOS1&2	110	phabs*mekal	C=21.6/31 d.o.f.	$N_{\text{H}}=0.48^{+0.31}_{-0.17}$; $kT > 10 \text{ keV}$
25	pn + MOS1&2	110	phabs*powerl	C=12.5/12 d.o.f.	$N_{\text{H}}=0.39^{+0.44}_{-0.29}$; $\Gamma=1.07^{+0.32}_{-0.32}$
65	pn	54	tbabs*mekal ($kT = 5 \text{ keV}$ fixed)	N/A	$N_{\text{H}}=0.8-2.4$

Notes. All errors are 90% confidence level.

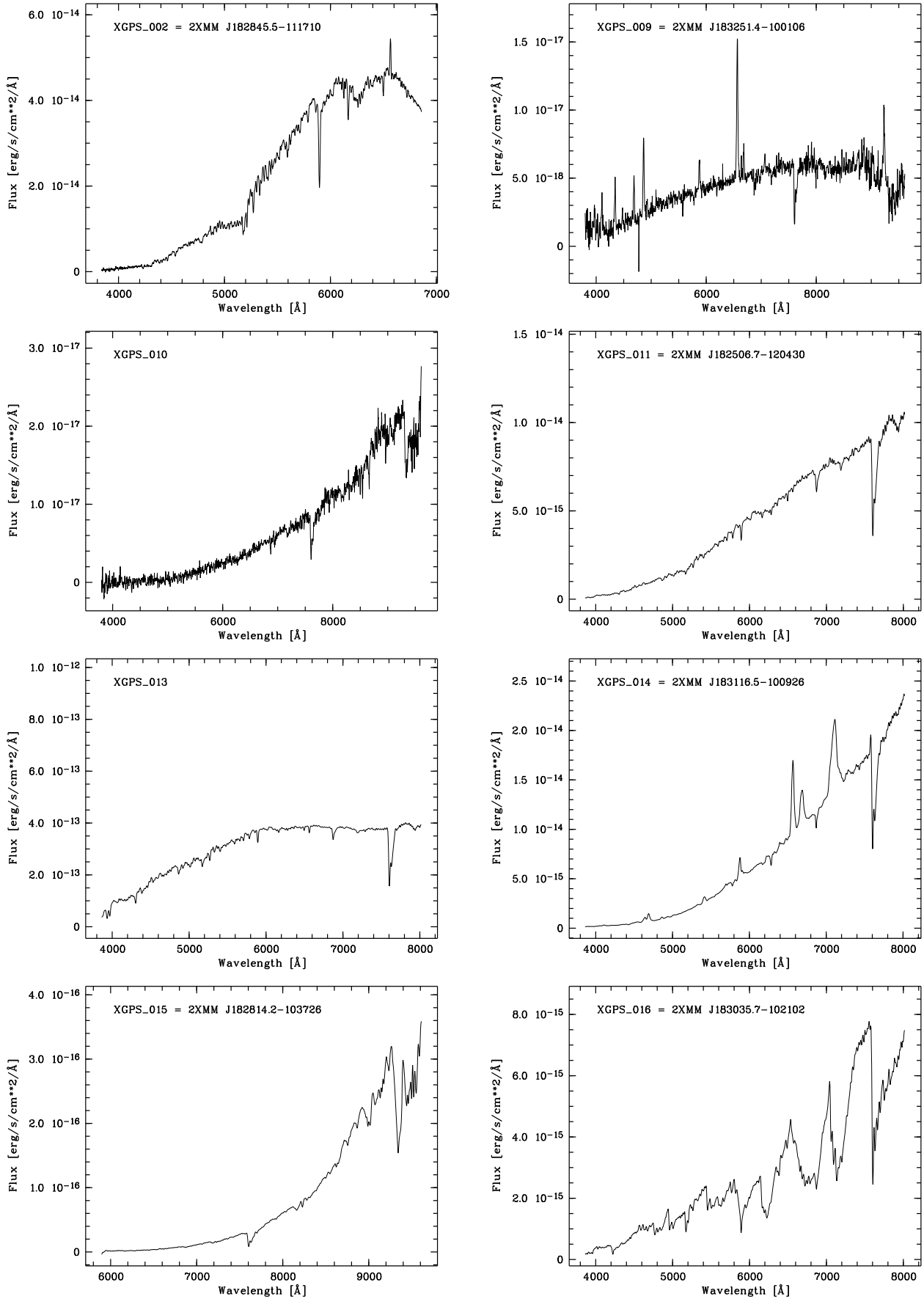


Fig. 32. Optical spectra of candidate counterparts to XGPS sources sorted by increasing id number.

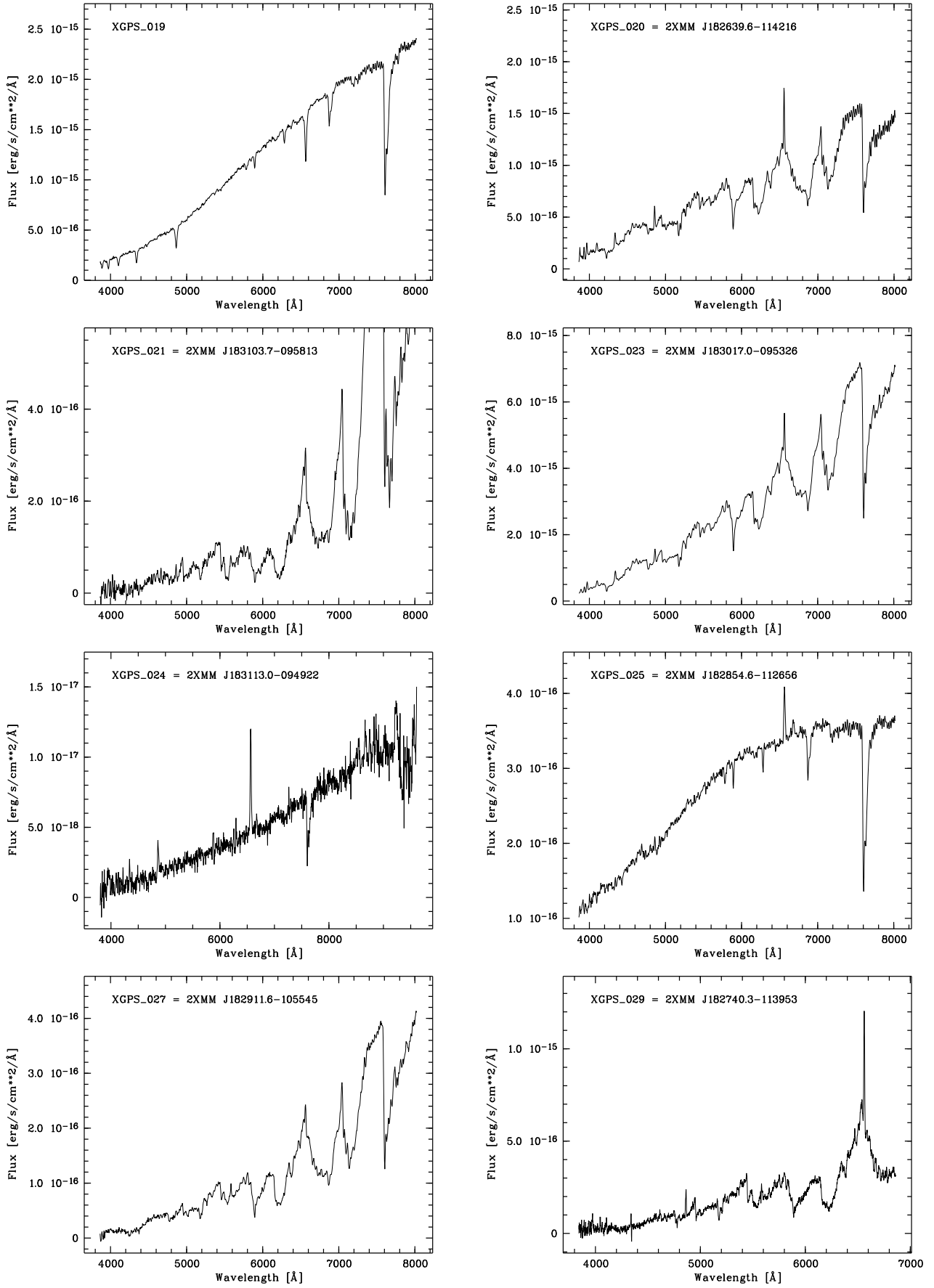


Fig. 32. continued.

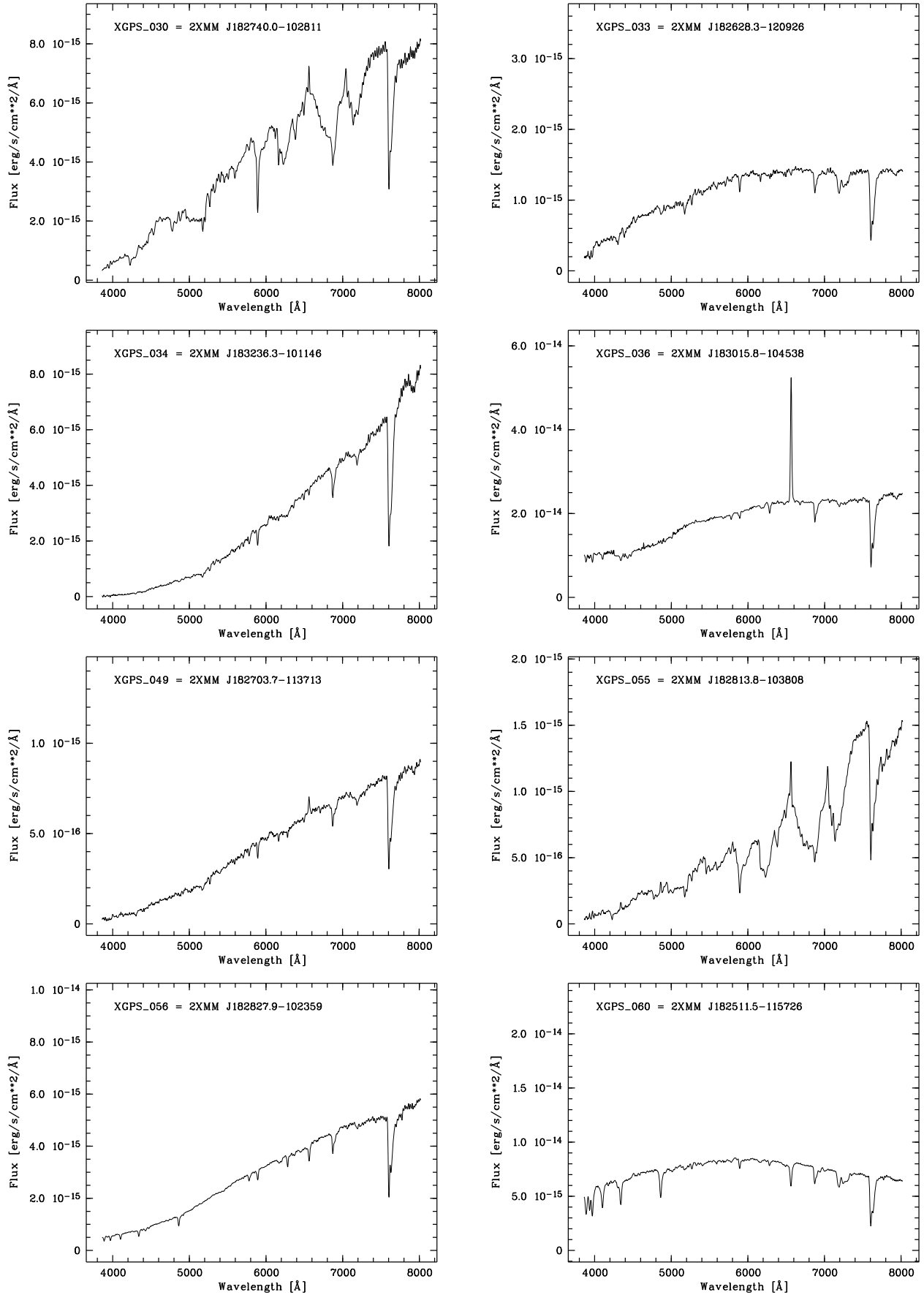


Fig. 32. continued.

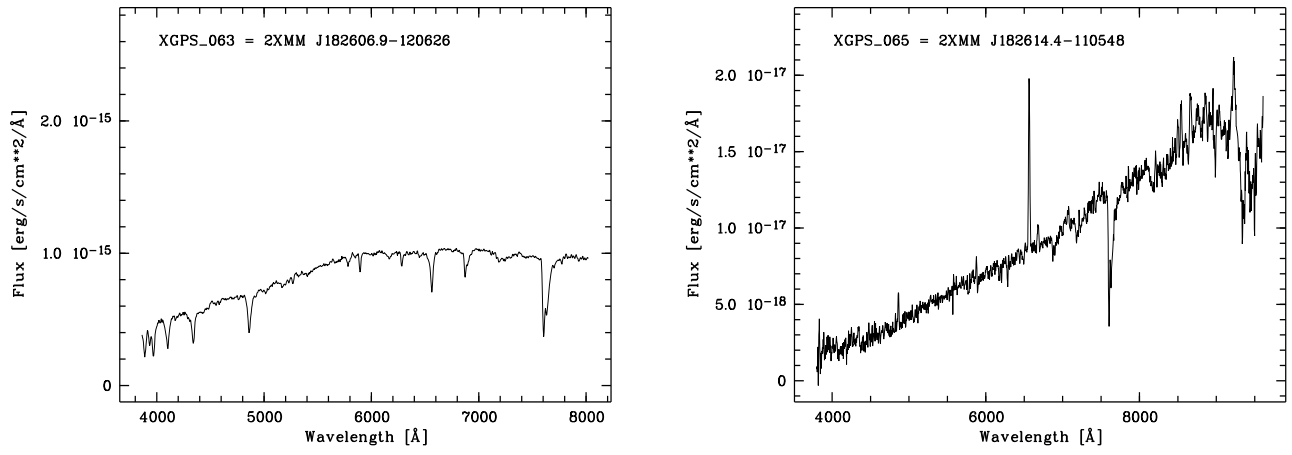


Fig. 32. continued.

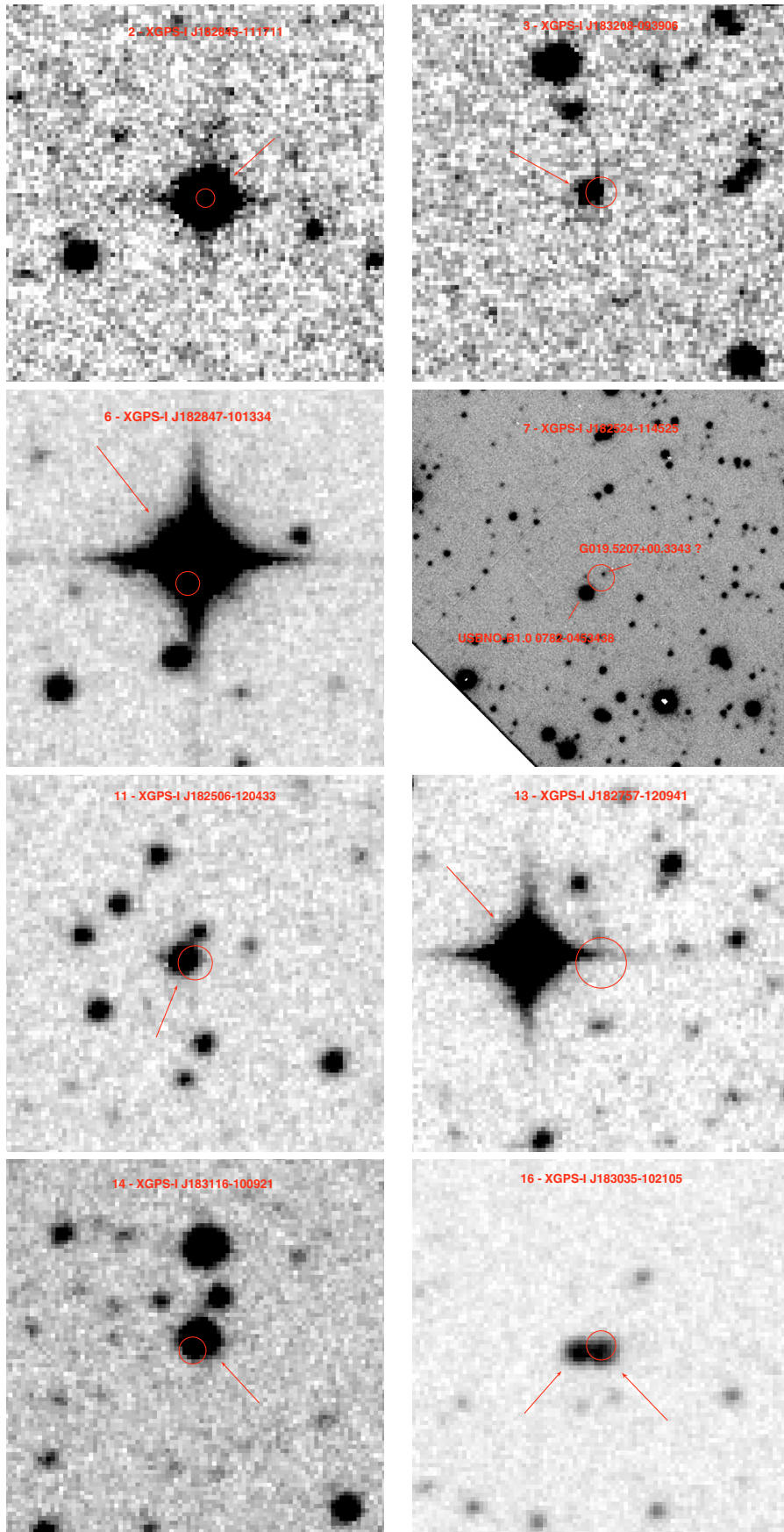


Fig. 33. Finding chart for XGPS sources not shown in the main text, sorted by increasing id number. North is at the top and East to the left. The field of view shown is approximately $1' \times 1'$. Plate origin is listed in Table 11. Proposed counterparts are indicated with an arrow whereas a simple line points to the possible candidates discussed in the main text.

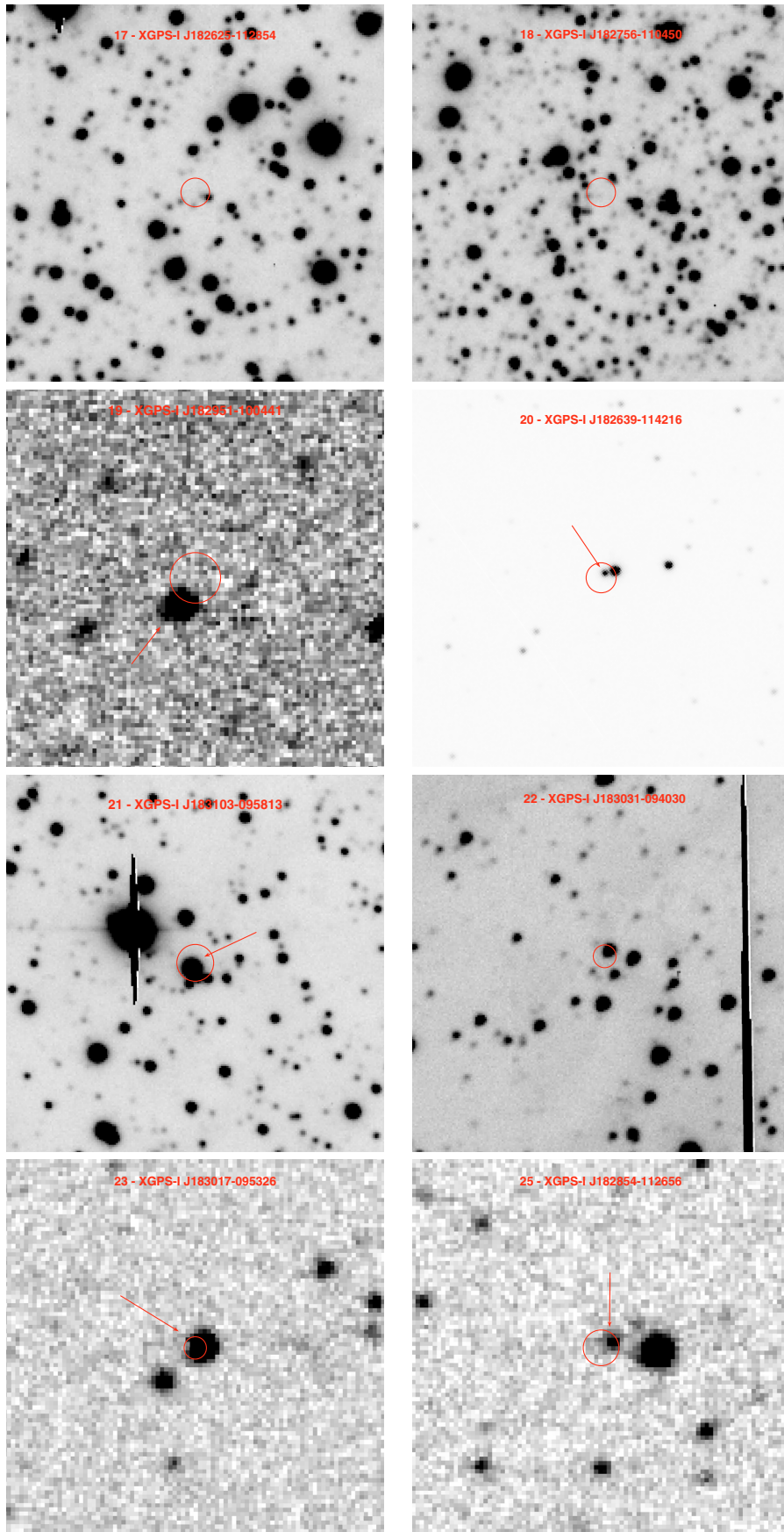


Fig. 33. continued.

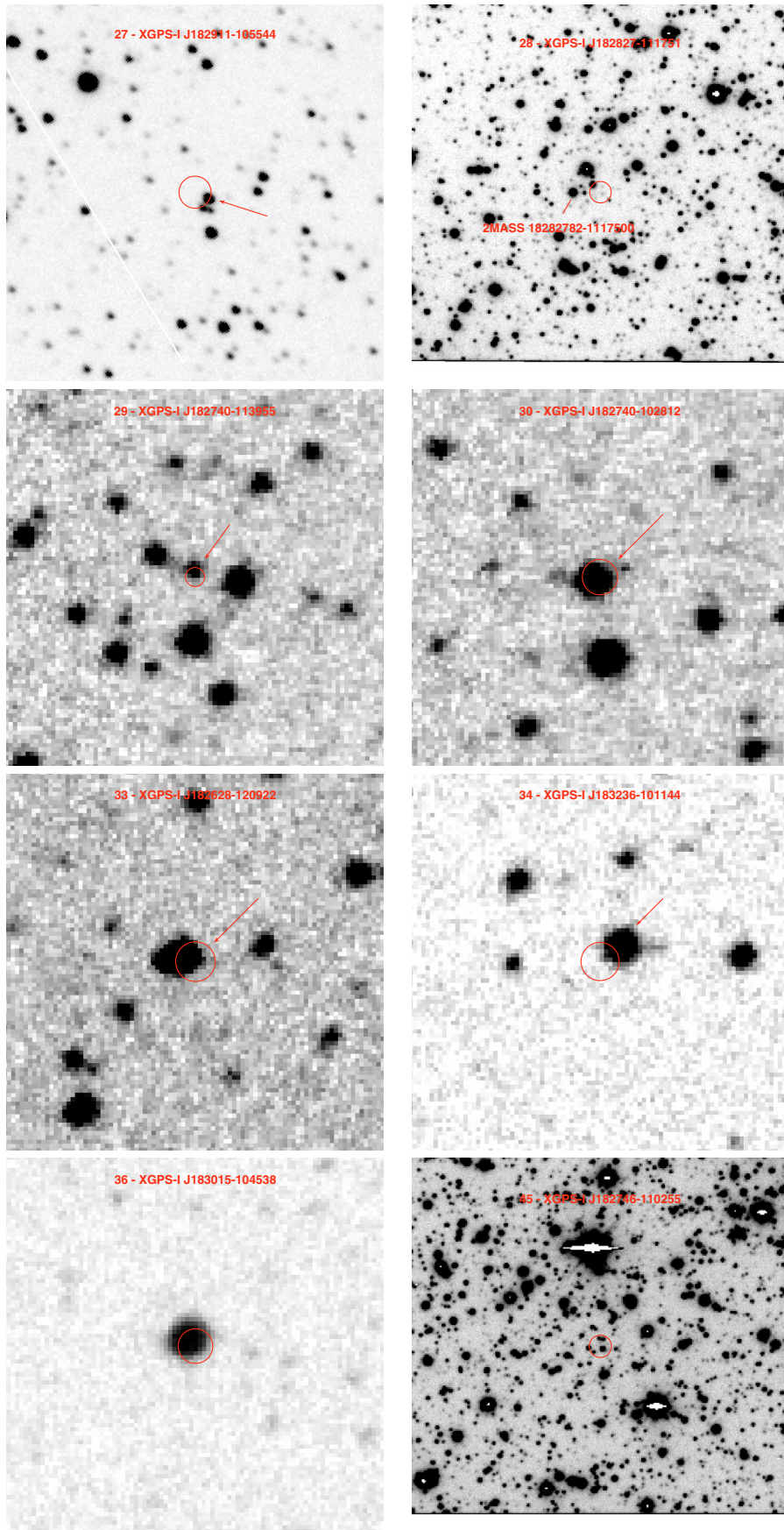


Fig. 33. continued.

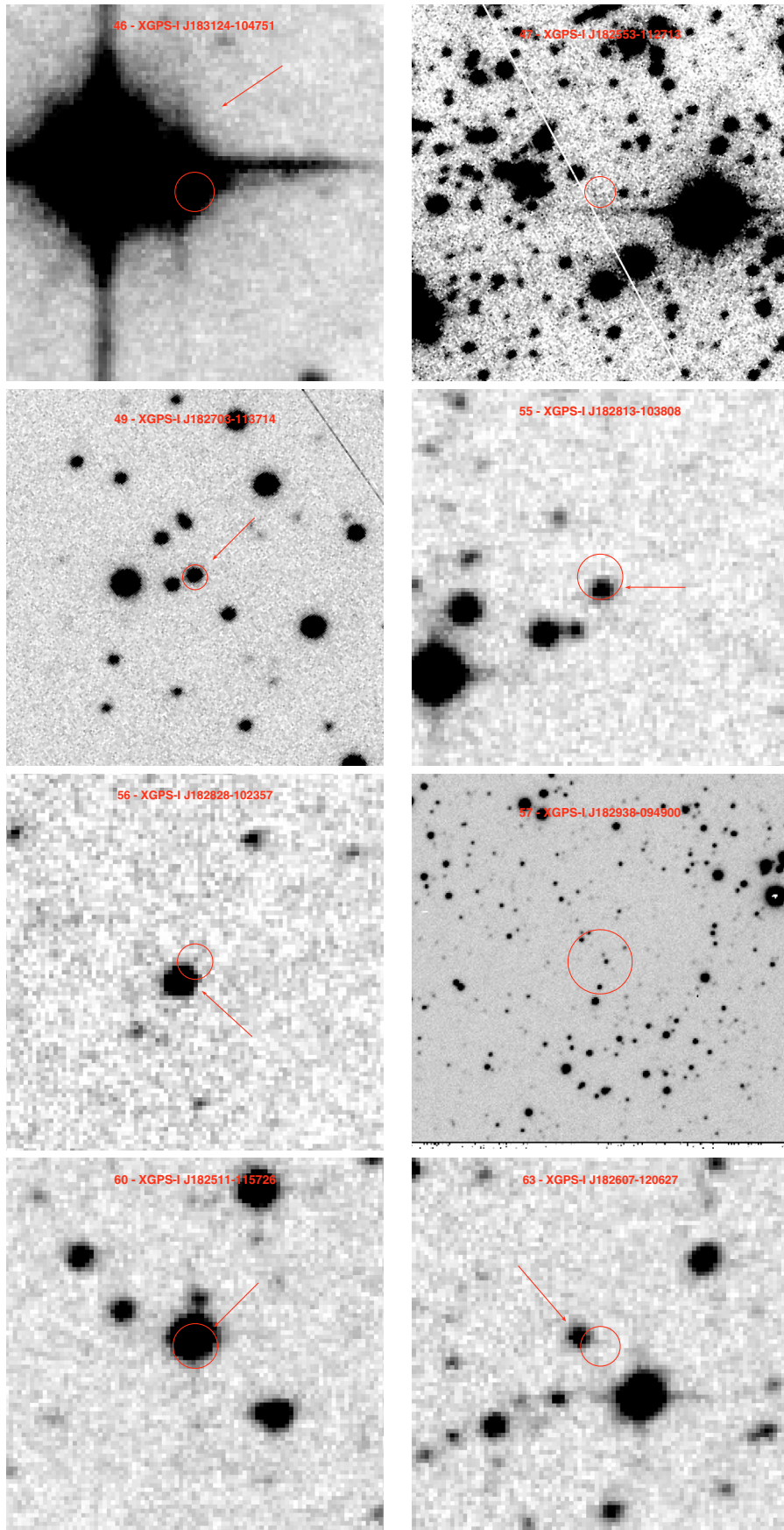


Fig. 33. continued.

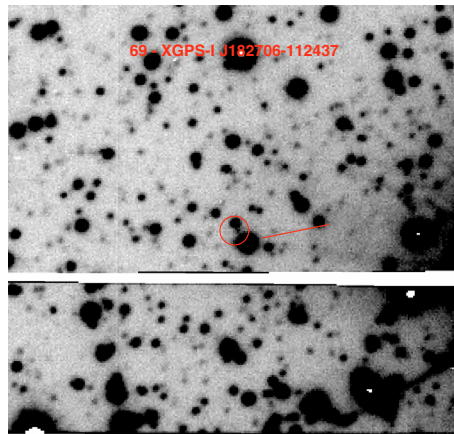


Fig. 33. continued.

Table 11. Origin of the finding charts shown in Fig. 33.

XGPS id	Telescope/Survey	Band	Exposure(s)/Plate id
2	SERC/MAMA	SR	SRC734S
3	SERC/MAMA	SR	SRC734S
6	SERC/MAMA	SR	SRC734S
7	ESO-VLT-U4/FORS2	WL	20
11	SERC/MAMA	SR	SRC734S
13	SERC/MAMA	SR	SRC734S
14	SERC/MAMA	SR	SRC734S
16	SERC/MAMA	SR	SRC734S
17	ESO-3P6/EFOSC	<i>I</i>	300
18	ESO-3P6/EFOSC	<i>I</i>	300
19	SERC/MAMA	SR	SRC734S
20	ESO-3P6/EFOSC	<i>R</i>	5
21	ESO-3P6/EFOSC	<i>I</i>	300
22	ESO-3P6/EFOSC	<i>I</i>	300
23	SERC/MAMA	SR	SRC734S
25	SERC/MAMA	SR	SRC734S
27	ESO-3P6/EFOSC	<i>R</i>	60
28	ESO-VLT-U4/FORS2	WL	20
29	SERC/MAMA	SR	SRC734S
30	SERC/MAMA	SR	SRC734S
33	SERC/MAMA	SR	SRC734S
34	SERC/MAMA	SR	SRC734S
36	SERC/MAMA	SR	SRC734S
45	ESO-VLT-U4/FORS2	WL	20
46	SERC/MAMA	SR	SRC734S
47	ESO-3P6/EFOSC	<i>R</i>	60
49	ESO-3P6/EFOSC	<i>B</i>	90
55	SERC/MAMA	SR	SRC734S
56	SERC/MAMA	SR	SRC734S
57	ESO-VLT-U4/FORS2	<i>I</i>	60
60	SERC/MAMA	SR	SRC734S
63	SERC/MAMA	SR	SRC734S
69	ESO-VLT-U4/FORS2	WL	20